NASA/CR—2017-219697

Toward Understanding Tip Leakage Flows in Small Compressor Cores Including Stator Leakage Flow

Reid A. Berdanier and Nicole L. Key
Purdue University, West Lafayette, Indiana

October 2017

NASA STI Program . . . in Profile

Since its founding, NASA has been dedicated to the advancement of aeronautics and space science. The NASA Scientific and Technical Information (STI) Program plays a key part in helping NASA maintain this important role.

The NASA STI Program operates under the auspices of the Agency Chief Information Officer. It collects, organizes, provides for archiving, and disseminates NASA's STI. The NASA STI Program provides access to the NASA Technical Report Server—Registered (NTRS Reg) and NASA Technical Report Server—Public (NTRS) thus providing one of the largest collections of aeronautical and space science STI in the world. Results are published in both non-NASA channels and by NASA in the NASA STI Report Series, which includes the following report types:

- TECHNICAL PUBLICATION. Reports of completed research or a major significant phase of research that present the results of NASA programs and include extensive data or theoretical analysis. Includes compilations of significant scientific and technical data and information deemed to be of continuing reference value. NASA counter-part of peer-reviewed formal professional papers, but has less stringent limitations on manuscript length and extent of graphic presentations.
- TECHNICAL MEMORANDUM. Scientific and technical findings that are preliminary or of specialized interest, e.g., "quick-release" reports, working papers, and bibliographies that contain minimal annotation. Does not contain extensive analysis.
- CONTRACTOR REPORT. Scientific and technical findings by NASA-sponsored contractors and grantees.
- CONFERENCE PUBLICATION. Collected papers from scientific and technical conferences, symposia, seminars, or other meetings sponsored or co-sponsored by NASA.
- SPECIAL PUBLICATION. Scientific, technical, or historical information from NASA programs, projects, and missions, often concerned with subjects having substantial public interest.
- TECHNICAL TRANSLATION. English-language translations of foreign scientific and technical material pertinent to NASA's mission.

For more information about the NASA STI program, see the following:

- Access the NASA STI program home page at http://www.sti.nasa.gov
- E-mail your question to help@sti.nasa.gov
- Fax your question to the NASA STI Information Desk at 757-864-6500
- Telephone the NASA STI Information Desk at 757-864-9658
- Write to:
  NASA STI Program
  Mail Stop 148
  NASA Langley Research Center
  Hampton, VA 23681-2199

NASA/CR—2017-219697

Toward Understanding Tip Leakage Flows in Small Compressor Cores Including Stator Leakage Flow

Reid A. Berdanier and Nicole L. Key
Purdue University, West Lafayette, Indiana

Prepared under Grant NNX11AI59A

National Aeronautics and
Space Administration

Glenn Research Center
Cleveland, Ohio 44135

October 2017

Acknowledgments

This work was supported by the National Aeronautics and Space Administration (NASA) as a renewal to award NNX11AI59A, originally under ROA-2010 NRA of the Subsonic Fixed Wing project. The technical monitor for this project was Dr. Mark Celestina. Additional support is gratefully acknowledged from Rolls-Royce, Dr. Aaron King, Dr. Steve Wellborn, and all other people who have provided helpful insights throughout this project. Collection of experimental data for this project was completed with assistance from Dr. Natalie Smith, Nicholas Kormanik III, Douglas Matthews, and Jordan Lewis. Significant thanks are also due to John Fabian, Robert McGuire, and the other support staff members at Purdue University who helped to facilitate the success of this project.

This work was sponsored by the Advanced Air Vehicle Program
at the NASA Glenn Research Center.

Level of Review: This material has been technically reviewed by expert reviewer(s).

Available from

NASA STI Program
Mail Stop 148
NASA Langley Research Center
Hampton, VA 23681-2199

National Technical Information Service
5285 Port Royal Road
Springfield, VA 22161
703-605-6000

This report is available in electronic form at http://www.sti.nasa.gov/ and http://ntrs.nasa.gov/

Toward Understanding Tip Leakage Flows in Small Compressor Cores Including Stator Leakage Flow

Reid A. Berdanier and Nicole L. Key
Purdue University
West Lafayette, Indiana 47907

SUMMARY

The focus of this work was to provide additional data to supplement the work reported in NASA/CR—2015-218868 (Berdanier and Key, 2015b). The aim of that project was to characterize the fundamental flow physics and the overall performance effects due to increased rotor tip clearance heights in axial compressors. Data have been collected in the three-stage axial research compressor at Purdue University with a specific focus on analyzing the multistage effects resulting from the tip leakage flow. Three separate rotor tip clearances were studied with nominal tip clearance gaps of 1.5%, 3.0%, and 4.0% based on a constant annulus height.

Overall compressor performance was previously investigated at four corrected speedlines (100%, 90%, 80%, and 68%) for each of the three tip clearance configurations. This study extends the previously published results to include detailed steady and time-resolved pressure data at two loading conditions, nominal loading (NL) and high loading (HL), on the 100% corrected speedline for the intermediate clearance level (3.0%). Steady detailed radial traverses of total pressure at the exit of each stator row are supported by flow visualization techniques to identify regions of flow recirculation and separation. Furthermore, detailed radial traverses of time-resolved total pressures at the exit of each rotor row have been measured with a fast-response pressure probe. These data were combined with existing three-component velocity measurements to identify a novel technique for calculating blockage in a multistage compressor.

Time-resolved static pressure measurements have been collected over the rotor tips for all rotors with each of the three tip clearance configurations for up to five loading conditions along the 100% corrected speedline using fast-response piezoresistive pressure sensors. These time-resolved static pressure measurements reveal new knowledge about the trajectory of the tip leakage flow through the rotor passage. Further, these data extend previous measurements identifying a modulation of the tip leakage flow due to upstream stator wake propagation.

Finally, a novel instrumentation technique has been implemented to measure pressures in the shrouded stator cavities. These data provide boundary conditions relating to the flow across the shrouded stator knife seal teeth. Moreover, the utilization of fast-response pressure sensors provides a new look at the time-resolved pressure field, leading to instantaneous differential pressures across the seal teeth.

Ultimately, the data collected for this project represent a unique data set which contributes to build a better understanding of the tip leakage flow field and its associated loss mechanisms. These data will facilitate future engine design goals leading to small blade heights in the rear stages of high pressure compressors and aid in the development of new blade designs which are desensitized to the performance penalties attributed to rotor tip leakage flows.

TABLE OF CONTENTS

LIST OF TABLES

LIST OF FIGURES

Figure Page

LIST OF SYMBOLS

Symbol	Description
A	Geometric Flow Area
B	Blockage
c	Chord
f	Frequency
H	Blade Span/Annulus Height
$\dot{m}$	Mass Flow Rate
Ma	Mach Number
N	Rotational Speed
P	Pressure
r	Radial Coordinate
R^2	Coefficient of Determination
Re	Reynolds Number
s	Blade Pitch
t	Time, Blade Thickness
U_{tip}	Blade Tip Speed
V	Absolute Velocity
x	Axial Coordinate

Greek

α	Absolute Flow (Yaw) Angle
δ^*	Velocity Density Deficit
$\delta_{()}$	Clearance Derivative
ϵ	Knife Seal Tooth Clearance
Ω	Blade Angular Velocity
ϕ	Pitch Angle
ρ	Density
τ	Tip Clearance Height
θ	Tangential Coordinate
ξ	Leakage Flow Trajectory Angle

Subscripts

AA	Radial and Circumferential Area Average
act	Actual Condition
c	Corrected Condition
L	Leakage
mech	Mechanical
o	Stagnation Condition
RA	Radial Area Average
ref	Reference Condition
stall	Stall Condition
x	Axial Direction

Symbol	Description
Accents	
$\langle\ \rangle$	Phase-Locked Ensemble Average (EA)
$*$	Condition of Matched TPR/$\dot{m}_c$

LIST OF ABBREVIATIONS

Abbreviation	Description
AIP	Aerodynamic Interface Plane
BPP	Blade Passing Period
CFD	Computational Fluid Dynamics
CMM	Coordinate Measuring Machine
DCA	Double Circular Arc
DMLS	Direct Metal Laser Sintering
DSA	Digital Sensor Array
EA	Ensemble Average
FT	Fourier Transform
HL	High Loading
HPC	High Pressure Compressor
HW	Hot-wire
IBR	Integrally Bladed Rotor
IGV	Inlet Guide Vane
LDV	Laser Doppler Velocimetry
LFS	Leakage Flow Size
LL	Low Loading
LSRC	Low-Speed Research Compressor
NASA	National Aeronautics and Space Administration
NB	Number of Blades
NL	Nominal Loading
NS	Near Stall
OPR	Overall Pressure Ratio
PE	Peak Efficiency
PIV	Particle Image Velocimetry
RMS	Root-Mean-Square
SFW	Subsonic Fixed Wing
SLE	Special Limits of Error
SM	Stall Margin
TC	Tip Clearance
TLF	Tip Leakage Flow
TPR	Total Pressure Ratio
TTL	Transistor-Transistor-Logic

CHAPTER 1: INTRODUCTION

Rising fuel costs and environmental concerns are continuing to drive gas turbine engine development toward increased overall efficiency and decreased fuel burn. However, achieving these goals will likely lead to smaller gas turbine engine cores for two reasons. First, improvements in materials and cooling schemes allow increased turbine inlet temperatures and, thus, increased overall pressure ratios (OPR) that will allow for higher thermal efficiencies. For a given engine size, an increased OPR is most easily accommodated through added stages. Second, larger bypass ratios lead to increased propulsive efficiencies in turbofan engines. For large aircraft, current under-wing engine mounting arrangements are limited in their ability to accommodate larger fan diameters. For small aircraft, the nacelle is already a significant contributor to overall aircraft drag and an increased fan diameter could have an overall negative effect. As these limits for the outer diameter of a turbofan are encountered, designers are turning their attention to reducing the size of the core as a means for increasing the bypass ratio. Both of these driving factors result in smaller blading, especially in the rear stages of a high-pressure compressor (HPC).

As engine cores become smaller, the flow path area decreases, and the losses in the endwall regions become more significant as they comprise a larger percentage of the total flow field. Additionally, tip clearances will not scale with the decreased blade size because of manufacturing tolerances and the margin needed for transient operation and thermal growth. As a result, a smaller core leads to rotor tip clearance heights which are large relative to the blade size. A larger relative tip clearance height leads to increased blockage due to the associated tip leakage flows, as well as potential issues with stage matching at off-design operating conditions. Previous research has suggested increased tip clearance-to-blade-height ratios causes decreased efficiency and pressure rise capability. Similarly, the ratio of clearance-to-chord may also increase, leading to a decrease in stall margin. Thus, small blade heights with increased relative clearances are expected to have a detrimental impact on HPC efficiency and operability.

However, these concerns with large tip clearance heights relative to blade size are not specific to new engine designs. Existing engine designs are also subject to these potential performance detriments as in-service deterioration results in larger clearances in compressors. The development of designs that are de-sensitized to large tip clearances would provide the ability to avoid the penalties of reduced stall margin and reduced efficiency typically associated with in-service deterioration. However, the flow physics of these tip leakage flows must be better understood in a multistage environment to generate these new designs – an understanding which must extend beyond the design point to also improve off-design compressor performance.

1.1. <u>Background</u>

1.1.1. Survey of Literature

Over the years, several dedicated literature reviews have summarized the body of work focused on tip clearance effects in compressors: Reeder (1968) and Peacock (1982, 1983). Experimental campaigns investigating several rotor tip clearances have typically been limited to isolated rotors or single stage machines operating in a low-speed regime. In particular, the results published by Hunter and Cumpsty (1982), Inoue et al. (1986), McDougall (1990), and Goto (1992) have helped to understand the overall performance effect of increased rotor tip clearance for idealized environments experiencing a clean inlet flow, free from the effects of an upstream stage. Multistage low-speed four-stage research compressors such as the facility used by Wisler (1985), and a similar facility by Tschirner et al. (2006), provide the important multistage flow environment which is expected to affect the rear stages of an HPC. However, these low-speed measurements often do not accurately represent the Reynolds numbers and Mach numbers present in the rear stages of an HPC, nor do they incorporate appreciable compressibility effects.

Using data collected from multistage compressors of varying designs, Freeman (1985) gives a thorough overview of rotor tip clearance effects in axial compressors. This information provides a valuable summary of overall performance effects for varying rotor tip clearance heights, but it does not address the underlying flow physics and stage-to-stage impact of tip leakage flows.

Of the existing studies considering several rotor tip clearance heights, few have studied the effects of rotor tip clearance heights larger than 3% blade span. Also, many published results have focused efforts toward building a detailed understanding of the fundamental leakage flow physics at a single rotor tip clearance height, instead of combining knowledge gained from several clearance heights: e.g., Lakshminarayana et al. (1982a, 1982b), Shin et al. (2008), and Sans et al. (2013).

Experimental results from cascades have also been beneficial to the growth of knowledge relating to tip clearance flows. Of note, Williams et al. (2010) recently used a cascade to investigate very large tip clearances up to 6% of annulus height, which is representative for the HPC stages of industrial gas turbines. As expected, losses increased with increasing tip clearance, however, losses leveled off for clearances larger than 4% annulus height. The authors hypothesized that for large tip clearances, the effect of the endwall became less important, and the flow through the tip gap behaved more like that of a wing tip vortex since the casing had less impact on the leakage flow.

1.1.2. Characteristics of Tip Leakage Flows

The static pressure difference across the rotor tip clearance is the primary mechanism driving the flow through the tip gap. In addition to the pressure-driven flow, the relative motion between the rotor blade and the stationary casing endwall also creates a shear-driven flow. Without a tip clearance, there exists a separation in the corner between the suction surface of the blade and the endwall as the low-velocity fluid near-wall flow is unable to negotiate the required pressure gradient as the radius of curvature decreases. The presence of a small tip clearance can be beneficial since it will energize the separation-prone fluid. Although some authors have suggested the existence of this optimal clearance height which could lead to a peak efficiency condition, this clearance is typically smaller than what can be achieved for mechanical reasons. In most applications, the tip leakage flows found in compressor rotors are responsible for entropy generation, loss in peak pressure rise, and decreased stall margin (Cumpsty, 2004).

In a canonical study, Wisler (1985) measured a change in overall compressor performance with increased tip gap in a four-stage low-speed research compressor (LSRC) at GE. When the tip clearance was increased from 1.36% to 2.8% of blade height, the overall compressor efficiency dropped by 1.5 points, and peak pressure rise was reduced by 9.7%. Wisler also showed a decrease of operability range by an 11% increase of stalling flow coefficient.

Some authors have discussed the formation of a shear layer and a vortex sheet as a result of the leakage fluid passing through the rotor tip gap interacting with the adjacent blade passage. Storer and Cumpsty (1991) used cascade measurements to show that the tip leakage vortex increased in size and strength as the clearance was increased. Once the leakage vortex separates from the blade surface, it may "burst," or break down into a high-loss region creating significant blockage to the main throughflow. The diffusive nature of the flow field contributes to this breakdown as the leakage vortex grows circumferentially and radially during its travel through the rotor passage. While passing through the tip gap, however, the clearance flow experiences little loss. Instead, the primary loss mechanism is due to the diffusive mixing that occurs when the jet-like clearance flow issues into the main passage flow.

Using measurements acquired on the same LSRC used by Wisler (1985), Yoon et al. (2006) showed that the tip leakage vortex strengthens and moves upstream as flow coefficient is reduced and also as tip clearance is increased. New findings from this experiment include that the tip vortex was weakened and moved downstream as stagger was increased. At very large clearances (5.5% chord), the vortex exhibited a change in trajectory because of a sudden increase in flow between mid-chord and trailing edge. This pushed the tip vortex toward the neighboring blade.

This circumferential flow trajectory increases the potential existence of a double leakage flow condition, as introduced by Khalsa (1996). Double leakage refers to the case when the tip leakage flow convects across the blade passage at a high trajectory angle and passes through tip clearance of the adjacent blade. In this case, the low-pressure fluid contained in the tip clearance flow faces a potentially compounding loss as it passes through the second clearance gap. The presence or absence of this effect is dependent upon the loading of the blade row through its effect on the trajectory of the vortex and the solidity of the blade row (Dickens and Day, 2011).

The role of the upstream stator is important for the development of the tip leakage flow. In particular, Mailach et al. (2008) used Laser Doppler Anemometry to investigate the tip region of a four-stage low-speed research compressor. The upstream stator wakes had a profound influence on the trajectory of the tip leakage vortex, the intensity of the tip leakage vortex, and the position of maximum tip leakage flow along the chord. This same interaction has also been addressed recently by other authors (Smith et al., 2016; Krug et al., 2015).

Sirakov and Tan (2003) used time-accurate Reynolds-averaged Navier-Stokes simulations to understand the role of unsteadiness on rotor tip leakage flows by replacing the effect of an upstream stator with representative wake deficits. Two situations were investigated for their study: a steady wake deficit and a pulsing wake deficit – the second representing what would be experienced by a rotating blade row. The authors observed a beneficial unsteady interaction between the rotor and (simulated) stator, which was attributed to the suppression of the double leakage phenomenon.

1.1.3. Computational Validation Using High-Speed Experimental Data

Detailed experimental datasets are critical for validating computational models of tip leakage flow effects on compressor performance. Suder and Celestina (1996) compared computations to experimental data obtained in the single stage transonic compressor (Stage 37) facility at NASA Glenn Research Center. Two loading conditions (peak efficiency and near stall) were investigated at two operating speeds: 60% speed with subsonic flow and 100% speed where the shock structure could be studied. The tip clearance at design speed was 0.5% span (0.7% chord). Laser anemometer measurements captured the interactions between the tip leakage vortex and the shock structure at high speeds. These authors showed that the radial influence of the tip leakage flows extended over a range up to twenty times the physical clearance at operating speeds for which shocks were present. At the subsonic conditions, however, the radial influence of the leakage flow was reduced to only five times the physical clearance.

These experimental data for Stage 37 allowed Van Zante et al. (1999) to investigate computational models of the tip clearance flow field focusing on the impact of grid topology, the numerical treatment of the tip gap, and their effects on the solution. The authors found that gridding the tip gap did not provide any advantages over using a simple tip clearance model, but the wall-bounded shear layer was an important component to the tip clearance flow, especially when the difference between the relative velocities of the leakage jet and casing was large. Gupta et al. (2003) agreed that sufficient clustering of grid points near the casing, as a method for capturing the shear layer, was critical to a successfully modeling the tip leakage flows. However, these authors were able to achieve the best results by using a square tip and fully resolving the tip gap rather than using approximate methods. A summary of these and other difficulties affecting computational models for turbomachinery applications, including tip clearance gap modeling challenges, is addressed by Denton (2010).

The observations by Van Zante et al. (1999) and Gupta et al. (2003) provide an excellent example of how a quality experimental dataset can be used to calibrate CFD models. However, the isolated rotor and single stage environment does not capture all of the important flow physics present in a multistage compressor. In particular, spanwise mixing and endwall boundary layers are influenced by upstream stages. These, in addition to the tip leakage flow, are major contributors to blockage in the endwall region and can lead to stage matching issues (Cumpsty, 2004).

1.1.4. Spanwise Mixing

Spanwise mixing is responsible for distributing the high losses associated with the endwall flows toward mid-span. For geometry with low aspect ratios, this spanwise mixing component must be accurately modeled to capture the flow field correctly. Adkins and Smith (1982) developed a spanwise mixing model which suggested secondary flow generated spanwise and cross-passage velocities to enhanced mixing, and it agreed well with several test cases. However, because this model was based on inviscid secondary flows, it was not adequate for cases with significant regions of separated flow, including high loading or other off-design cases.

A different mechanism responsible for spanwise mixing was proposed by Gallimore and Cumpsty (1986). Using an ethylene tracer gas technique, these authors concluded that turbulent diffusion, rather than the radial velocity associated with secondary flows, was the main mechanism for spanwise mixing. For this analysis, the experiments were performed near a peak-efficiency point, but off-design conditions with highly separated flows were not investigated.

In fact, both of the mechanisms identified by Adkins and Smith (1982) and Gallimore and Cumpsty (1986) can be important. Wisler et al. (1987) used the ethylene tracer gas technique and hot-wire anemometry to investigate mixing at design loading and high loading operating conditions. In the “free stream region,” they found the primary mechanism for mixing was turbulent diffusion. In the endwall regions and along the blade surfaces, though, secondary flow effects were equally responsible, if not slightly more important than turbulent diffusion. A follow-on computational study by Leylek and Wisler (1991) confirmed the importance of both turbulent diffusion and secondary flows in the spanwise mixing process. However, these authors noted important considerations to accurately recreate spanwise mixing representative of real engine operating environments. Of note, the turbulence intensity associated with upstream blade and vane wakes must be appropriately introduced, and the blade row inlet endwall boundary layer must be adequately represented to achieve the secondary flow field.

The single stage low-speed study conducted by Goto (1992) at the Whittle Laboratory investigated the effect of different rotor tip clearances (up to 3% chord) on the flow field in the downstream stator, with an emphasis on spanwise mixing. As the tip clearance increased, the blockage in the tip region increased and led to a decrease in wake size near the stator hub and a suppression of the unsteadiness in the hub region.

1.1.5. Blockage and Stage Matching

In compressors, blockage represents the reduction of flow area due to the existence of low momentum fluid. Blockage will increase the velocity in the core flow region, thereby reducing the work done by the rotor on the core flow. As endwall boundary layers grow at off-design operating conditions, stage matching problems may be introduced. However, a lack of understanding for this endwall boundary layer growth in multistage axial compressors also exists at design conditions and typically forces designers to rely on correlations, as explained by Cumpsty (2004).

The most significant body of data on compressor endwall boundary layers was acquired by Smith (1970) in the four-stage LSRC at GE. These data showed that blockage was essentially unchanged across a repeating stage, and blockage was a function of tip clearance and loading condition. However, the repeating-stage model is valid for multistage compressors with large aspect ratios and relatively small clearances. The repeating stage condition was not achieved for an aspect ratio of 1.96, the lowest aspect ratio tested by Smith. The rear stages of high pressure core compressors typically have aspect ratios on the order of unity. Thus, further information must be collected under these conditions to supplement the data published by Smith.

Cumpsty (1986) presented measurements from a four-stage compressor at lower Reynolds numbers. The data indicated that the rotor tip clearance (or stator hub clearance) was a critical parameter for determining the endwall boundary layer thickness. Using a model developed to relate the flow through the tip clearance to the downstream blockage, Khalid et al. (1999) proposed that the total pressure loss in the endwall region resulted from the interaction of tip leakage flows and passage flows, and the vortical structure associated with the leakage vortex was deemed less important. Khalid et al. also correlated endwall blockage with aerodynamic loading on the blade. Data acquired by Suder (1998) on the isolated transonic rotor (Rotor 37) showed that the blockage in the endwall region increased with blade loading in agreement with Khalid's correlation. Further, 3D Particle Image Velocimetry (PIV) measurements collected by Wernet et al. (2005) in a large-scale four-stage low-speed compressor at NASA Glenn Research Center showed that the radial velocity component was important in determining the radial extent of influence of the tip leakage flows and the blockage associated with these flows.

1.1.6. Stator Hub Seal Leakage Flow

The influence of seal leakage flows for shrouded stators in multistage compressor has been evaluated by several researchers in the past. Mahler (1972) conducted a thorough assessment of many dynamic sealing technologies in gas turbine engines. From that study, Mahler notably reported a series of correlations describing the relationship between discharge coefficient and flow parameters (e.g., Reynolds number, tooth clearance, tooth geometry) for knife seal teeth.

Beyond this, Mahler (1972) and Freeman (1985) specifically outlined efficiency penalties incurred as a result of increased knife seal clearance gaps.

Wellborn (1996) presented results from experimental data collected in a four-stage low-speed axial compressor, and those data were the foundation for a parametric study geared toward improving design theory for sealing technologies. Wellborn's measurements interrogated the relationship between the shrouded stator seals and the primary throughflow, and the data collected served as detailed boundary conditions from which to build high-quality computational models comparing with the experimental results. Details of these boundary condition data, as well as a preliminary comparison with computational results, are given by Wellborn and Okiishi (1999).

From the computational modeling approach, LeJambre et al. (1998) identified the value of incorporating seal cavity geometries. Heidegger et al. (1996) further showed how the presence of seal cavity geometries can significantly influence the simulated performance of the primary throughflow for the stator row, as flow is removed and reintroduced. These authors showed that the importance of including these effects increases as the compressor speed increases. As a follow-on to the experimental data campaigns led by Wellborn (1996), Wellborn et al. (2000) presented the results of a one-dimensional seal cavity model which was implemented with the average-passage solver, APNASA, to create a powerful analysis and design tool for seal cavity flows.

More recently, Yoon et al. (2015) studied the influence of seal tooth count while assessing stator hub configuration. Computational modelers continue to seek the ability to accurately model shrouded stator seal cavity flows, and the debate of cantilevered versus shrouded stators in the context of leakage flows and loss mechanisms is a closely-coupled part of this modeling desire.

1.2. Program Objectives

NASA led a Turbomachinery Technical Working Group that provided a list of propulsion improvements necessary to meet the Subsonic Fixed Wing (SFW) project goals, specifically allowing the project to meet its N+1 and N+2 reduced fuel burn goals. One of the main topics on the list was tip leakage flows in high pressure ratio cores. The group anticipates that the smaller cores will result in blade tip clearances of 2% to 4% of blade height, and the resulting compressor efficiency loss due to the leakage flow through the tip gap could be as high as 5 points, corresponding to a specific fuel consumption (SFC) effect on the order of 3% (Heidmann, 2009). Thus, reductions in these endwall and tip leakage losses are absolutely necessary to realize SFC improvements.

The research presented in this report supports NASA's strategic goals of reduced fuel burn in the SFW area by contributing to the understanding of core compressor losses associated with tip leakage flows and other endwall losses. Once the flow physics associated with these losses are understood, CFD models can be generated to accurately predict off-design performance. These data will be instrumental in calibrating predictive tools for multistage compressor performance. Before designs attempting to mitigate or desensitize compressor performance to large tip clearances can be successfully achieved, the flow physics associated with these large tip clearance flows must be well understood and accurately predicted. The data acquired in this project help to illuminate such flow physics.

The objective of this research project was to provide detailed flow field measurements in a three-stage axial compressor typical of the rear stages in an HPC. The availability of these data provides an opportunity to calibrate existing CFD tools for off-design prediction and stage matching. The experimental campaign has measured the flow field for three different rotor tip clearances: a baseline case with a 1.5% tip clearance (with respect to annulus height), a 3.0% tip clearance, and a large tip clearance of 4.0%. A comparison of three different tip clearance configurations allows the performance deltas between configurations to be captured. Overall compressor performance maps have been acquired, as well as detailed flow field measurements. A combination of traditional measurement techniques such as steady and time-resolved total pressures, as well as over-rotor static pressures, interrogate flow structures in the embedded stage of a multistage compressor. Furthermore, a unique instrumentation design facilitates measurements of time-resolved pressures in the shrouded stator cavity, leading to differential pressure data across the knife seal teeth. This project represents the continuation of one of the few complete databases available in the open literature, and the only database focused on multistage flow in the rear stages of an HPC with large relative tip clearances.

CHAPTER 2: EXPERIMENTAL METHODS

2.1. Research Facility

2.1.1. Integral Facility Components

The Purdue University three-stage axial compressor research facility is a geometrically-scaled design which models the rear stages of a high-pressure core compressor. In particular, the facility features engine-representative Reynolds numbers and Mach numbers, which makes it a useful vehicle for research at a high technology readiness level. Furthermore, the intermediate rotational speed regime and the multistage design of the facility create unique opportunities to analyze an “embedded” stage and complex multistage flow effects.

The Purdue three-stage compressor facility features a 6061 aluminum casing and all blading is machined from 17-4 stainless steel. The compressor comprises an inlet guide vane (IGV) followed by three stages. The inlet guide vane and the three rotor rows are double-circular arc (DCA) designs, and the three stator vane rows are NACA 65-series airfoils. All three of the rotor rows are integrated bladed rotor (IBR) “blisk” designs, such that each of the three rotor rows represents one solid piece of material. Further, each of the stationary vane rows has been created as a 180-degree monolithic segment, with vanes which are fully-shrouded at the inner and outer diameters. Specific geometric parameters for the blading in the facility are outlined in Table 2.1.

Each of the stationary vane rows is individually circumferentially indexable for up to two full stator vane passages, allowing circumferential flow variations to be measured with stationary instrumentation. Each of the vane rows is moved with a pair of linear actuators during compressor operation, and precision string potentiometers provide feedback control of the vane positions. This two-vane circumferential measurement capability was an expansion beyond previous capabilities which was made possible through the compressor casing hardware required for this project.

Table 2.1: Purdue three-stage compressor airfoil design parameters.

Blade Row	Camber [°]		Stagger [°]		Chord [in.]		t/c	Airfoils		Ma (avg)		Re_c
	Hub	Tip	Hub	Tip	Hub	Tip		NB	Type	Rel	Abs	10^5
IGV	-12.3	-14.0	8.2	9.0	2.00	2.00	0.065	44	DCA	0.26	0.26	3.0
R1	44.7	25.8	32.6	47.8	2.46	2.81	0.045	36	DCA	0.46	0.32	7.0
S1	49.5	48.3	25.6	24.0	2.11	2.11	0.065	44	65	0.35	0.35	4.4
R2	42.4	24.6	35.4	49.8	2.60	2.96	0.049	33	DCA	0.45	0.31	7.7
S2	49.7	48.4	26.1	24.6	2.22	2.22	0.065	44	65	0.33	0.33	4.6
R3	39.5	22.9	38.2	51.8	2.75	3.13	0.051	30	DCA	0.44	0.31	8.4
S3	62.4	61.2	19.7	18.1	2.35	2.35	0.065	50	65	0.31	0.31	4.8

The research compressor is driven from the rear by a 1400 hp AC motor through a 5:1 speed-increasing gearbox to provide a nominal rotational speed of 5000 rpm at the design point. A liquid-cooled variable frequency drive system paired with an encoder on the motor drive shaft provides the capability to maintain a compressor operating speed within 0.01% of the desired mechanical speed. This capability creates an especially unique opportunity to ensure confidence in the repeatability of measurements as they relate to the rotational speed of the machine. In addition to the motor encoder, an optical laser tachometer aimed at the high-speed output shaft of the gearbox creates a transistor-transistor logic (TTL) signal which is used as a once-per-revolution (1/rev) trigger for the high frequency response data acquisition systems.

The compressor operates with ambient, unconditioned air as the working fluid. As shown in Figure 2.1, the air is first drawn into a large settling chamber before passing through a reducing bellmouth into a two foot diameter duct. A long-form Venturi flow meter designed in accordance with ASME PTC-19.5 (2004) flow measurement standards accurately measures the mass flow rate passing through the compressor.

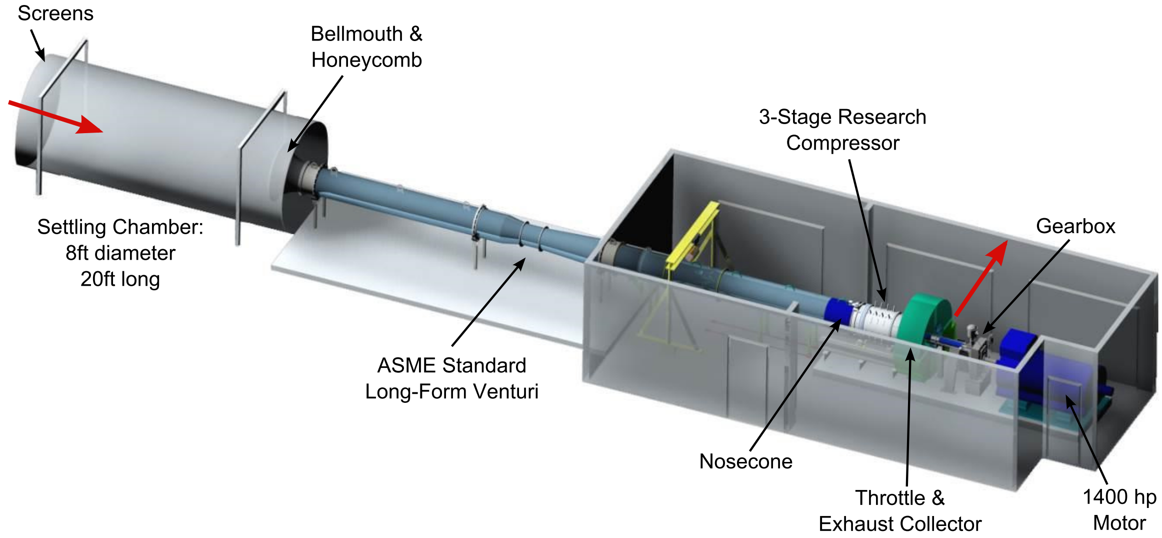

Figure 2.1: Purdue three-stage axial compressor research facility.

Two Rosemount 3051C high-accuracy pressure transmitters are installed for measuring the differential pressure across the Venturi. Because the relative uncertainty of the differential pressure measurement is dependent upon the calibration range, the two 3051C transmitters were calibrated in different pressure ranges (0 to 5 inH_2O and 0 to 8 inH_2O) and are connected via a manifold. These ranges were selected to ensure adequate coverage of the entire range of operating conditions (0 to 8 inH_2O), while maintaining a measurement near the peak efficiency point which utilizes the smallest possible measurement uncertainty. Moreover, in the low flow rate measurement range, the pair of devices provides a redundant measurement for added confidence. As a complement to the differential pressure measurements, a pitot-static pressure probe with an integrated T-type thermocouple is installed just upstream of the Venturi meter, and the measurements from this probe are used to define the density and other thermodynamic properties required for the mass flow rate calculation equations.

After passing through the Venturi meter, the air continues through an insulated duct section that is 11 duct diameters in length. A bullet-nose cone upstream of the compressor directs the airflow to the constant annulus flowpath, which is defined by a two-inch passage height with a hub-to-tip ratio of 5:6. At the exit of the compressor, a sliding-annulus throttle controls the back pressure of the machine, and a scroll collector directs the air to an exhaust plane at ambient pressure. Additional specifics defining the existing facility layout can be found in Ball (2013), and a thorough discussion of facility health monitoring systems is provided by Talalayev (2011).

2.1.2. Additional Geometry Considerations

In addition to the typical geometry parameters prescribed for the Purdue three-stage compressor flowpath, other pertinent information may be required to accurately build a computational model of the machine. Of note, the labyrinth (knife) seal clearances under the stator platforms have been measured as “cold” (static) values: 0.022 in. for the IGV, 0.035 in. for Stator 1, 0.037 in. for Stator 2, and 0.024 in. for Stator 3. Operating “hot” clearances for these seals have not been measured. Further, all of the stator vanes have fillet radii at both inner and outer diameter endwalls of 3/32 in., and the rotor hub fillet radii are all 0.150 in. The leading edges of the rotor blades have elliptical shape, and the stators have circular leading edges. An average surface roughness of 30-40 μin. has been prescribed for all of the internal flowpath surfaces, including the blades. A past analysis using an optical scan compared the design intent geometry of the rotor blisks with the as-manufactured geometry and confirmed that all measured dimensions are within the specified design tolerances of the parts. The rotor tip clearances for each defined operating condition have been measured, and the data are presented in a past report (Berdanier and Key, 2015b).

2.1.3. Variable Tip Clearance Hardware

A series of compressor casing hardware components were required to support the tip clearance analyses desired for this project. Three tip clearance configurations were used for this study, as outlined by the information in Table 2.2. In each configuration, one discrete tip clearance height exists for all three rotor rows (i.e., no combinations of tip clearance heights were considered). The first tip clearance configuration (TC1) represents the baseline compressor configuration that has been presented by previous investigators with this facility. This baseline configuration represents a nominal 1.5% tip clearance height as a fraction of overall annulus height.

Table 2.2: Tip clearance configurations and design intent clearance heights

Configuration	Nominal Clearance Height, τ [in]	Normalized Clearance Height, τ/H [%]	Tip Clearance Representation
TC1	0.030	1.5	Smooth Wall
TC2	0.060	3.0	Casing Recess
TC3	0.080	4.0	Casing Recess

As shown in the cartoon of Figure 2.2, the two larger tip clearance configurations (TC2 and TC3) were achieved through the use of a casing recess over the rotors. These compressor configurations nominally represent 3.0% and 4.0% tip clearance height. Although the differences between casing recesses and traditional cropped rotors have been documented in the past (Wisler and Beacher, 1989), the parametric analysis discussed by Brossman (2012) showed through computational simulation of the Purdue three-stage axial compressor that the overall performance and the individual stage performances of a compressor with these types of casing recesses – which are introduced as far as possible upstream and downstream of the rotor – sufficiently represent the trends of the same machine with a smooth wall and a cropped rotor. This, combined with the budget constraints involved with a cropped rotor study, led to the choice of using recessed casings to achieve the two larger clearance configurations.

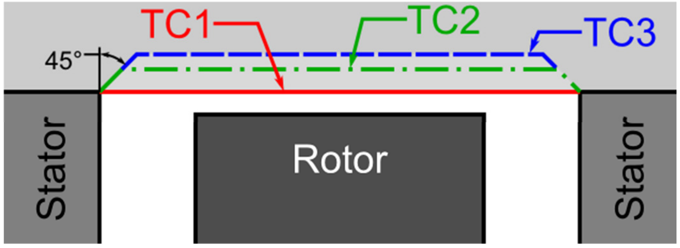

Figure 2.2: Compressor tip clearance casing geometry configurations. Sketch not to scale.

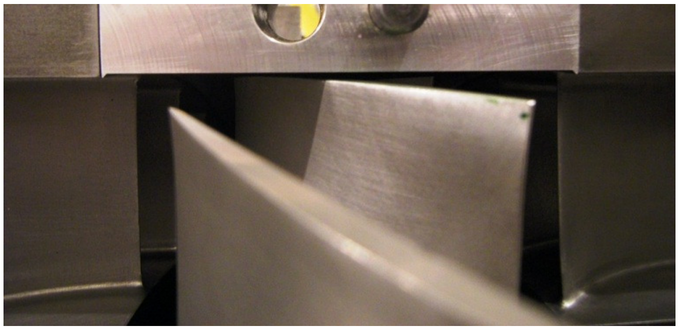

Figure 2.3: Casing recess example photograph (TC2) highlighting 45 degree angles at both ends of recess. Flow is from left to right.

Because the emphasis of this study was not on the effects of trenched casings as discussed by Wisler and Beecher (1989), the axial extent of the trenches was increased as much as allowable to the adjacent stator vanes (approximately 0.4 axial chords upstream and downstream of the rotor blades). Furthermore, 45 degree angles were introduced to ease the transition from the 2-inch annulus height of the baseline compressor defined by the stator vanes and the increased space over the rotors. The introduction of these angle features facilitates grid topology continuity for computational comparison studies. In addition to the cartoon of the casing configurations in Figure 2.2, a photographic example of the casing recess for TC2 is shown in Figure 2.3. It is important to note here that a manufacturing error led to the removal of the 45 degree ramp from the recess at the upstream side for Rotor 2, as shown in Figure 2.4, for both TC2 and TC3.

Figure 2.4: Missing 45 degree ramp upstream of Rotor 2, shown here for TC2. Flow is from left to right.

To ensure that the three separate compressor casings would provide the best possible vehicle for tip clearance performance comparisons, the casing designs incorporated tight manufacturing tolerances. In addition to preventing the introduction of tip clearance non-uniformities for a given casing configuration, these tolerances also helped to ensure consistency between the three casings. The most important of these tolerances pertained to the inner diameter of the casing over the rotor tips, for which the diameter dimension was specified with a tolerance of +0.001/0.000 in., as well as geometric tolerances of 0.005 in. for the overall runout and 0.002 in. for the profile shape. These tolerances, as well as all of the other pertinent dimensions, were verified by coordinate measuring machine (CMM) inspection processes.

2.2. Steady Compressor Performance

2.2.1. Corrected Operating Conditions for Humidity Effects

The definition of a compressor operating point is typically "corrected" to standard day conditions to ensure consistent measurements with changing inlet conditions and comparability with computational simulations. To this end, many facilities operate according to classical corrected speed and corrected mass flow rate definitions defined by turbomachinery textbooks. However, careful examination of these equations shows that they do not appropriate account for the presence of humidity in the air.

Existing compressor test codes and full engine analyses discuss the importance of humidity, and some suggest the use of conditioned or refrigerated air to avoid the potentially negative effects (NACA TN-1138, 1950; Erwin, 1964). Because the Purdue three-stage compressor facility does not have the luxury of a conditioned air supply, a method of appropriately accounting for the presence of humidity is required.

Analysis of the derivation process leading to the classical equations defining corrected speed and corrected mass flow rate for a compressor highlights the assumptions of a thermally- and calorically-perfect gas which are not necessarily appropriate for a humid air mixture. Ultimately, an alternate presentation of these same equations has been derived to circumvent the need for perfect gas assumptions. These alternate equations utilize stagnation speed of sound and stagnation density in place of stagnation temperature and stagnation pressure in the classical equations. By this process, the corrected rotational speed is determined by

$$N_c = \frac{N_{\text{mech}}}{a_{o,\text{act}}/a_{o,\text{ref}}}\ , \tag{2.1}$$

and the corrected mass flow rate is determined by

$$\dot{m}_c = \dot{m}_{\text{act}} \left(\frac{\rho_{a,\text{ref}}\ a_{o,\text{ref}}}{\rho_{a,\text{act}}\ a_{o,\text{act}}} \right). \tag{2.2}$$

A formal derivation of these conditions for humid air considerations is available in Berdanier et al. (2015).

2.2.2. Holistic Performance Measurements

For the Purdue three-stage compressor, the conditions used to calculate the corrected speed and corrected mass flow rate are measured at the Aerodynamic Interface Plane (AIP), denoted by axial position zero in the flowpath shown in Figure 2.5. At this upstream inlet plane of the compressor, the 50% span measurements from a seven-element total pressure rake and a seven-element total temperature rake are used to represent the bulk one-dimensional flow. The amount of moisture in the air is determined by an Omega HX94 thermo-hygrometer located near the inlet of the compressor, capable of measuring relative humidity with an uncertainty of ±2%. These measured parameters are used as inputs with the REFPROP thermodynamic equation program (Lemmon et al., 2013) to calculate the pertinent stagnation speed of sound and stagnation density required for Equations (2.1) and (2.2) above.

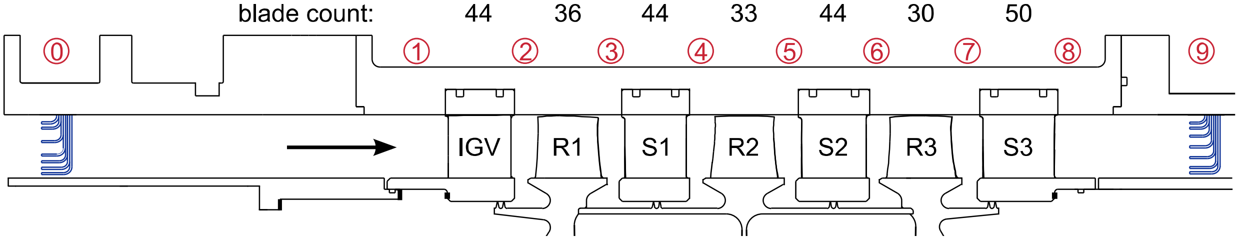

Figure 2.5: Purdue three-stage compressor facility flowpath cross section.

In addition to the seven-element total pressure and total temperature rakes installed at the AIP, 13 circumferentially-distributed static pressure taps evaluate the static pressure for this upstream inlet plane at the outer diameter of the flowpath. Great care has been incorporated to ensure circumferential uniformity of the pressures and temperatures at the inlet of the compressor, as measured by Ball (2013).

Referring again to the flowpath in Figure 2.5, the exit plane of the compressor (axial position 9) is also defined by a set of seven-element total pressure and total temperature rakes and one static pressure measurement. Separate from these upstream and downstream locations, additional seven-element total pressure and total temperature rakes are available at each of the axial positions labeled 1 through 8. Static pressures at these axial positions are evaluated by four circumferentially-distributed static pressure taps on the casing. The combination of these measurements at positions 1 through 9 provide the opportunity to define overall compressor performance and relative performance of each individual blade row or each stage. The radial position of the measurement locations for the seven-element pressure and temperature rakes at axial positions 0 and 9 are provided in Table 2.3. Additional information about the rakes positioned at interstage locations (1 through 8) is available in Berdanier and Key (2015b). The axial location of the stations labeled in Figure 2.5 is halfway between the blade rows based on the mid-span geometry, and the centerline of the rake coincides with the location of the axial measurement plane.

Table 2.3: Radial distributions of inlet and exit rake measurement locations.

Ax. Pos.	Total Pressure [% annulus height]							Total Temperature [% annulus height]						
0	12	20	30	40	60	80	88	12	20	35	50	70	80	88
9	12	20	35	50	65	80	88	12	20	30	50	70	80	88

Because the recessed casing geometry design (Figure 2.2) extends to the farthest axial extent, when the rakes are inserted with the TC2 or TC3 casing hardware, they are positioned within the tip clearance recess area. For the interstage performance measurements presented by Berdanier and Key (2015b, 2016a), the rakes were radially positioned such that the measurement positions defined in Table 2.3 are consistent with the annulus height of the stator vanes (which are geometrically unaffected by the casing recesses). These rake positions are shown graphically in Figure 2.6, such that the outer edge of the rake was aligned with the 100% annulus height location, regardless of the tip clearance configuration (i.e., whether or not a casing recess was present). By this method, the detailed measurements collected at these same axial positions extend to 101.5% or 102.5% annulus height for the TC2 and TC3 tip clearance configurations, respectively.

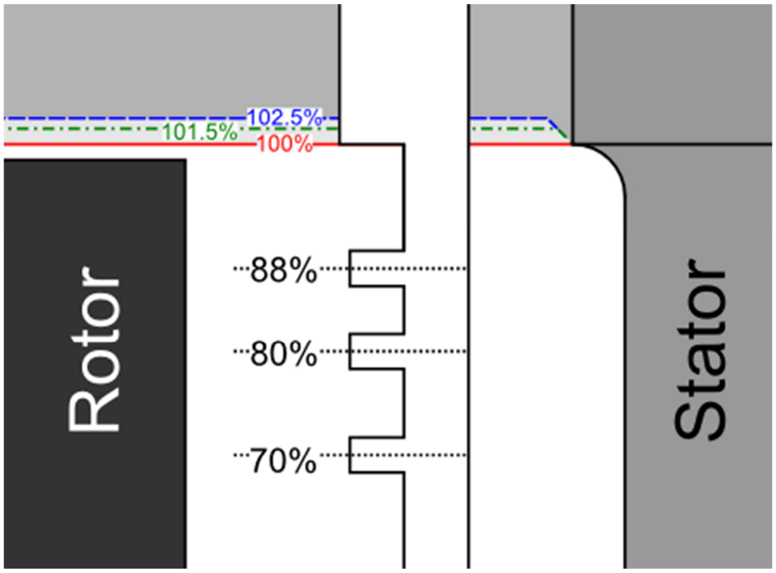

Figure 2.6: Rake positions for different tip clearance configurations.

The variable tip clearance hardware for this project expanded the capabilities of the facility to accommodate measurement rake insertion at three to six circumferential positions (the exit of the embedded second stage accommodates six positions, although three or four is standard for other axial locations) for each of the positions 1 through 8 in Figure 2.5. These same rake insertion positions also function as locations for the installation of L.C. Smith precision probe positioners for detailed measurement traverses with a variety of instrumentation technologies.

The total and static pressures for the facility are measured using Scanivalve 3217 and 3016 Digital Sensor Array (DSA) pressure scanner modules, each containing 16 temperature-compensated piezoresistive pressure sensors. Depending on the requirements of the specific measurement, the DSA channels are rated for differential pressure ranges of 1 psid, 2.5 psid, 5 psid, or 15 psid. These devices have been selected for their long-term stability ratings of 0.12% FS, 0.12% FS, 0.05% FS, and 0.05%FS, respectively. Thermal measurement drifts from these devices are prevented through regular procedures for an on-line zero calibration prior to and during compressor operation. The differential pressures are referred to an atmospheric reference pressure which is separately measured using a high-accuracy Setra 270 barometric pressure sensor with an accuracy of 0.03% FS.

The temperatures for the facility are evaluated using T-type thermocouples paired with special limits of error (SLE) extension wire. A Keysight Technologies 34980A integrating voltmeter paired with 34921A/T modules and terminal blocks accommodates the measurement of these thermocouple channels. To achieve significantly reduced uncertainty contributions to the temperature measurements, Keysight Y1138A extension cables separate the terminal blocks from the measurement modules, and a 10 kΩ thermistor with an interchangeability of ±0.18 ºR provides the reference temperature for the isothermal terminal block.

Through the use of a liquid calibration bath, the measurement chain for each of the temperature rake measurement channels was evaluated. By incorporating a high-accuracy thermistor as a reference measurement in the same calibration bath, the overall uncertainty of each individual channel was determined. These calibration results show an overall uncertainty typically less than 0.45 ºR for all temperature channels. However, the repeatability of the temperature measurements is an order of magnitude less than this value.

2.3. Tip Clearance Measurements

To complement the tip clearance data evaluated herein, the static "cold" tip clearances were measured for each of the three tip clearance configurations. These measurements were collected by measuring the blade-to-blade variability (i.e., the run-out of the rotor blade tips) using a fixed dial indicator with a rolling tip. The manufacturing tolerances of the rotor blisk show the blade-to-blade variability at any fixed location about the circumference of the compressor, as presented in Figure 2.7. These blade-to-blade measurements were collected several times to calculate the mean values in Figure 2.7. As a result, the uncertainty of the mean value is on the order of 1×10^{-4} in.

The concentricity of the rotor with respect to the casing has also been evaluated using static tip clearance measurements collected at several positions around the circumference of the compressor casing. These measurements have shown for each tip clearance configurations that the concentricity of the rotor with respect to the casing is on the order of 0.002-0.004 in. The smallest tip clearances are measured at a position of 345 degrees from the top of the compressor, in the direction of rotor rotation, as shown in Figure 2.8. The rotor concentricity can be controlled using a set of alignment bolts at both the front and rear bearing assemblies, as prescribed by Talalayev (2011). Based on the adjustment limitations outlined by Talalayev, the measured concentricity of the rotor is confirmed to be within the adjustment capabilities of the system.

As part of this study, the operating tip clearances were also measured using an FM capacitance probe system. Three probes were installed over each rotor row, equally-spaced circumferentially 120 degrees apart, at positions of 105 degrees, 225 degrees, and 345 degrees – all measured from the top of the compressor in the direction of rotor rotation (see Figure 2.8). Details of the capacitance probe system, measurement uncertainty, and operating clearance measurements are presented by Berdanier and Key (2015a, 2015b).

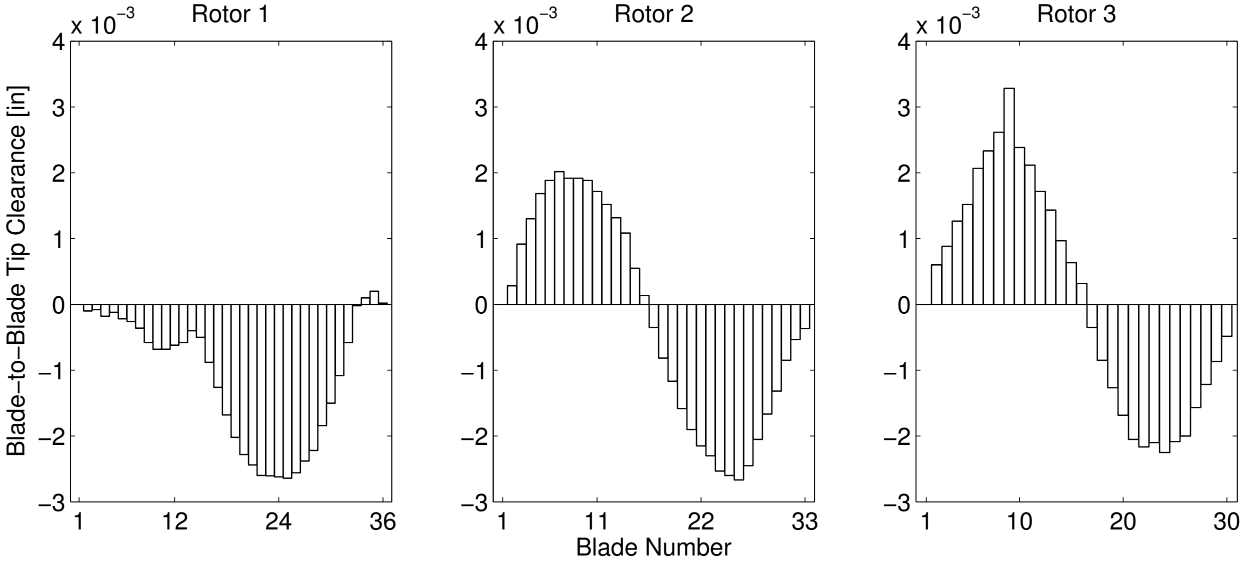

Figure 2.7: Blade-to-blade variability of tip clearance height with respect to Blade 1 for all three rotor rows.

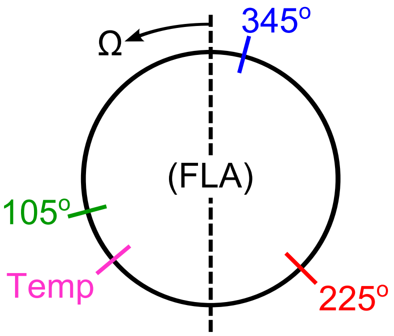

Figure 2.8: Circumferential capacitance probe measurement locations.

2.4. Detailed Radial Pressure Traverses

2.4.1. Steady Total Pressure at Stator Exit

Although typical compressor performance is adequately defined by seven-element rakes placed in interstage measurement locations, these rakes inherently lack spatial resolution, with a particular lack of resolution near the endwalls. Thus, in addition to the total pressure rake measurements, a miniature Kiel head total pressure probe (United Sensor KAC-type) was traversed in small radial increments downstream of each of the stator vane rows. This probe features a 0.063 in. outer diameter Kiel head and was paired with a L.C. Smith precision probe positioner to incrementally achieve the desired plunge locations with position feedback. The probe accommodates a yaw and pitch acceptance cone of greater than ±40 degrees, but the probe was aligned with a representative mean flow angle. The pressures from this total pressure probe were measured using a Scanivalve 3217 module with a 5 psid range.

2.4.2. Time-Resolved Total Pressure at Rotor Exit

In addition to the steady total pressures measured at positions downstream of the stator vane rows, time-resolved total pressure measurements were also acquired at the rotor exit planes. A custom-designed fast-response total pressure probe incorporates a Kulite LQ-062 subminiature pressure transducer embedded in a miniature Kiel head with a 0.083 in. outer diameter and a 0.067 in. inner diameter (Figure 2.9). The sensor has a 5 psi maximum range with an electronically sealed gage reference condition. This transducer also includes a standard B-type protective screen, therefore reducing the natural frequency of the sensors to approximately 20 kHz. A separate pressure chamber designed for this probe provided the ability to calibrate the sensor at prescribed intervals over the 0-5 psi, range and a least-squares linear fit was applied to the calibration results. The sensor was balanced with the acquisition of a zero gage pressure reading prior to each calibration, and similarly before and after each test. As with the steady total pressure measurements, an L.C. Smith precision probe positioner was used to achieve the desired plunge positions.

The excitation and amplification for this fast-response pressure sensor was provided by a Precision Filters 28000 chassis with four 28118 full bridge amplification cards, each of which is capable of managing eight channels for a total of 32 simultaneous operating sensors. Each of the channels in the Precision Filters system is independently managed through a manufacturer-designed GUI to adjust the DC offset, gain, and on-board analog filter characteristics. The sensor signals were then digitized using an NI PXIe-1073 chassis utilizing two 16-channel PXIe-6358 modules, each capable of simultaneous sampling of up to 1.25 MHz per channel, via NI BNC-2110 connector blocks.

Figure 2.9: Fast-response total pressure probe.

2.5. Over-Rotor Static Pressure Measurements

Time-resolved static pressures over the rotor tips were measured using a custom-designed array implementing flush-mounted fast-response pressure transducers. This array incorporates 25 Kulite XCS-062 subminiature pressure transducers (having an outer diameter of 0.066 in.) with a 5 psig range. These XCS-series transducers feature high-sensitivity piezoresistive sensing elements, maximizing the resolution of the measurements. These sensors were installed with standard B-type screens for protection of the sensing elements, but the new sensors were filled with additional silicon material to reduce the cavity size behind the screen and allow for the greatest allowable frequency response. As a result, a natural frequency on the order of 30 kHz is expected for these new sensors.

During the design process, a specific effort was made to accommodate all sensors in one axial row. Some previous authors have utilized a method of offsetting sensors in two or more axial rows, separated by some angle in the pitch-wise direction, to accommodate more axial resolution (Yoon et al., 2006; Shin et al., 2008; Courtiade and Ottavy, 2012). However, such sensor orientations can introduce complications in the measurements for multistage machines, as the wakes propagating from upstream stators and potential fields from downstream stators may affect the measurements. Understandably, this effect can be accounted for if the sensors are moved relative to the stator vanes, but it introduces an additional complication to the data acquisition and processing procedures. As an alternative, other authors have achieved maximum axial resolution by implementing a series of sensors at different axial positions, spaced periodically in the circumferential direction with respect to the rotor pitch (Levis, 2006; Sans et al., 2013). However, this method could be also be negatively affected by blade-to-blade non-uniformities, rotor eccentricity, and any associated flow variability.

The small diameter of the XCS-062 devices provided the ability to incorporate as many sensors as possible in one axial row, thereby increasing the spatial resolution of the output results. The sensors are permanently installed in a removable block which can be inserted into any one of nine frames. These nine frames represent one for each of the three rotor blade rows (R1-R3), and each of the three tip clearance configurations (TC1-TC3). The removable sensing block and one of the nine frames are shown in Figure 2.10(a).

The instrumentation block was designed to maximize the number of sensors which can fit within the space defined by the instrumentation access location over Rotor 1, which features the least axial space. Because the same fixed sensor locations are implemented for Rotor 2 and Rotor 3, whereas the axial chord of the rotors increases slightly moving from Rotor 1 to Rotor 3, the positions of the sensors change with respect to the leading and trailing edges of the blades for the three rotor rows. These sensor positions are presented for the three rotors in Table 1 as a percentage of axial chord.

Table 2.4: Flush-mounted sensor positions for each rotor as a percentage of axial chord.

Blade Row	Minimum Sensor Location [$\%c_x$]	Maximum Sensor Location [$\%c_x$]	Sensor Separation [$\%c_x$]
Rotor 1	-14.0	114.0	5.33
Rotor 2	-12.8	113.6	5.26
Rotor 3	-11.9	113.2	5.21

The excitation and amplification for these fast-response pressure sensors were supplied by the same Precision Filters system and measurement chain outlined above for the fast-response total pressure probe. Immediately prior to installation and operation in the compressor, the fast-response pressure sensors were calibrated in a custom-designed calibration chamber (Figure 2.10(b)) by prescribing a known pressure to the device. For each calibration, up to 15 data points were prescribed over the full sensing range of 0 to 5 psi. From these measurements, a least-squares linear fit was applied to the calibration data. The channels were zeroed prior to each calibration and again prior to testing, although thermal compensation and a stable measurement system reduce the day-to-day drift of a representative channel to 1 mV or less (after amplification), which corresponds to a pressure of less than 8×10^{-4} psi.

For each rotor and each tip clearance configuration, data were acquired at several loading conditions on the 100% corrected speedline. In all cases, 500 revolutions of data were simultaneously sampled to allow phase-locked ensemble averaging and other pertinent statistics.

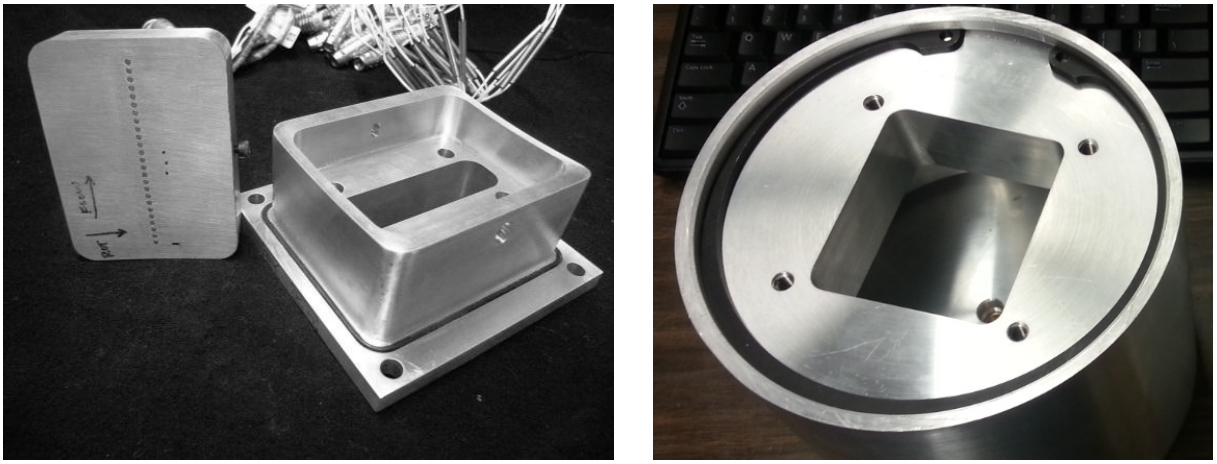

(a) (b)

Figure 2.10: Over-rotor static pressure measurement system. (a) Removable sensing block and frame; (b) Calibration chamber.

2.6. Stator Hub Seal Leakage Flow

Measurements providing boundary conditions for the flow through the knife seals in the shrouded stator cavity are desirable to create reliable computational models. In the companion study preceding this work, Berdanier and Key (2015b) showed results of mass flow rate through the Stator 3 knife seal passage, as measured by an orifice plate. To further support this effort, the hardware components for Stator 1 and Stator 2 were modified to accommodate a removable instrumentation block housing two Kulite LQ-062 (0.066 in. diameter sensing element) fast-response piezoresistive pressure transducers. One sensor was placed upstream of the two knife seals, and a second was placed downstream of the knife seals, as shown in Figure 2.11. The axial position of the sensors relative to the seals was determined by the spacing between the seals, shown in Figure 2.11 to be 0.2 in.

As part of the process leading to the selection of fast-response sensors for this application, a removable two-vane segment of Stator 2 was created by a direct metal laser sintering (DMLS) process, and a series of pneumatic pressure taps were routed through the part for measuring static pressures in the stator hub shroud cavity. Because the hardware required to install a similar two-vane segment in Stator 1 was not available, this fast-response sensor design was selected for its minimal invasive manufacturing requirements versus installation of pneumatic pressure taps through the existing stator vanes. Furthermore, this instrumentation design provides the ability to measure time-resolved pressures in the seal cavity, which has not previously been reported in the open literature.

A schematic of this two-vane segment is shown in Figure 2.12. In this figure, there are four pressure taps located on both the upstream and downstream sides of the knife seals, at the same axial positions outlined in Figure 2.11; these pressure taps are separated by 25% pitch in the circumferential direction. In preliminary tests for Stator 2 using this two-vane insert, minimal circumferential variation of pressure was identified (on the order of the uncertainty for the Scanivalve 3217 pressure scanners used for the measurements), leading to an outcome decision that one sensor on each side of the seal pair is sufficient to quantify the flow through the knife seal cavity.

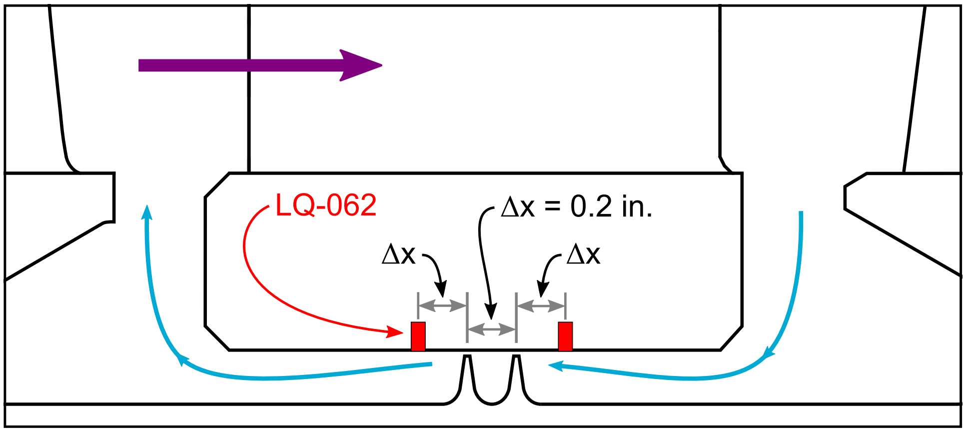

Figure 2.11: Schematic of sensor location with respect to knife seals.

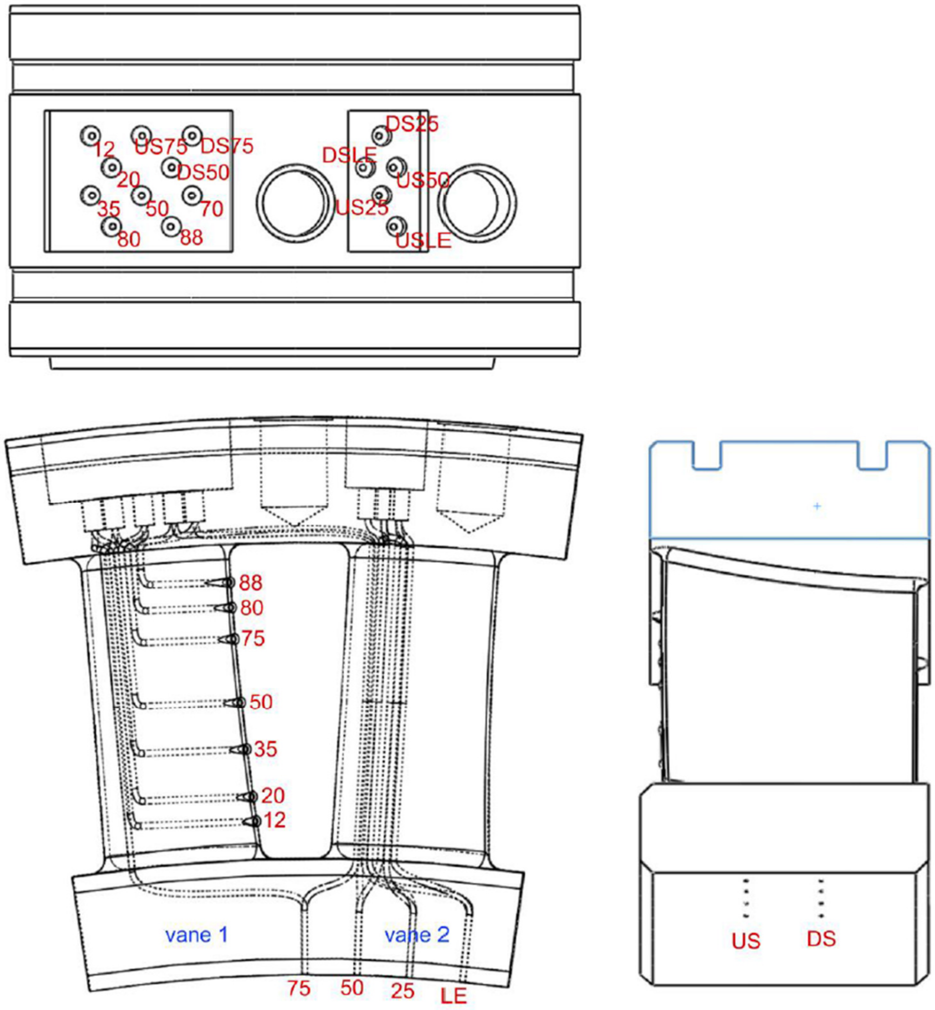

Figure 2.12: Model of two-vane instrumented segment for Stator 2 showing pneumatic pressure tap locations and routing paths (Smith, 2015).

A photograph of the removable instrumentation block installed in the stator hub shroud is shown in Figure 2.13. By using this removal block technique, the sensors could be installed from the underside of the removable block, thereby hiding the securing epoxy and any wires away from the hub shroud surface which might influence the flow through the seal cavity. Furthermore, the removable instrumentation block allows insertion of a solid “blank,” preventing exposure to conditions which could damage the sensors if their operation is not required.

For installation, the LQ-062 sensors were temporarily secured in place with a small amount of quick-bond adhesive, and then an epoxy (Loctite Ablestik 285 resin cured with Loctite Catalyst 23LV) was used to back-fill over the sensors and the wires. Once cured, this epoxy back-fill provided a solid support for the pressure transducers.

The wires for the fast-response pressure sensors (four wires per sensor) were routed through an hole in the upstream side of the stator hub shroud (the upstream side of the stator was selected for this hole because of the “reversed” flow direction of the flow through the cavity, meaning that the wires would not act as a “trip” for the flow entering the cavity at the downstream side. Then, the wires were routed up the leading edge of an adjacent vane (to minimize the potential impact of the wires on the vane surface) to an egress hole in the casing typically used for instrumentation access. The lead wires were secured to each surface along this routing path using Micro-Measurements M-Coat A protective coating. The thin diameter of the 36 AWG lead wires ensured minimal protrusion from the surface after they were secured. A photograph, Figure 2.14 shows this wire routing. Custom-length lead wires on the sensors ensured that the temperature compensation module for each sensor would be outside the compressor casing. In addition, silicone RTV was used to fill and smooth any cavities created by the fasteners (see Figure 2.13) or for wire egress.

Prior to installation and operation of the removable instrumentation block, the sensors were calibrated over the full operating range of the devices using a modified version of the calibration chamber shown in Figure 2.10(b). Extensive tests were conducted to verify linearity and repeatability of the sensor calibrations after installation in the removable sensor block. Ultimately, data were collected at all four corrected speeds (100%, 90%, 80%, and 68%) for the baseline tip clearance only, TC1. Specific measurements were collected at the same loading conditions defined by the compressor map data outlined by Berdanier and Key (2015b) to supplement these results and provide additional boundary conditions for computational simulation comparison studies.

Figure 2.13: Photograph of removable sensor block installed in stator hub shroud.

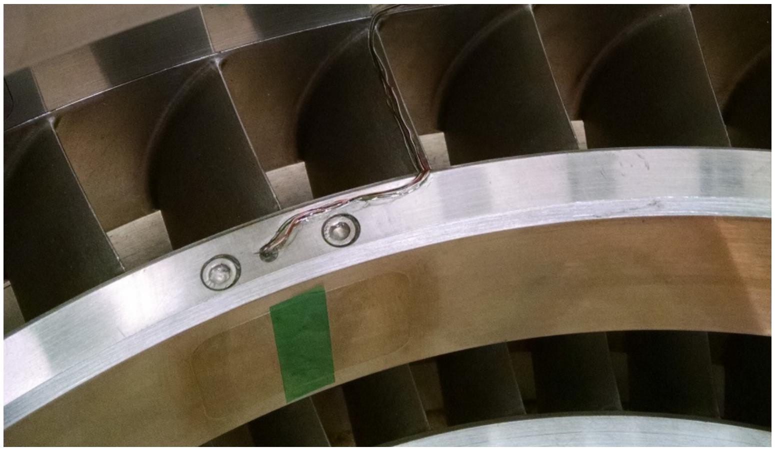

Figure 2.14: Photograph of wire routing on upstream face of hub shroud and along leading edge of adjacent stator vane to wire egress hole in casing. Clean-release protective tape shown here covering the sensors from damage was removed prior to operation.

CHAPTER 3: RESULTS AND DISCUSSION

3.1. Overall Compressor Performance

In the initial phase of this study (Berdanier and Key, 2015b), compressor performance data were collected at four corrected operating speeds (100%, 90%, 80%, and 68%) with each of the three tip clearance configurations (TC1-TC3). For each of the four speedlines, data from different tip clearance configurations were collected at equivalent corrected mass flow rates for initial comparison.

Benchmark compressor map data are presented in Figure 3.1. On the abscissa of Figure 3.1, the corrected inlet mass flow rates have been normalized by the value at the nominal loading point. Each measurement point in Figure 3.1 is calculated from area-averaged rake measurements collected from the seven-element total pressure rakes at 20 equally-spaced vane positions across one vane pitch. In this figure, the overall total pressure ratio (TPR) across the compressor is calculated as the ratio of radially and circumferentially area-averaged total pressures from axial planes 1 and 9 in the Figure 2.5 schematic:

$$\mathrm{TPR} = \frac{P_{o,9,\mathrm{AA}}}{P_{o,1,\mathrm{AA}}}. \tag{3.1}$$

In Figure 3.1, five operating points from the 100% corrected speedlines have been designated for comparison throughout this document: a low loading (LL) condition which represents a high flow rate, negative incidence condition; a nominal loading (NL) condition representing an operating point at a mass flow rate slightly higher than the peak efficiency point; a peak efficient (PE) point; a high loading (HL) condition which represents a low flow rate, high incidence operating point; and a set of conditions near the stall point (NS) which have a stall margin of approximately 5%. For this study, the stall margin (SM) is defined as follows:

$$\mathrm{SM} = \frac{\left(\frac{\mathrm{TPR}}{\dot{m}_c}\right)_{\mathrm{stall}} - \left(\frac{\mathrm{TPR}}{\dot{m}_c}\right)}{\left(\frac{\mathrm{TPR}}{\dot{m}_c}\right)} \times 100\% \,. \tag{3.2}$$

In Figure 3.1, the final point at the top of each speedline (the lowest flow rate condition) is not a 20-point traversed point, but rather a representative location of the stall point for the compressor at that operating speed. Once the stall point is identified in a preliminary run, it is subsequently approached slowly through incremental throttle movements to determine the mass flow rate and pressure rise locating the stall point. An approximate representation of the stall point with respect to the traversed points on the rest of the speedline was determined by stalling the compressor in several stator vane positions with respect to the fixed rake positions. The dotted line connecting these points represents a stall line for the specific tip clearance configuration.

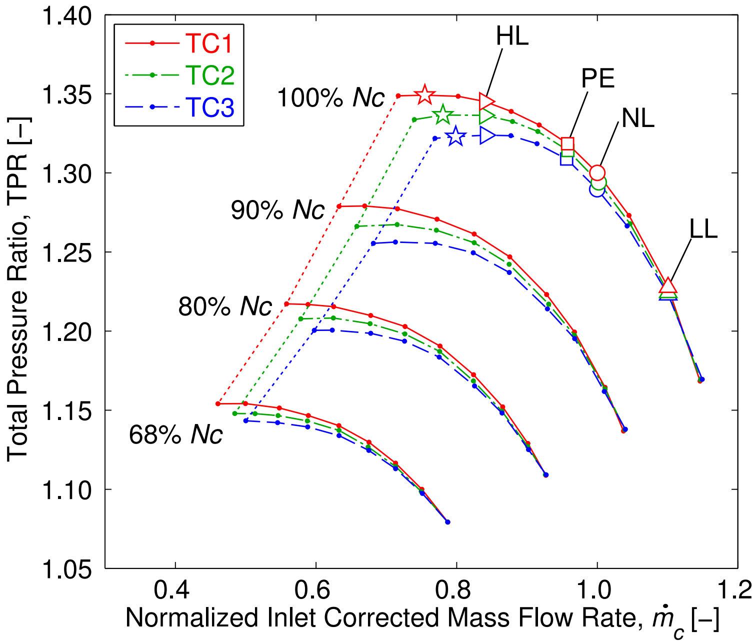

Figure 3.1: Compressor total pressure ratio map.

3.2. Steady Total Pressure Traverses at Stator Exit

To supplement the measurements collected downstream of the stator vanes using the total pressure rakes (see Berdanier and Key (2015b)), a series of detailed traverses were conducted with a miniature Kiel head total pressure probe. These measurements consisted of up to 30 radial plunge positions (at least four times the resolutions from the rake), with an emphasis on capturing the flow features in the endwall regions, as well as a higher resolution of 25 pitch-wise positions with respect to the stationary vanes. The companion study conducted by Berdanier and Key presented results from these measurements for TC1 and TC3, but additional measurements collected for TC2 are now added to the data set. A considerable outcome from the previous study showed that tip clearance effects cannot be assumed to be linear, and therefore, the addition of detailed measurements at an intermediate clearance value, TC2, provides a crucial supplementation for the previous data set. These TC2 data are presented in the context of TC1 and TC3 to identify trends across all three clearances: Stator 1 data in Figure 3.2 and Figure 3.3 for NL and HL, respectively; Stator 2 data in Figure 3.4 and Figure 3.5 for NL and HL, respectively; Stator 3 data in Figure 3.6 and Figure 3.7 for NL and HL, respectively.

Furthermore, the addition of steady total pressure traverses at stator exit planes for TC2 adds to the comparison set of flow visualization photographs collected in this facility (Smith and Key, 2015; Berdanier and Key, 2015b). These photographs are included here again for comparison purposes: Figure 3.8 and Figure 3.9 for NL and HL, respectively.

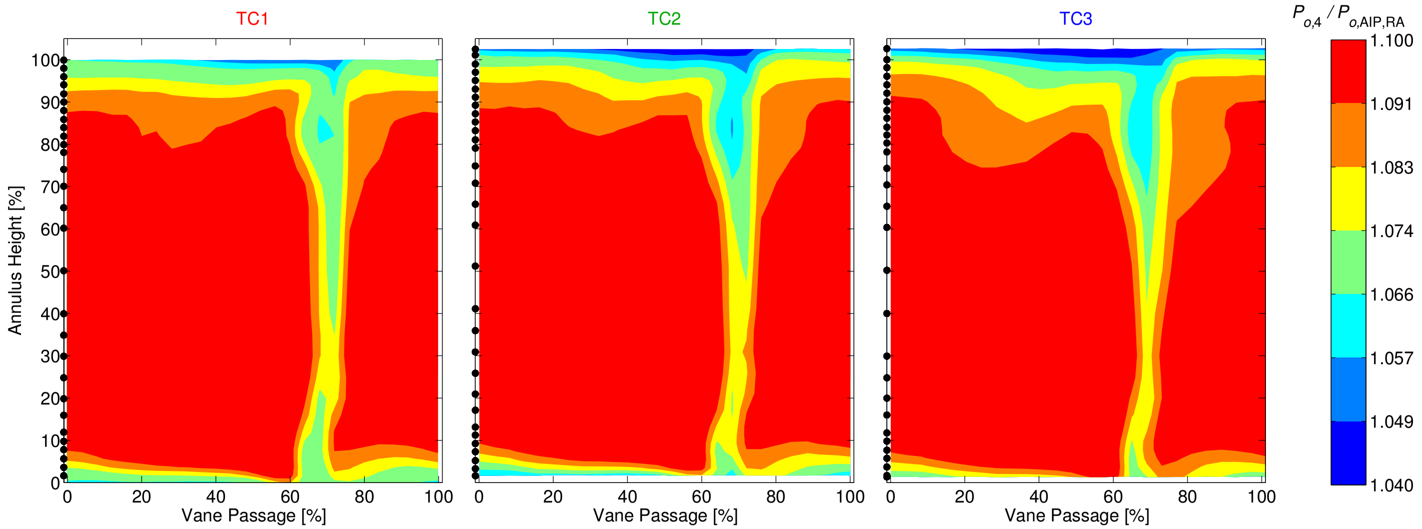

Figure 3.2: Detailed total pressure traverses at Stator 1 exit, NL.

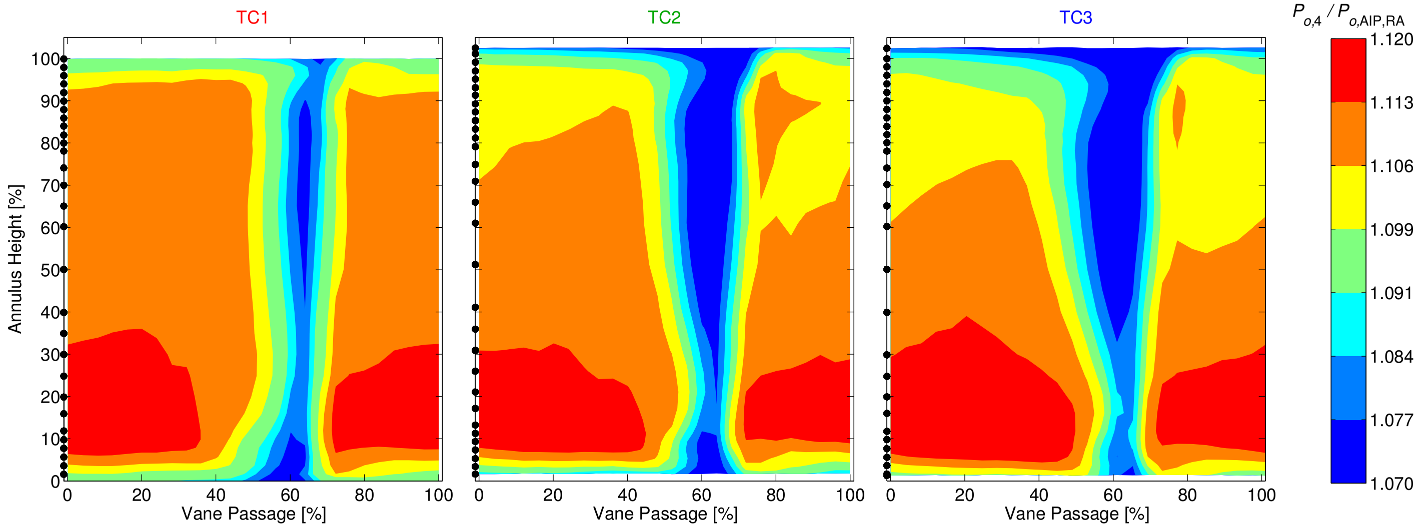

Figure 3.3: Detailed total pressure traverses at Stator 1 exit, HL.

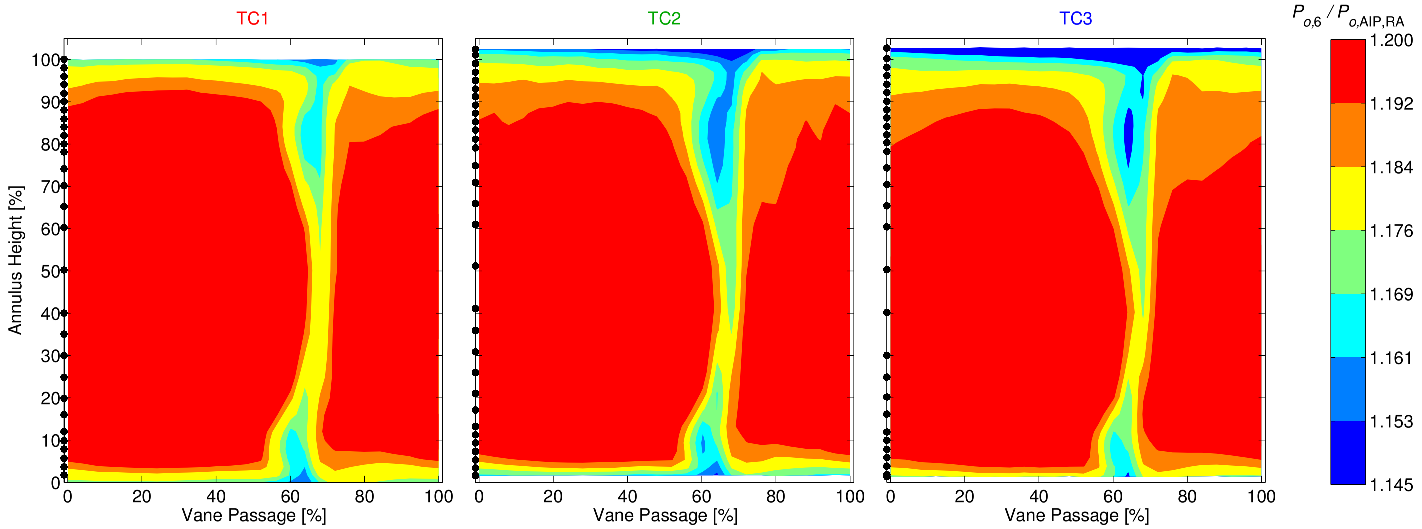

Figure 3.4: Detailed total pressure traverses at Stator 2 exit, NL.

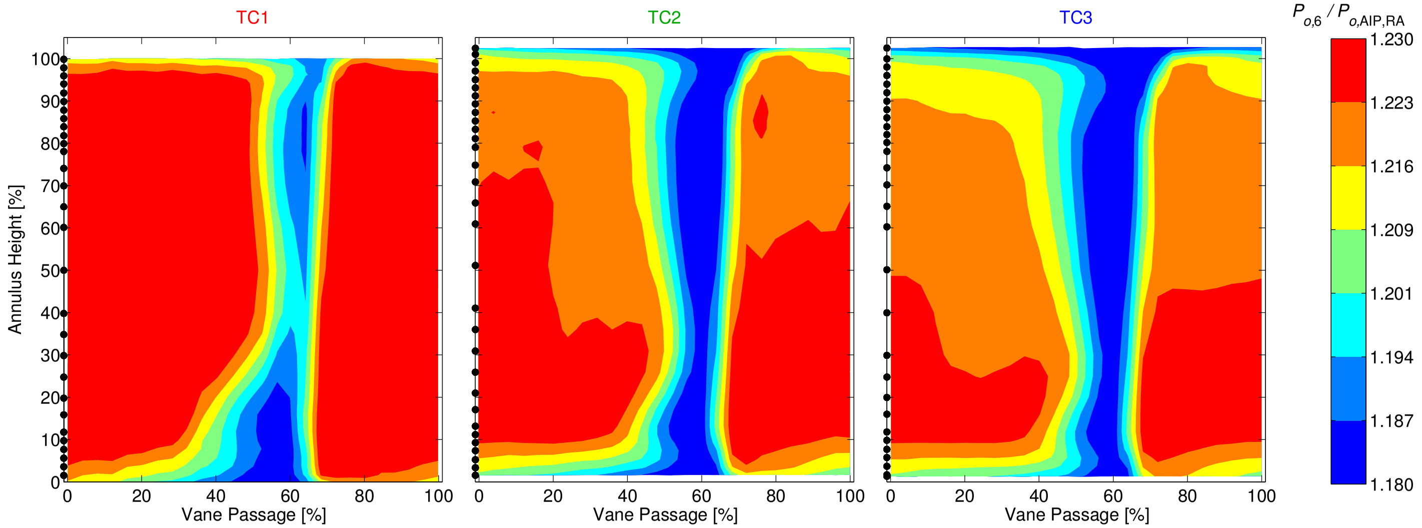

Figure 3.5: Detailed total pressure traverses at Stator 2 exit, HL.

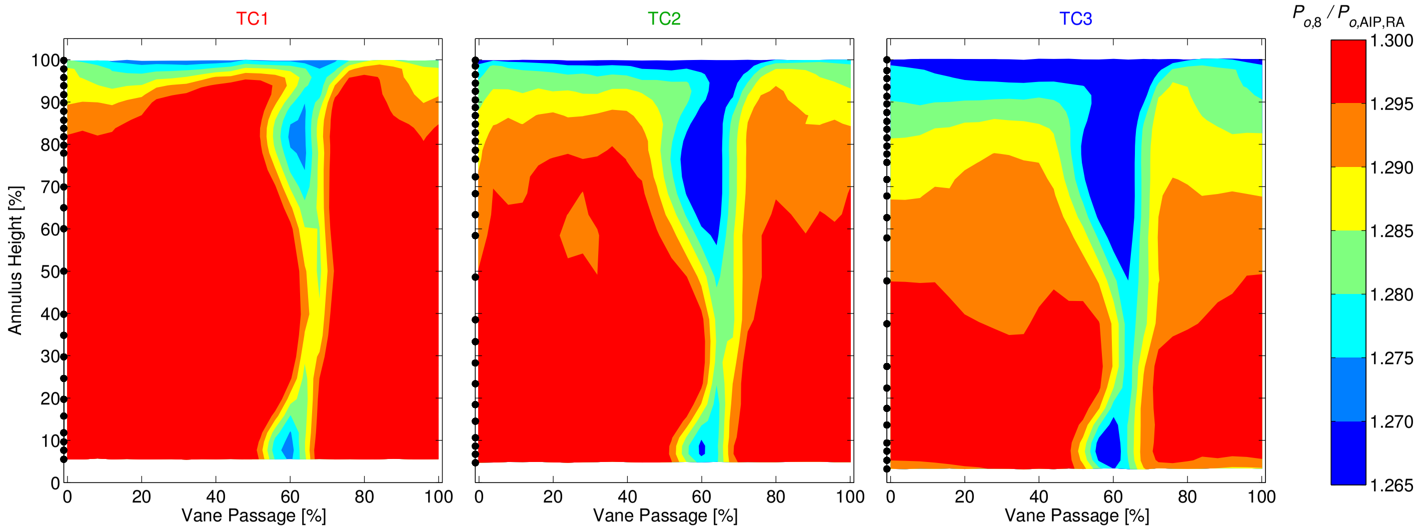

Figure 3.6: Detailed total pressure traverses at Stator 3 exit, NL.

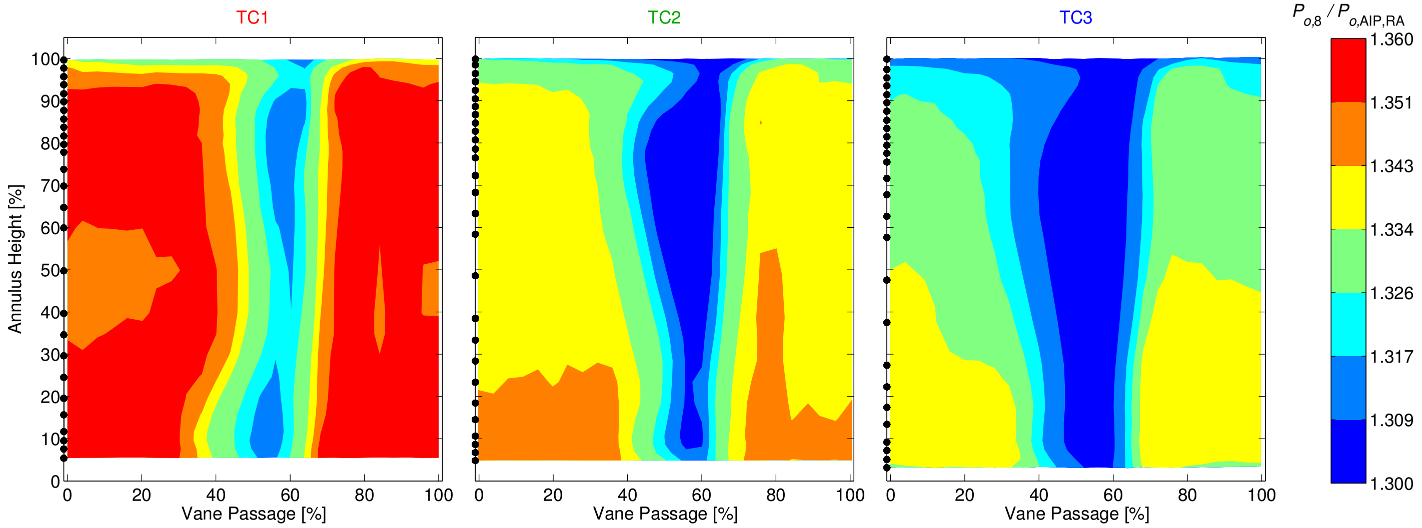

Figure 3.7: Detailed total pressure traverses at Stator 3 exit, HL.

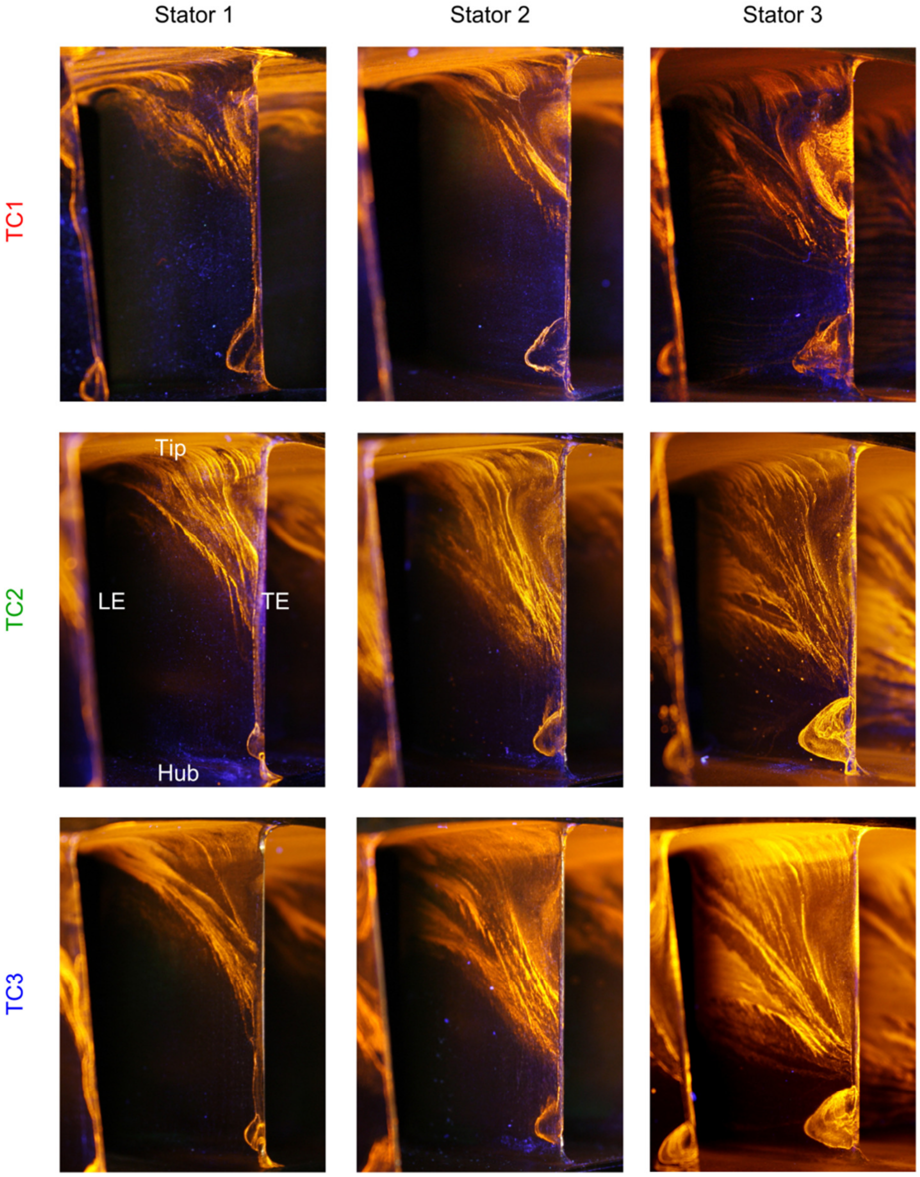

Figure 3.8: Flow visualization of vane corner separations at NL for TC1 (top), TC2 (middle), and TC3 (bottom).

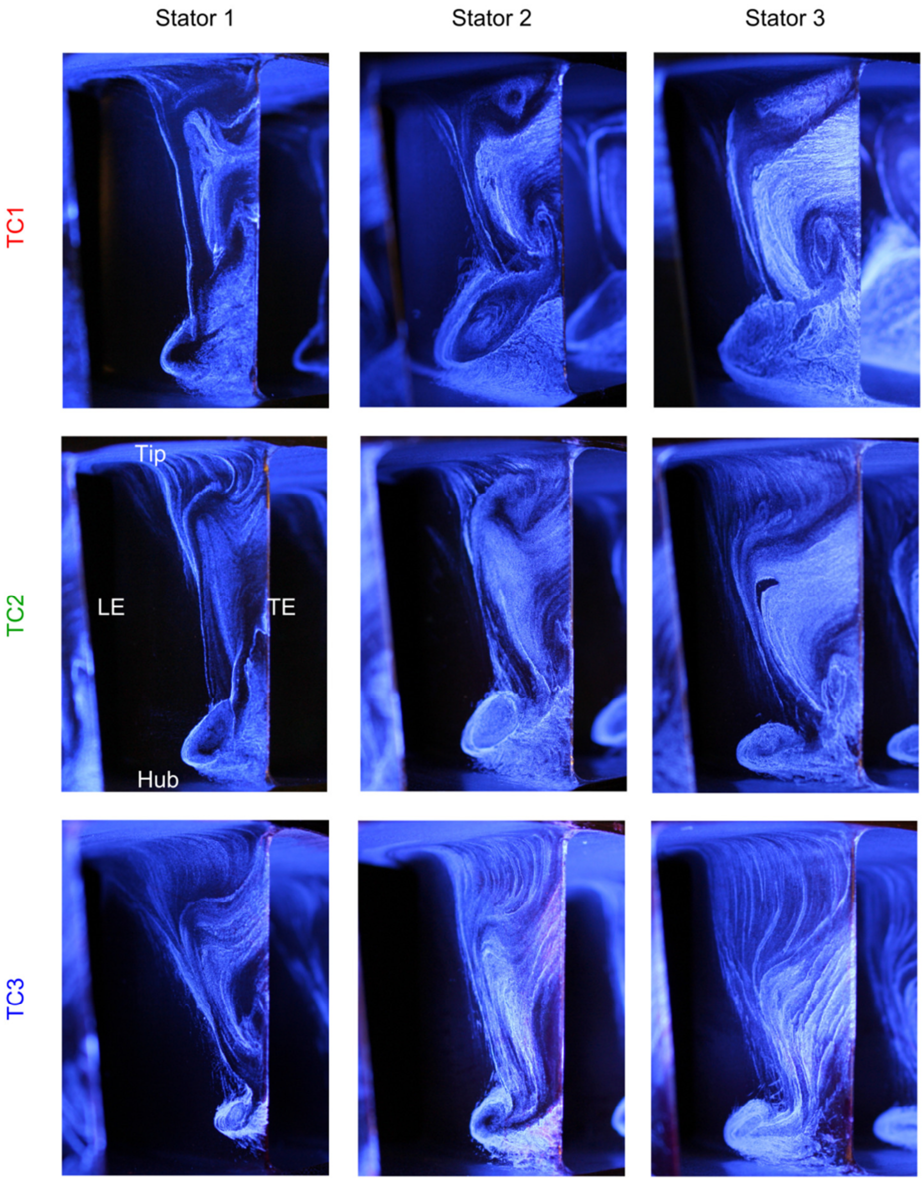

Figure 3.9: Flow visualization of vane corner separations at HL for TC1 (top), TC2 (middle), and TC3 (bottom).

3.3. Time-Resolved Total Pressure Traverses at Rotor Exit

In a companion study, Berdanier and Key (2015b) presented time-resolved total pressure measurements for this compressor under the smallest and largest clearances, TC1 and TC3. Here, additional data are presented which fill the gap for TC2 and facilitate a series of future assessments considering linear trends of calculated parameters with increasing rotor tip clearance.

For these time-resolved measurements, the data were phase-locked using a once-per-revolution (1/rev) signal. By this process, a phase-locked ensemble average (EA) pressure is calculated from N revolutions of data using:

$$\langle P(t_i)\rangle = \frac{1}{N}\sum_{k=1}^{N}[P(t_i)]_k \,. \tag{3.3}$$

In addition to the phase-locked ensemble average, the root-mean-square (RMS) pressure is defined with respect to the ensemble average:

$$P_{\mathrm{RMS}}(t_i) = \sqrt{\frac{1}{N}\sum_{k=1}^{N}[P(t_i) - \langle P(t_i)\rangle]^2{}_k} \,, \tag{3.4}$$

at the i^{th} time position in a given revolution for N revolutions of data. This presentation of RMS results accommodates the identification of high unsteadiness in recirculating flow regions such as the tip leakage flow and the rotor wake.

Berdanier and Key (2015b) showed a modulation of the tip leakage flow structure (size, shape, and position) by conducting radial probe traverses at each of the 26 pitchwise positions (pp) across one vane pitch. (Of these 26 positions, 25 are *unique* positions, since one pair of positions, pp1 and pp26, are periodic with respect to the vane pitch.)

These RMS measurements are presented in the following figures: Rotor 1 results in Figure 3.10 and Figure 3.11 for NL and HL, respectively; Rotor 2 results in Figure 3.12 and Figure 3.13 for NL and HL, respectively; and Rotor 3 results in Figure 3.14 and Figure 3.15 for NL and HL, respectively. In these figures, the RMS with respect to the ensemble average (500 revolutions, for these data) has been calculated at each circumferential vane position, and then averaged across all rotor blades (36 blades for Rotor 1) to identify an averaged rotor passage.

The IGV wake is very thin and has a minimal effect on the downstream rotor row. As a result, Figure 3.10 and Figure 3.11 show a weak modulation of the tip leakage flow across one vane pitch (following the figures in a clockwise direction, denoted by the titles pp1-pp26). In addition to the pitchwise modulation of the flowfield exemplified by the 26 circumferential measurement positions, a mean contour represents the rotor wake averaged across one vane pitch. The PS and SS are labeled in this mean contour to orient the figure.

Moving through the following conditions, each rotor shows slight variations in how the resulting RMS unsteadiness is affected by the increased tip clearance. Ultimately, it is these discernible changes that facilitate comparisons with CFD and calculation of performance metrics (such as blockage) in subsequent sections.

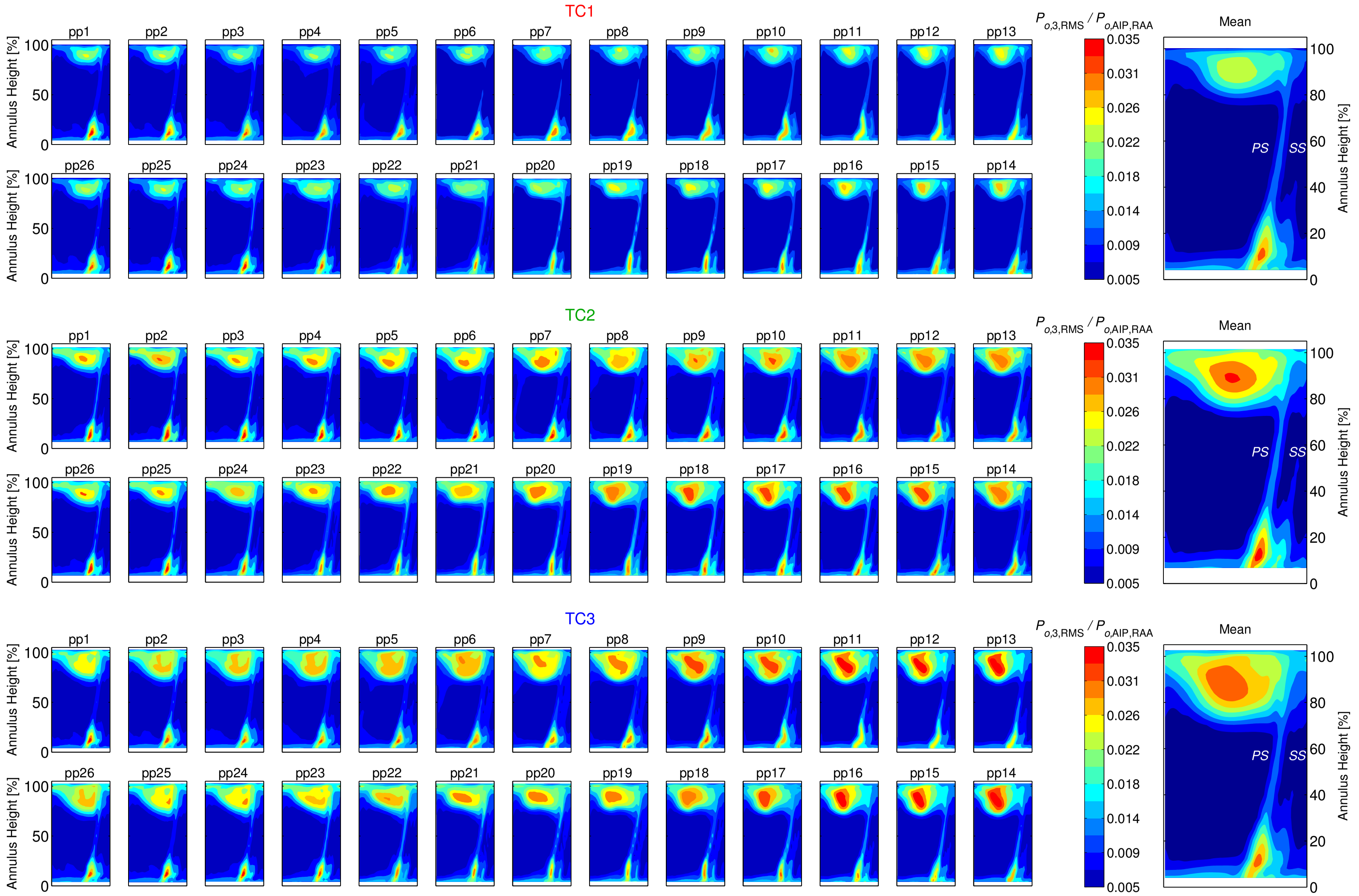

Figure 3.10: Average Rotor 1 exit flow field, in terms of RMS total pressure, at each circumferential location across one vane passage (clockwise) at NL.

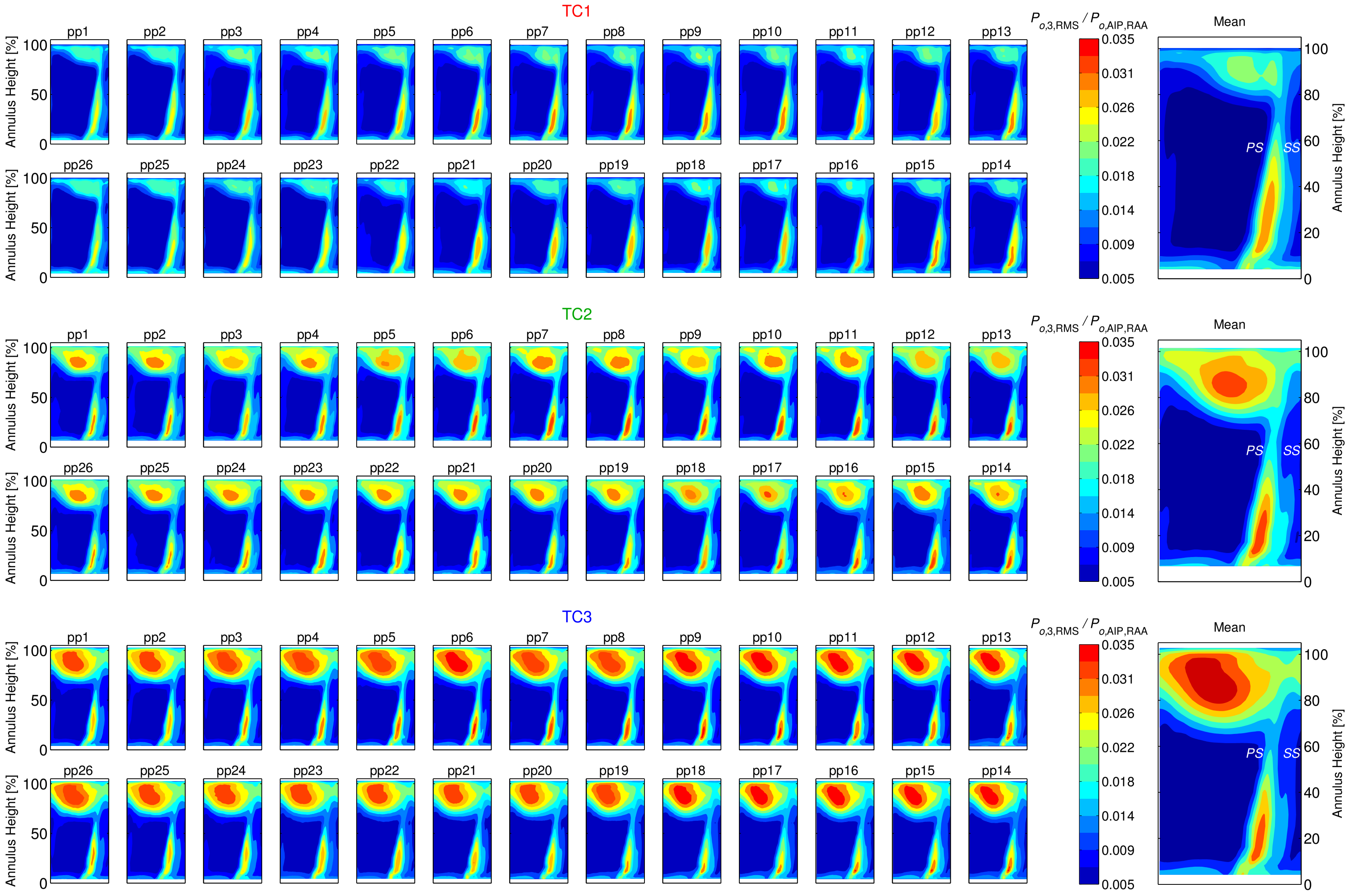

Figure 3.11: Average Rotor 1 exit flow field, in terms of RMS total pressure, at each circumferential location across one vane passage (clockwise) at HL.

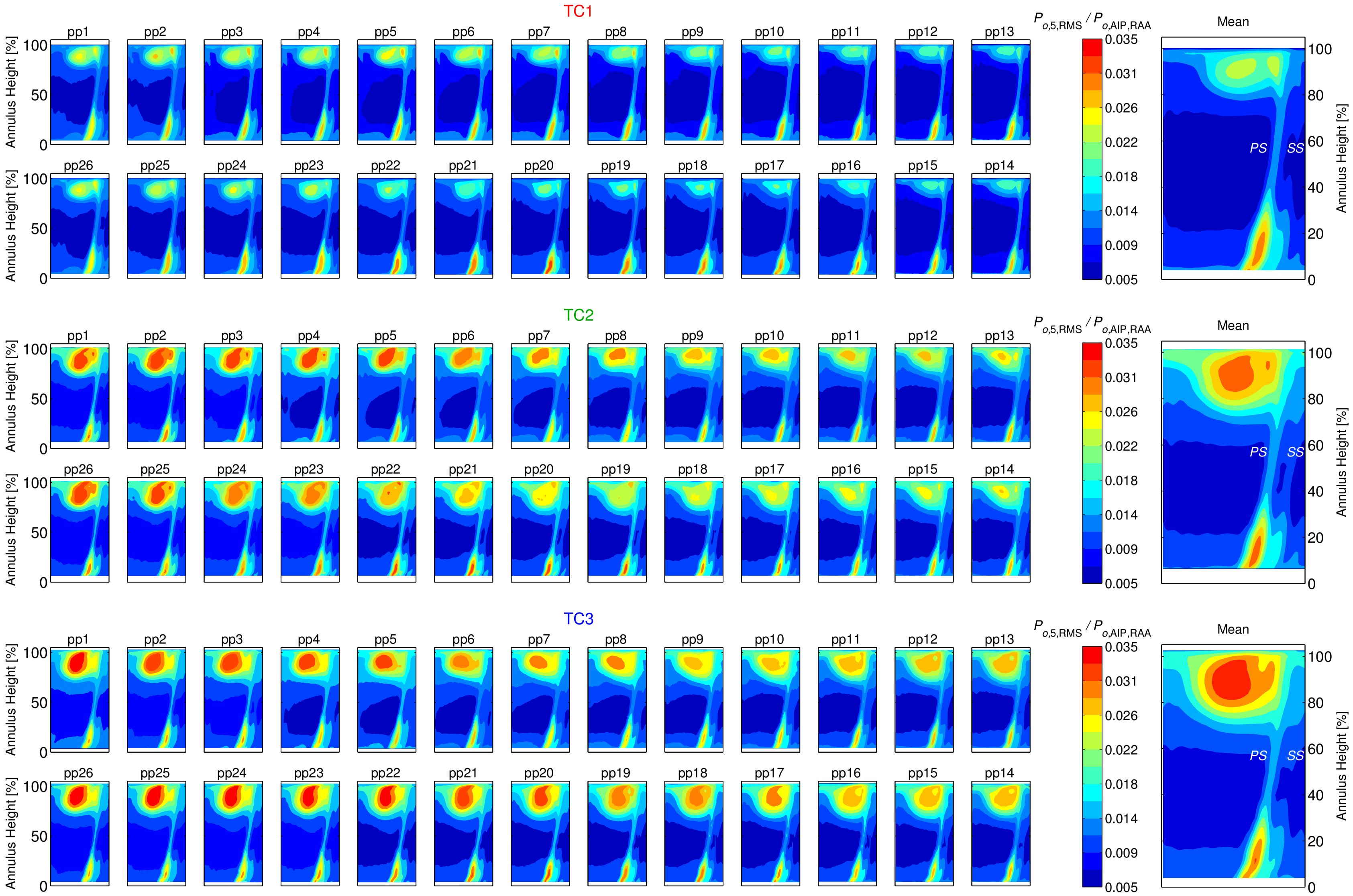

Figure 3.12: Average Rotor 2 exit flow field, in terms of RMS total pressure, at each circumferential location across one vane passage (clockwise) at NL.

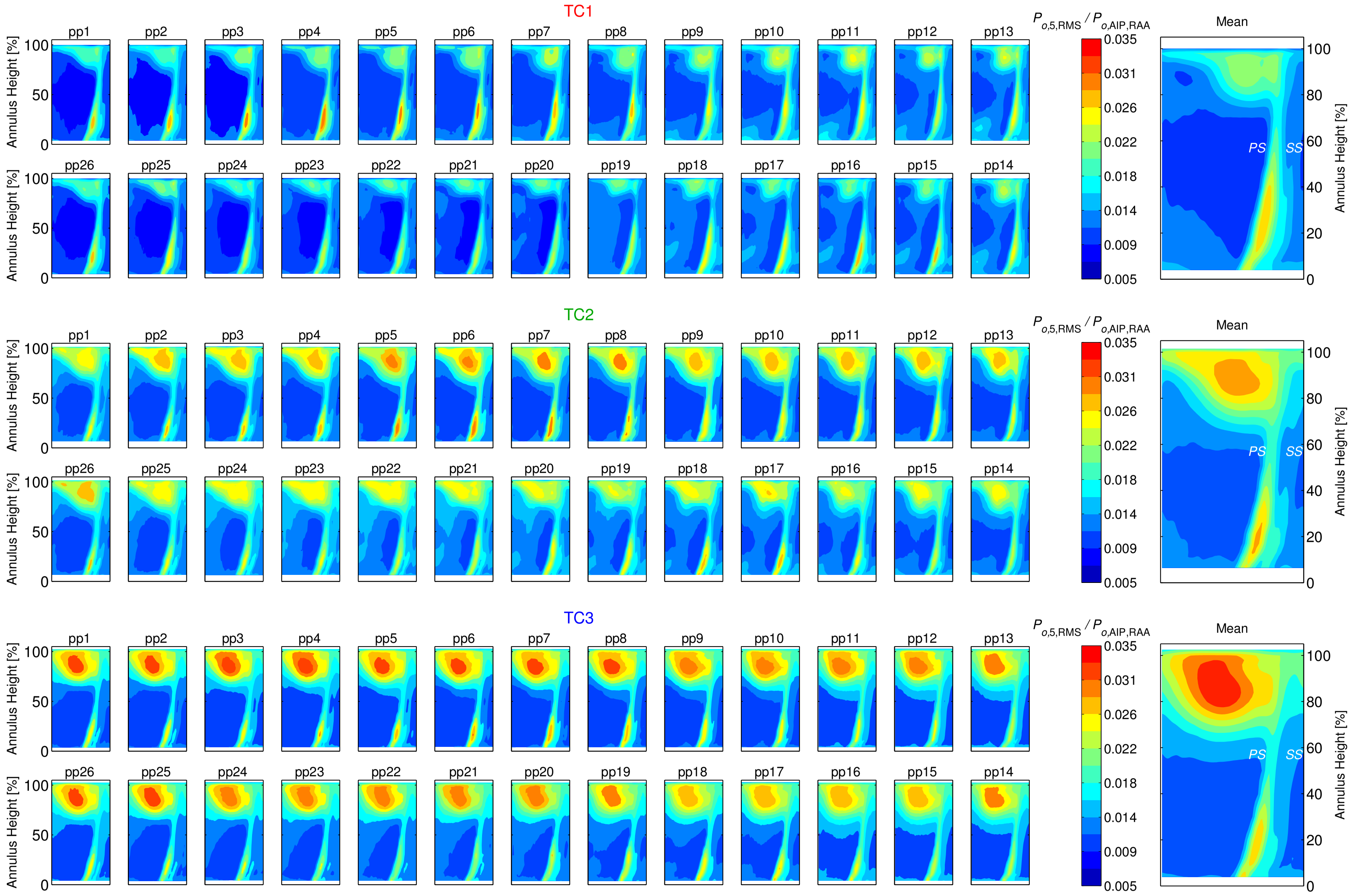

Figure 3.13: Average Rotor 2 exit flow field, in terms of RMS total pressure, at each circumferential location across one vane passage (clockwise) at HL.

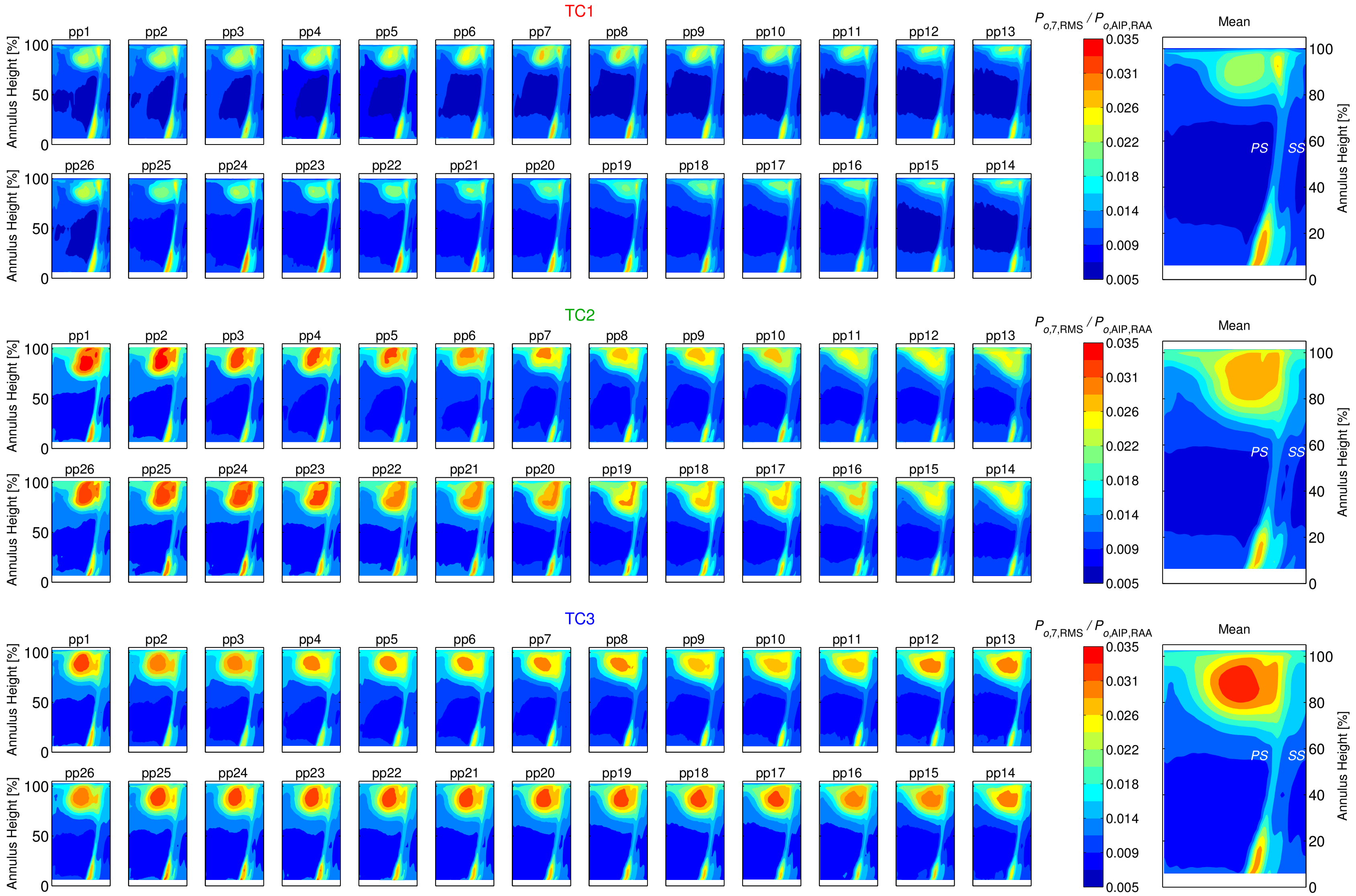

Figure 3.14: Average Rotor 3 exit flow field, in terms of RMS total pressure, at each circumferential location across one vane passage (clockwise) at NL.

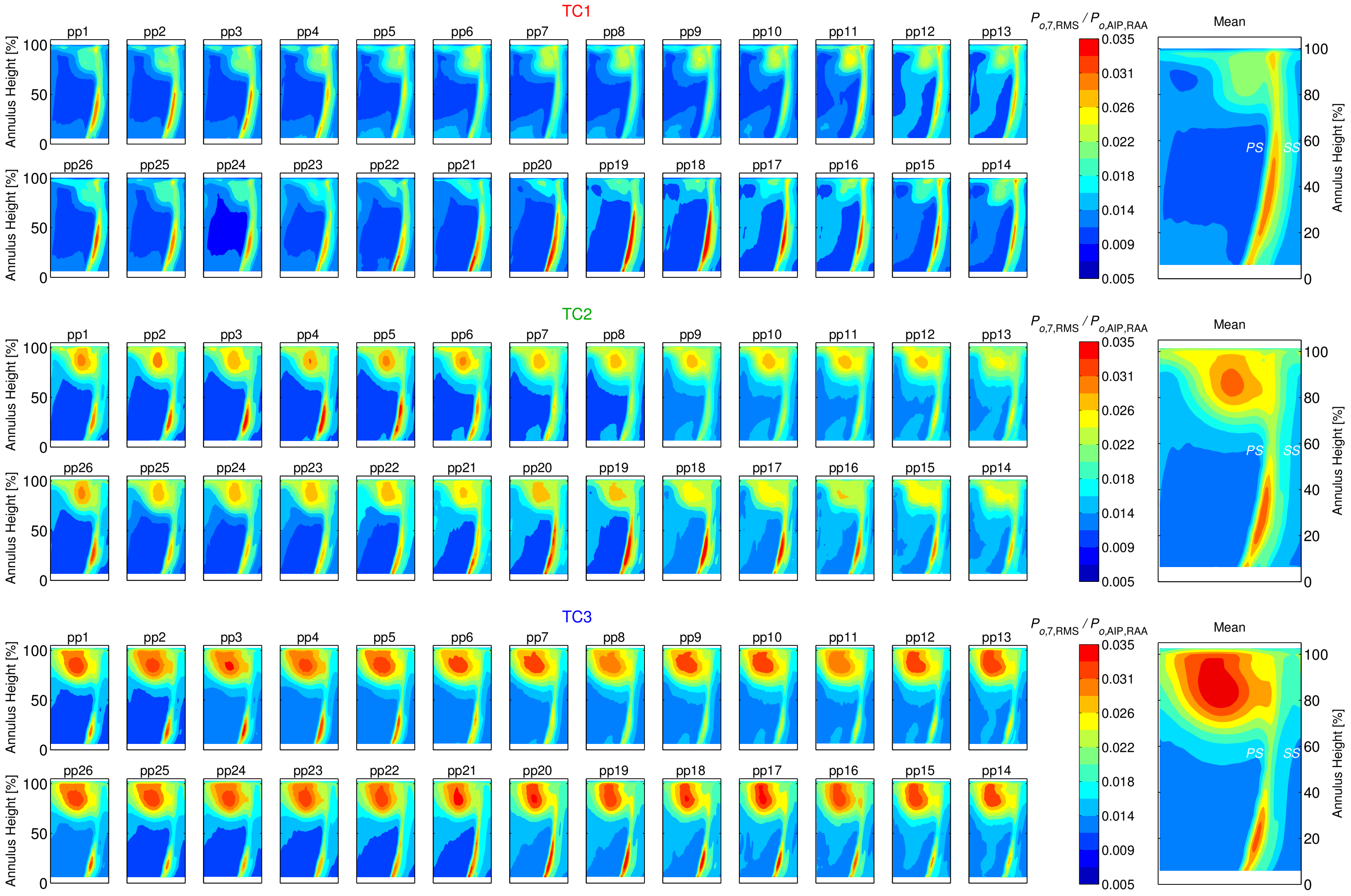

Figure 3.15: Average Rotor 3 exit flow field, in terms of RMS total pressure, at each circumferential location across one vane passage (clockwise) at HL.

Using these time-resolved pressure unsteadiness data, Berdanier and Key (2015b) outlined a method for identifying the size of the tip leakage flow at the rotor exit measurement plane. This method applies a gradient method, similar to the blockage calculation algorithm presented by Suder (1998), along with a human-guided selection tool in the plotting GUI. The method outlined by Berdanier and Key previously showed results for the smallest and largest tip clearances, TC1 and TC3, but the addition of measurements at an intermediate clearance, TC2, provides the ability to observe whether leakage flow size trends linearly with increasing clearance.

These results, Figure 3.16, show the passage-averaged value of leakage flow size (LFS) represented by the filled bars. As noted in the above figures, however, the size of the leakage flow can change considerably due to an interference of the tip leakage flow with the stator wakes propagating from upstream. Therefore, a range bar is included for each filled bar, identifying the potential variations of leakage flow size with position in the vane passage.

Evaluating these results, Figure 3.16, leads to several observations. First, the range of variation tends to be smallest for Rotor 1, which indicates the IGV wake imposes a weaker influence on the tip leakage flow than Stator 1 or Stator 2 on the downstream rotors. This observation is expected as a result of the relatively thin wake from the IGV due to the accelerating nature of the IGV.

Second, the size of the tip leakage flow does not increase linearly with clearance. This claim is more clearly identified by recasting the peaks of the filled bars from Figure 3.16 in terms of line plots, Figure 3.17. The results in Figure 3.17 are presented as a function of clearance normalized by annulus height, H, although similar conclusions are drawn if normalizing by chord or pitch. Here also, the tip clearances on the abscissa of Figure 3.17 represent the operating clearances for the test conditions of the given test campaign. In this case, though, minimal changes of ambient conditions from one test to the next lead to only minor variations of clearance value.

Based on the data in Figure 3.17 a clearance derivative for leakage flow size can be defined, as a function of normalized clearance-to-span:

$$\delta_{\text{LFS}} = \frac{\Delta \text{LFS}}{\Delta(\tau/H)}. \tag{3.5}$$

Using this definition, Figure 3.17 shows that the clearance derivatives are nearly identical for Rotor 1 and Rotor 2 at both loading conditions, NL and HL. On the other hand, though, Rotor 3 portrays a different trend, which approaches a more linear condition across clearances.

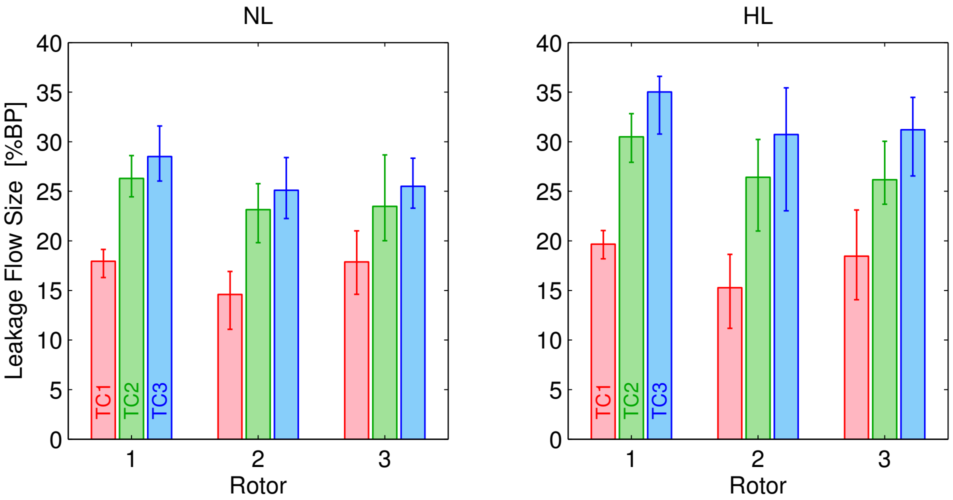

Figure 3.16: Leakage flow size approximated from total pressure unsteadiness: passage-averaged value and range.

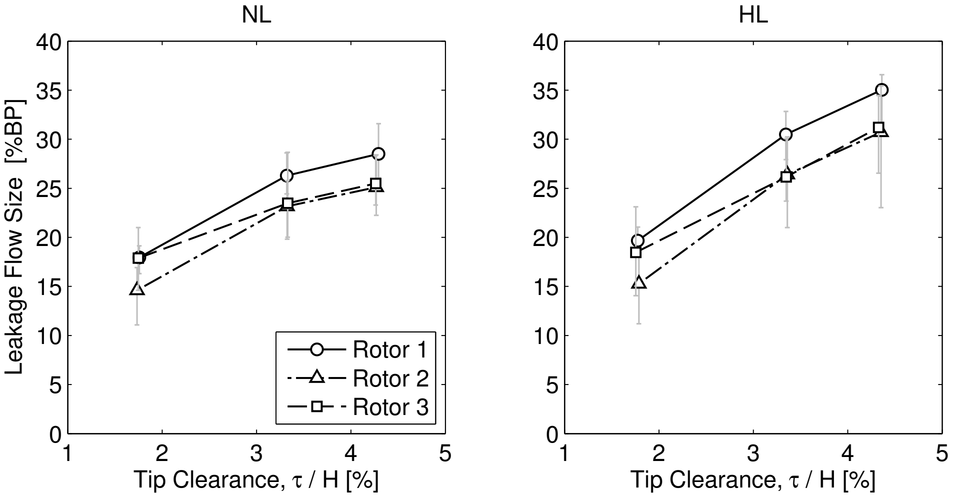

Figure 3.17: Leakage flow size versus normalized clearance, τ/H.

3.4. Quantifying Blockage from Pressure Measurements

In its simplest form, blockage represents a reduction of effective flow area or a redistribution of useful flow velocity. Through its fundamental relationship with displacement thickness, the blockage parameter depends on a measured velocity profile. Compared to basic pressure measurements, however, velocity measurement techniques prevalent in turbomachinery applications – such as hot-wire anemometry, particle image velocimetry (PIV), and laser Doppler velocimetry (LDV) – require significantly more setup (laser-based techniques), calibration (thermal anemometry), operation, and processing time. Thus, the capability to define a blockage parameter using steady and time-resolved pressure measurements would unlock new opportunities for evaluating tip leakage flows, stage matching in multistage compressors, and the overall influence on compressor stall inception. With this in mind, a series of techniques were developed for calculating blockage using steady and time-resolved pressure measurements.

Three-component time-resolved velocity measurements were incorporated to validate the pressure-based blockage calculation techniques, and these data were collected using the single slanted hot-wire approach. This study implemented a Dantec Dynamics 55R02 fiber-film sensor with a 45° slant angle. Measurements were collected through a Dantec Stramware Pro frame with analog-to-digital conversion through a National Instruments PXIe-1073 system at a sample rate of 1 MHz.

To determine three velocity components, phase-locked data were processed by solving a series of non-linear equations, similar to the procedure presented by Wagner and Okiishi (1977). Additional details regarding the hot-wire processing algorithms for this specific application are outlined by Berdanier and Key (2016b).

3.4.1. Traditional Blockage Calculations

Suder (1998) outlined a calculation method for quantifying the blockage in a turbomachine through the use of velocity measurements. Through this method, Suder utilizes a two-dimensional procedure for calculating the blockage parameter, B. In this process, the blockage is defined using the effective flow area as a function of the velocity-density deficit, δ^*, in the flow region:

$$B = 1 - \frac{A - \int \delta^* dr}{A}, \tag{3.6}$$

for which A represents the geometric flow area. In Equation (3.4), the velocity-density deficit is defined through an analogy to one-dimensional boundary layer displacement thickness:

$$\delta^* = \int_0^{2\pi/\mathrm{NB}} \left(1 - \frac{V_x}{V_{x,\mathrm{inviscid}}}\right) r d\theta\,, \tag{3.7}$$

based on an assumption of $\rho = \rho_{\mathrm{inviscid}}$, for which NB is the number of blades in the blade row of interest.

To determine the inviscid velocity, spatial gradients of axial velocity are calculated in the radial and circumferential directions. According to Suder (1998), a velocity “defect region” associated with the wake and the endwall flows is then calculated by assessing the sum of gradients with respect to a cutoff value:

$$\text{Defect Region:} \quad \text{where } \left|\frac{\partial V_x}{\partial r}\right| + \left|\frac{\partial V_x}{\partial (r\theta)}\right| \ \geq \ \text{cutoff}\,. \tag{3.8}$$

For the data in the present study, spatial derivatives were numerically calculated using a central differencing scheme, with exception to the edges of the region of interest, which were calculated as single-sided differences.

An example of the defect region definition for measurements downstream of Rotor 2 in the present study is shown in Fig. 3. Specifically, the rotor exit axial velocity field in Figure 3.18(a) is evaluated according to Equation (3.6), and the corresponding defect region is marked in Figure 3.18(b). Using this defect region, the inviscid velocity is determined by a two-step process, which is graphically portrayed via the two slices defined in Figure 3.18(b). First, the radial velocity profiles are linearly extrapolated from the edge of the defect region to the wall, as exemplified in Figure 3.19(a). Second, the circumferential velocity profiles are linearly extrapolated across the wake, with a corresponding example at mid-span shown in Figure 3.19(b). Once the inviscid velocity is known, a blockage parameter is calculated at each radial plunge position. These values can then be radially-integrated to evaluate a one-dimensional representative blockage parameter for the data.

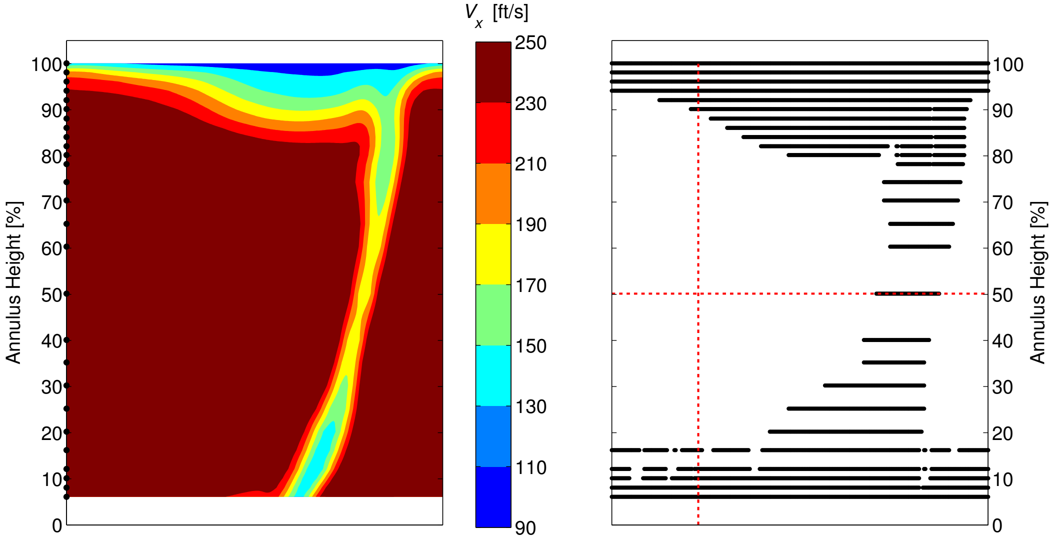

(a)

(b)

Figure 3.18: Example of identified defect region for calculating blockage from hot-wire measurements: (a) Axial velocity contours for an average blade passage, (b) Corresponding defect region marked with two slices.

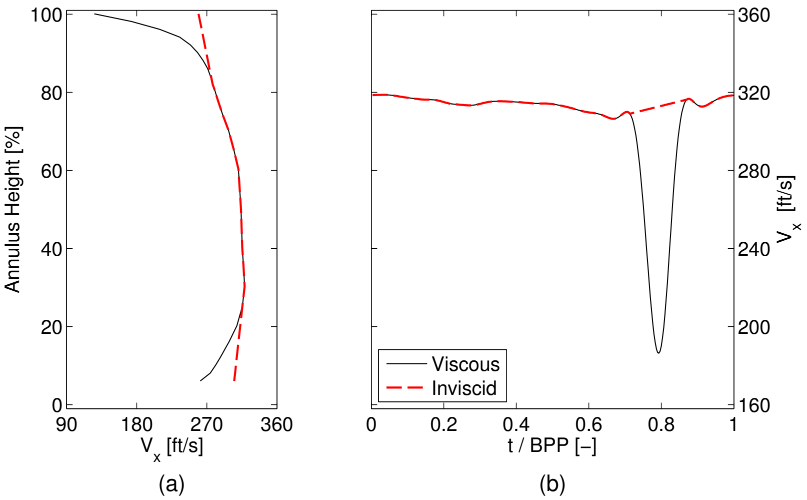

Figure 3.19: Example of inviscid velocity definition at slices marked in Figure 3.18(b): (a) Radial profile at $t/\mathrm{BPP} = 0.2$, (b) Circumferential profile at 50% span.

3.4.2. Defining Cutoff Value

From the blockage calculation process presented by Suder (1998) and outlined here, a cutoff value in Equation (3.6) must be defined. Suder notes that the selection of a cutoff threshold is arbitrary, and it has little effect on the outcome of the resulting blockage value. To evaluate this claim of insensitivity, blockage calculations were conducted for data from all rotor exit test conditions with cutoff values ranging from 2 to 6 s^{-1}. Figure 3.20 shows these results in three parts: Stage 1, Stage 2, Stage 3 in parts (a), (b), and (c), respectively. Two important takeaways are drawn from these results.

First, the calculated blockage values in Figure 3.20 are relatively insensitive to the arbitrarily selected cutoff threshold at the Rotor exit when small tip clearances are present. For reference, the data from Suder (1998) correspond to measurements from the isolated Rotor 37, for which the rotor tip clearance was 1% chord (0.84% span) or less. In cases of larger tip clearances, the tip leakage flow fills a larger portion of the blade passage, and the regions of very high gradients are smaller. This effect is also observed in the stator exit data from Figure 3.20. In comparison with Suder's isolated rotor study, the effect of cutoff value is least influential for Rotor 1, but even Rotor 1 blockage is affected when the tip clearance is increased from TC1 to TC3.

Second, in a multistage compressor, the effect of cutoff threshold can play an important role as the mean flow unsteadiness in the bulk throughflow near mid-span is higher due to the influence from upstream blade rows. This can be identified specifically in Figure 3.21, which shows radial profiles of mean total pressure unsteadiness for all three rotors. The unsteadiness for Rotor 2 and Rotor 3 in Figure 3.21(b) and Figure 3.21(c), respectively, is higher than for Rotor 1 (Figure 3.21(a)) across a majority of the span for TC1, and the effect is more pronounced for TC3 (the increased unsteadiness near mid-span for the high loading condition is even more apparent, although not shown here). For the stator exit data, the primary flow regions (i.e., outside the wake) are also affected more in the latter stages as the upstream stator wakes propagate through the compressor.

In Figure 3.20, a cutoff threshold of 4.5 s^{-1} is noted by a filled symbol on each of the lines, identifying the cutoff threshold implemented for all blockage calculations presented from this point forward. This cutoff value was selected as a position where the curves in Figure 3.20 begin to level off and the blockage-cutoff gradient approaches zero.

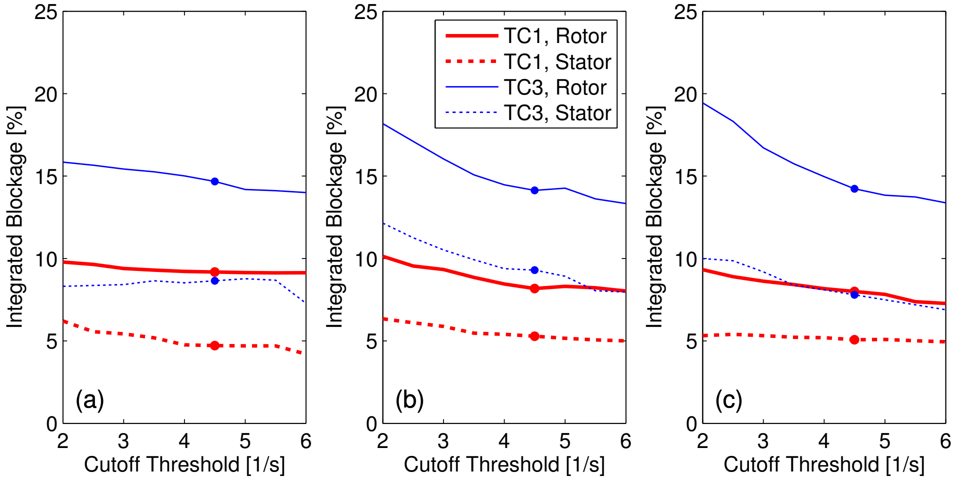

Figure 3.20: Effect of cutoff threshold on integrated blockage:
(a) Stage 1, (b) Stage 2, (c) Stage 3.

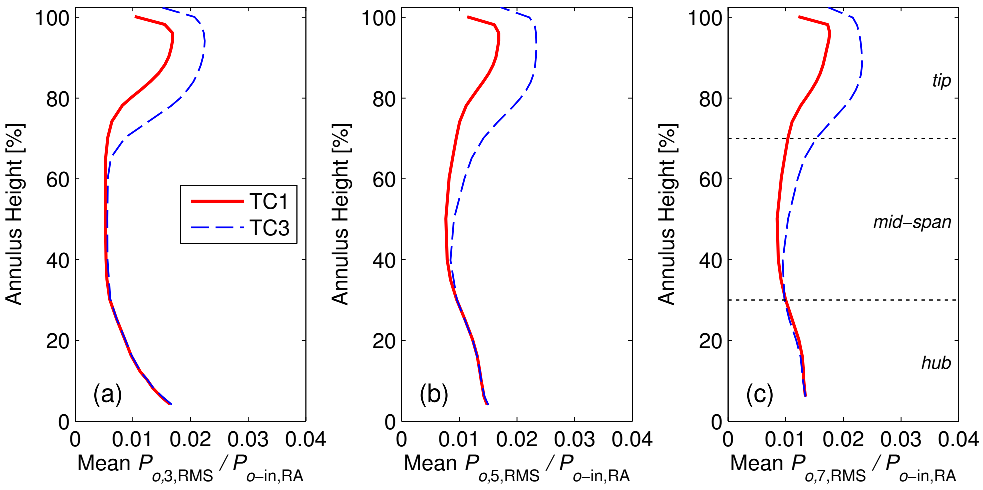

Figure 3.21: Radial profiles of mean total pressure unsteadiness highlighting increase of unsteadiness with increased tip clearance near mid-span at NL:
(a) Rotor 1, (b) Rotor 2, (c) Rotor 3.

3.4.3. Calculating Stator Exit Blockage with Steady Total Pressure Data

Figure 3.22 shows overlaid contours of steady total pressure (filled contours) and axial velocity (line contours, normalized by blade tip speed). This comparison shows excellent qualitative similarity between the velocity and total pressure data for the flow region associated with the vane wake. Thus, based on the similarity of results in Figure 3.22, a question is posed: Is it possible to utilize measurements from total pressure probes to accurately represent a blockage parameter typically calculated using velocity measurements? In general, total pressure measurements (steady or time-resolved) are less time-intensive and more cost-effective than velocity measurements using thermal anemometry, laser Doppler velocimetry (LDV), or particle image velocimetry (PIV) techniques. As a result, the development of such a technique is desirable. The answer to this question will be constructed and evaluated in the following sections.

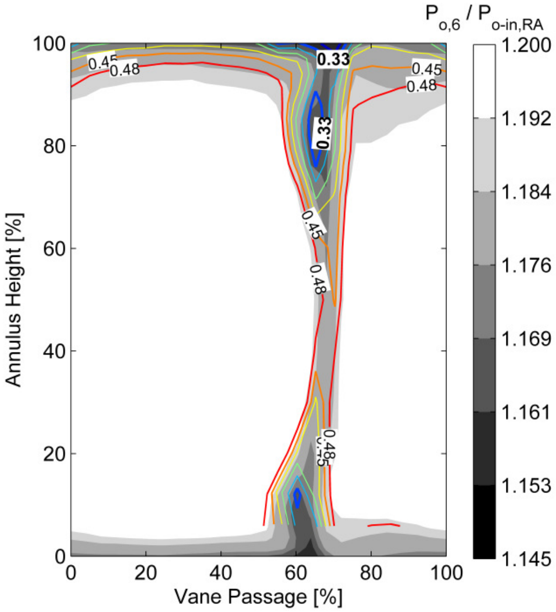

Figure 3.22: Overlaid contours of normalized total pressure (filled contours) and normalized axial velocity, V_x/U_{tip} (line contours) for Stator 2 exit at NL (TC1).

To complement these steady total pressures, static pressures were simultaneously measured from static taps in the casing. Because the Purdue three-stage compressor features constant-annulus geometry, a parallel streamline assumption is adopted.[1] Furthermore, this compressor facility operates just below the limit for incompressibility assumptions (Mach numbers less than 0.3). As a result, a simple manipulation can transform these total pressure data into first-order approximations of velocity for blockage calculations:

$$V \approx \sqrt{2(P_o - P)/\rho}\,. \tag{3.9}$$

In Equation (3.7), the density can be calculated using a combination of simultaneous total pressure, static pressure, and total temperature measurements. However, in this equation, the purpose of the density is simply to transform the units of pressure into units of velocity and to yield velocities which are of the correct order of magnitude for true velocities. Indeed, if an approximated velocity field were the desired outcome, the particular density value would be

---

[1] The three-component velocity measurements accompanying this study (Berdanier and Key, 2015b) confirm that pitch angles are on the order of three degrees or less across the entire span for the wide range of tested conditions.

important. However, for these blockage approximations, it will be shown that the exact value of density is not a necessary input. For simplicity, all total pressure data presented from this point forward utilized a density of 1.20 kg/m^3 (0.075 lbm/ft^3), a representative average air density for typical conditions at the Purdue University test facility.

Also in Equation (3.7), this approximation identifies the absolute velocity component, not the axial velocity component required for calculating blockage. At these stator exit planes, however, the absolute yaw angle, α, is small (on the order of ten degrees or less for the present machine) since the stator vanes remove whirl angle and turn the flow toward the axial direction. In its full three-component formulation, the axial velocity is defined by:

$$V_x = V \cos \alpha \cos \phi \tag{3.10}$$

for pitch angles, ϕ. However, for small pitch angles accompanying the parallel streamline assumption and small absolute yaw angles at stator exit planes, the cosine functions are approximately unity, yielding:

$$V_x \approx V\,. \tag{3.11}$$

This result in Equation (3.9) is important to the process under development here because it emphasizes that measured flow angles are not a requirement for approximating blockage from steady total pressure downstream of a stator.

After converting the total pressure measurements to an approximate axial velocity, a blockage calculation algorithm was implemented with a standard cutoff of 4.5 s^{-1}. A comparison between radial profiles of blockage calculated using the hot-wire measurements and the steady total pressure data are shown in Figure 3.23 for TC1 for Stator 1, Stator 2, and Stator 3 in parts (a), (b), and (c), respectively. These comparisons in Figure 3.23 show similar results between the two measurement techniques, on the order of one percent absolute difference for positions above 30 percent span. Absolute differences grow up to four percent near the hub region, with the largest discrepancies occurring for the NL operating condition.

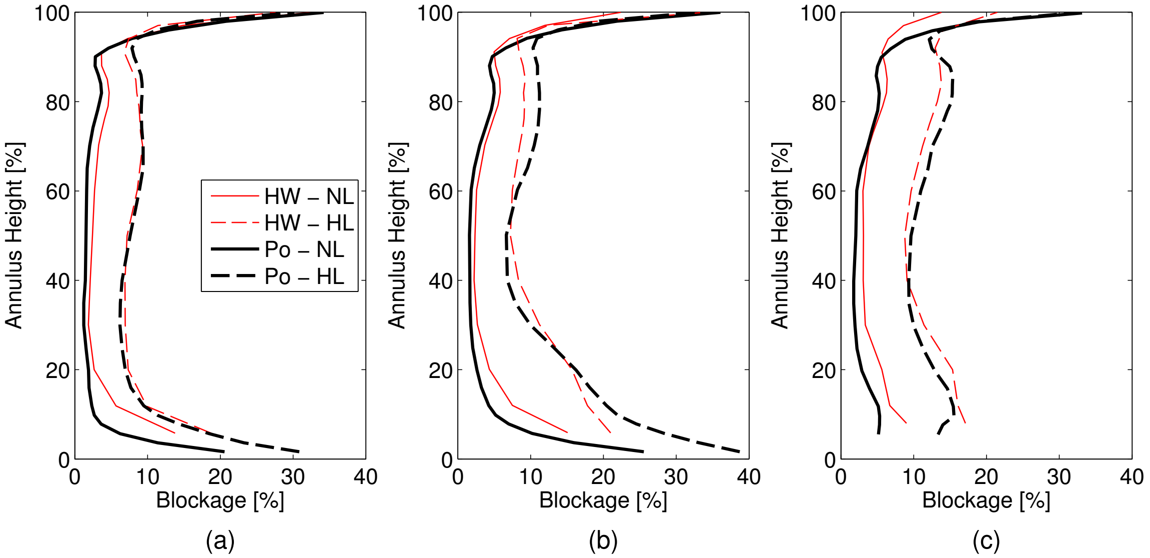

Figure 3.23: Overlaid contours of normalized total pressure (filled contours) and normalized axial velocity, V_x/U_{tip} (line contours) for Stator 2 exit at NL (TC1).

These slight differences near the endwalls are not surprising given the increased radial flow associated with corner separations and secondary flows. Thus, the small angle approximation from Equation (3.8) to Equation (3.9) is less appropriate in these regions. For further reference, the selection of a density value of 0.96 kg/m^3 (0.060 lbm/ft^3) or 1.44 kg/m^3 (0.090 lbm/ft^3) – a 20% relative change from the average density defined earlier, much larger than expected for realistic test conditions – has an effect of shifting these radial profiles by an absolute value of 0.2 percent left or right (within the thickness of the lines in the chart). This insensitivity to input density for Equation (3.7) highlights that temperature measurements are also not a requirement to implement this simplified pressure-based blockage technique.

3.4.4. Calculating Rotor Exit Blockage with Time-Resolved Total Pressure Data

To this point, a method was preliminarily introduced through which blockage may be approximated using measurements from steady total pressure measurements. However, a similar approximation is also desired for data collected at rotor exit planes. To assess this capability, Figure 3.24 shows overlaid contours of total pressure unsteadiness (filled contours) and axial velocity (line contours, normalized by blade tip speed). Parallel to the conclusion with the steady total pressure contours (Figure 3.22), these time-resolved data highlighting the blade wake and the tip leakage flow region also show qualitative similarity.

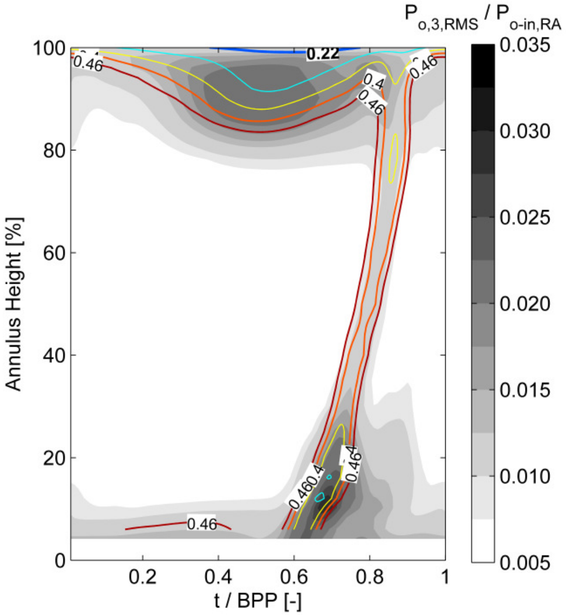

Figure 3.24: Overlaid average passage contours of normalized RMS total pressure (filled contours) and normalized axial velocity, V_x/U_{tip} (line contours) for Rotor 1 exit at NL (TC1).

Based on the Suder (1998) method for blockage calculation and the approximation introduced above for steady total pressures, a similar process can be applied to the time-resolved total pressure measurements. Unlike the stator exit data, the rotor introduces whirl to the fluid, leading to relatively high absolute yaw angles at the rotor exit. As a result, Equation (3.8) can be used to determine an approximate absolute velocity field, but it does not represent the axial velocity. Furthermore, the velocity deficit regions are less apparent in the absolute velocity, V, than the axial velocity, V_x. At the rotor exit, radial flow components may be significant through the wake and in the endwall regions, with particular contributions from the tip leakage flow region. However, for the present application these pitch angles are still on the order of five to ten degrees, even in the most extreme regions. Thus, the small angle approximation may still be adopted for pitch angles, but the same is not true for the yaw angle. As a result, the axial velocity relationship simplifies to:

$$V_x \approx V \cos \alpha \,, \tag{3.12}$$

but additional information is required to determine the yaw angle, α.

Based on the qualitative comparison in Figure 3.24, it is expected that a correlation exists between the total pressure unsteadiness and the flow angles yielding an axial velocity deficit. An example of this correlation is identified in Figure 3.25. Figure 3.25(a) shows contours of the non-dimensional total pressure unsteadiness, and Figure 3.25(b) shows the corresponding absolute yaw angle as measured by the hot-wire technique. At a given radial position, there is a linear trend between these two variables with a typical coefficient of determination, R^2, on the order of 0.8. In this case, the relationship at 30% span is shown in Figure 3.25(c). Through this relationship, the full radial distribution of non-dimensional total pressure unsteadiness can be transformed to represent a yaw angle field. Finally, this yaw angle field combines with the calculated absolute velocity distribution to determine the required axial velocity. A flowchart outlining the relationships of these parameters is shown in Figure 3.26.

These methods require additional attention if they are to be implemented with transonic applications. In particular, the determination of blockage outlined in Equation (3.5) is dependent on an inviscid density assumption, and the demonstration of these results is based on an exemplar of subsonic flow. Suder (1998) discusses the implications of the inviscid density assumption for transonic applications, noting that the density defect through a rotor wake is in-phase with the velocity defect, leading to a negligible influence on the defined defect region. However, the incorporation of density inside the integral of Equation (3.5) is expected to yield results within ten percent of the true value (less than two percent blockage for the cases presented here). As noted by Suder, this error is sufficiently small to identify trends when comparing test cases.

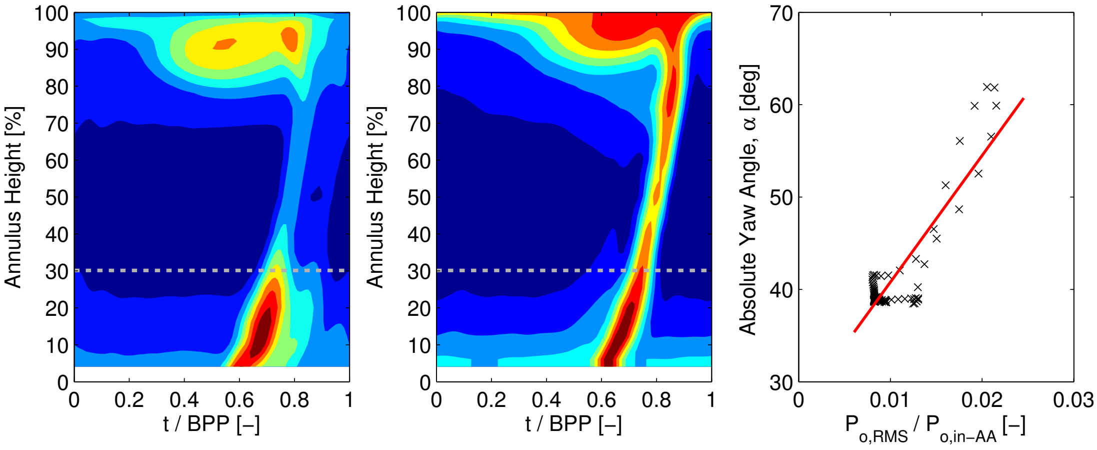

(a) (b) (c)

Figure 3.25: Example yaw angle approximation relationship for Rotor 2 exit with TC1 at NL: (a) Total pressure unsteadiness, (b) absolute yaw angle, and (c) linear relationship at 30% span.

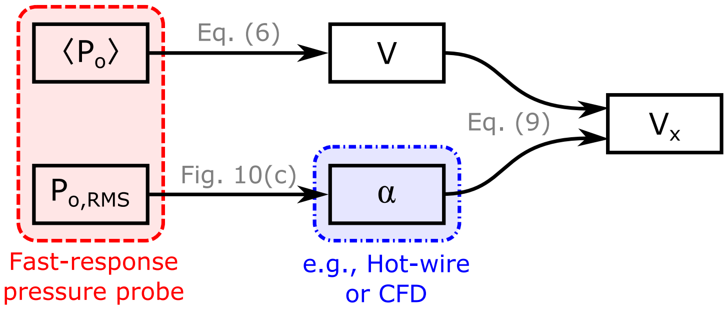

Figure 3.26: Flowchart outlining parametric relationship leading to axial velocity for blockage calculation.

This method requires limited knowledge of flow angles to determine the linear relationship shown in Figure 3.25(c). The selection of radial position for determining the relationship shown in Figure 3.25(c) is dependent on the identified results from the total pressure RMS unsteadiness.

Although any radial position will yield a nearly linear correlation between RMS unsteadiness and absolute yaw angle, the ideal position or “target zone” is selected to be adjacent to the region of high unsteadiness in the wake near the hub. This recommendation stems from an assessment of all conditions measured in this study. Because the unsteadiness in the wake is dependent on blade loading, it must be selected independently for each test case. Figure 3.27 shows an example of different spanwise target zone positions for three discrete test cases across all three rotors, three tip clearances, and two loading conditions. These selected example conditions represent Rotor 2 exit with TC1 at NL, Rotor 3 exit with TC2 at HL, and Rotor 1 exit with TC3 at HL in parts (a), (b), and (c), respectively.

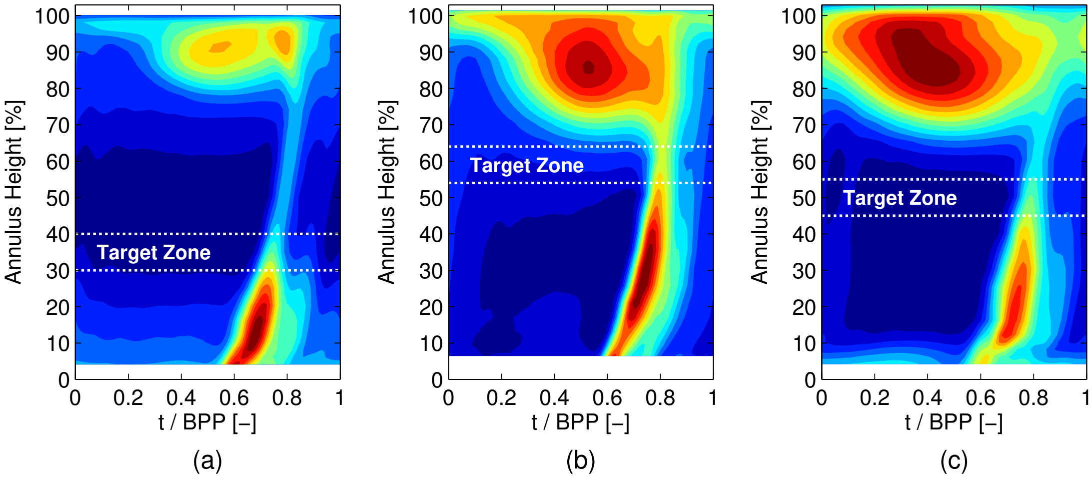

Figure 3.27: Target zone identification for several total pressure unsteadiness conditions: (a) Rotor 2 exit with TC1 at NL, (b) Rotor 3 exit with TC2 at HL, (c) Rotor 1 exit with TC3 at HL.

For these rotor exit data, the requirement of flow angle information is an added complication. In particular, if a hot-wire or other technique is required to measure the flow angle, then the velocity information is likely paired with those results. However, these results show that only one radial position is required, thereby opening additional benefits which maintain this total pressure technique as a viable approximation method. Of note, flow angle measurements at one radial position are considerably less time-consuming than a full radial traverse. Furthermore, the position of the example target zones shown in Figure 3.27 in the mid-span region and outside the high-unsteadiness wake region suggests that a simplified two-component velocity technique (e.g., X-wire) is sufficient and three-component velocity measurements are not a requirement. Finally, the mid-span positioning of these target zones also makes it possible to utilize computational fluid dynamics (CFD) results to determine the relationship in Figure 3.25(c), given that computational tools are typically more accurate in these mid-span regions than in highly three-dimensional endwall flows.

To evaluate the effectiveness of this blockage approximation scheme, Figure 3.28 shows a comparison of the blockage calculated from hot-wire data (bars) with the time-resolved total pressure approximation (markers). These blockage data are compared for the three regions – hub, mid-span, and tip – as defined in Figure 3.21. For the TC1 results at NL in Figure 3.28, the total pressure blockage approximation agrees with the hot-wire method within approximately one percent blockage or better for each of the three regions. The largest discrepancy occurs for Rotor 1 in the hub region (in the range from 0 to 30% span), with a difference of less than three percent blockage.

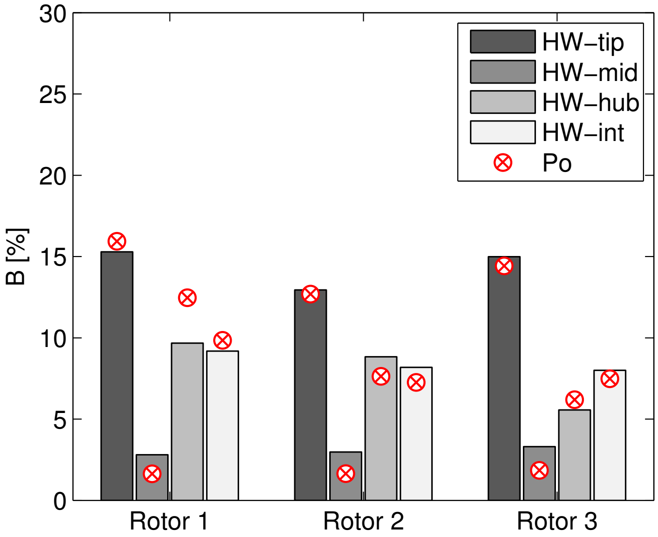

Figure 3.28: Blockage comparison from hot-wire (HW; bars) and time-resolved total pressure (Po; markers) in three radial regions (tip, mid, hub) and integrated (int) across the entire span for TC1 at NL.

3.4.5. Evaluating Blockage Schemes through the Compressor

Using the methods presented here, the integrated blockage through the compressor is evaluated using the standard velocity method and the new pressure-based methods. For this study, detailed pressure measurements were collected for all three tip clearance configurations, but hot-wire velocity data were collected only for the smallest and largest tip clearance configurations, TC1 and TC3. As a result, these comparisons provide additional insight to the blockage development in this three-stage axial compressor, without the need to invest the time for a hot-wire velocity measurement with TC2. To evaluate these comparisons, results are presented comparing the blockage through the compressor in the tip region, the mid-span region, and the overall integrated blockage.

To begin, Figure 3.29 shows the development of tip blockage through the compressor using the traditional velocity-based method from hot-wire (HW) measurements and the proposed approximations with total pressure measurements. Comparisons at nominal loading are shown in Figure 3.29(a), and Figure 3.29(b) shows high loading comparisons. From these results, several observations may be drawn. First, a pattern of increased blockage at rotor exits, and then decreased blockage at stator exits, is present for both loading conditions and all tip clearances through the compressor. This result is typical because the tip leakage flow is the primary contributor of tip blockage at rotor exit, but its influence is dispersed after passing through the downstream stator. Second, the approximated pressure-based tip blockage compares very well with the velocity-based calculations – typically on the order of one percent blockage or better. Third, the pressure-based blockage for TC2 trends closer to TC1 than TC3 at NL but closer to

TC3 than TC1 at HL. Based on this, the development of blockage in the tip region does not trend linearly with relative tip gap size, especially for the NL operating condition.

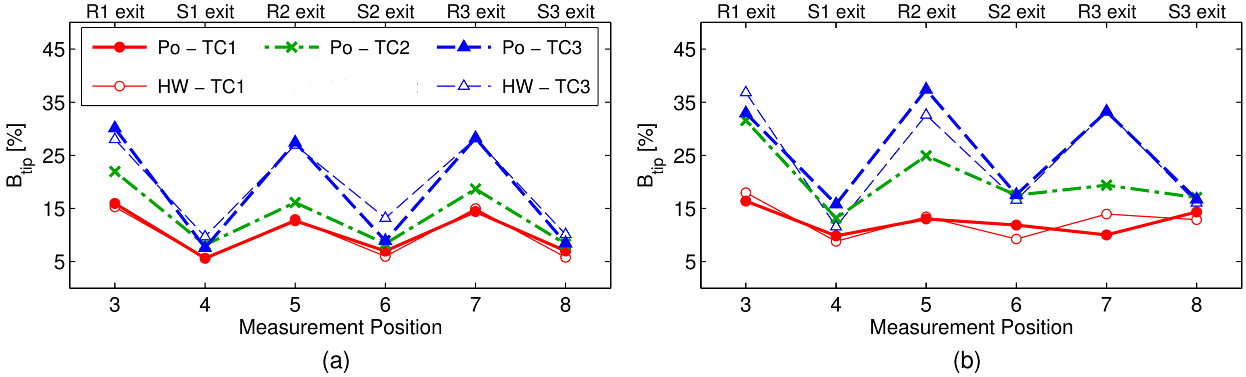

(a)

(b)

Figure 3.29: Comparison of true blockage (hot-wire) and approximated blockage (total pressure) in the tip region: (a) NL, (b) HL.

Figure 3.30 shows a similar development pattern through the compressor for mid-span blockage. For the nominal loading condition in Figure 3.30(a), the blockage changes minimally across measurement positions moving axially through the compressor. For the high loading condition in Figure 3.30(b), the up-and-down pattern is reversed from the tip region in Figure 3.29(b). Specifically, in Figure 3.30(b), the mid-span blockage is greater at the stator exit planes and then decreases at the rotor exit planes. For all conditions shown, the pressure-based blockage approximation provides a good representation of the velocity-based measurements, with mid-span blockage discrepancies typically on the order of one to two percent.

The HL results in Figure 3.30(b) are of particular interest as the blockage trend with increased tip clearance changes at rotor exit measurement locations compared to stator exit positions. At the rotor exit conditions, the increase of the tip leakage flow size with increased tip clearance leads to a redistribution of fluid to lower spanwise locations. As a result, the mid-span (and hub, although not shown here) are energized and blade surface separation tendencies decrease, leading to a reduction of blockage associated with the blade wake. This differs from the NL condition, for which the wake thickness and corresponding velocity defect at mid-span are relatively insensitive to the increase of tip clearance. At the stator exit planes at HL, however, the change of stator inlet conditions due to the tip leakage flow and the flow redistribution leads to an increase of wake thickness in the mid-span and near the tip, but a decrease of wake thickness near the hub. These characteristics are also reflected in the mid-span blockage data, Figure 3.30.

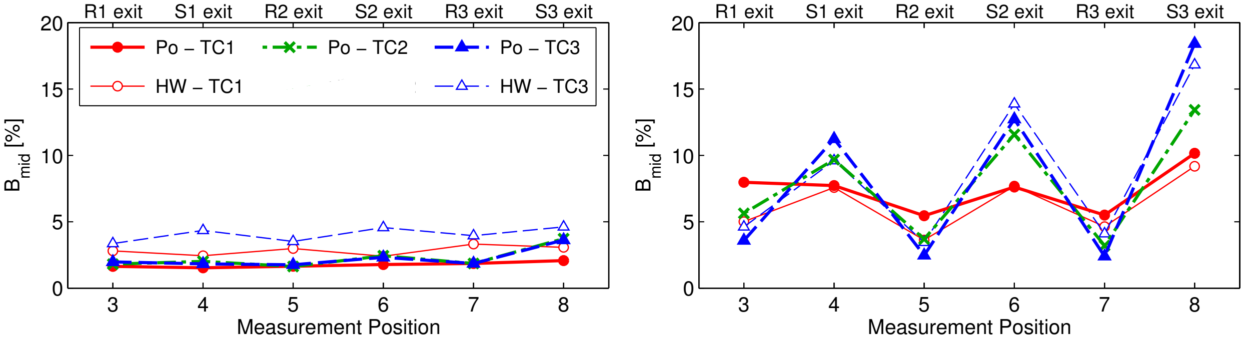

(a) (b)

Figure 3.30: Comparison of true blockage (hot-wire) and approximated blockage (total pressure) in the mid-span region: (a) NL, (b) HL.

Finally, the overall integrated blockage information in Figure 3.31 provides a holistic comparison of these blockage approximation techniques. As before, nominal loading comparisons are shown in Figure 3.31(a) and high loading comparisons are shown in Figure 3.31(b). Although the hub blockage is not shown explicitly here for brevity, the overall results in Figure 3.31 lead to several notable observations: First, the pattern of increased blockage at rotor exits and decreased blockage at stator exit positions identified for the tip region (Figure 3.29) directs the overall blockage for the NL condition in Figure 3.31(a). At the rotor exit plane, the tip leakage flow contributes to large blockage, but that blockage decreases after passing through the stator. This observation is consistent for all three tip clearances based on both the velocity data and the pressure data. However, this trend is not present at HL. At the high loading condition, the significant increase of blockage through the mid-span (Figure 3.30(b)) dictates the change of shape shown in Figure 3.31(b). The results presented here separating the blockage contributions into distinct regions of the annulus provide new insights about how blockage develops through a multistage axial compressor as a result of large rotor tip clearances.

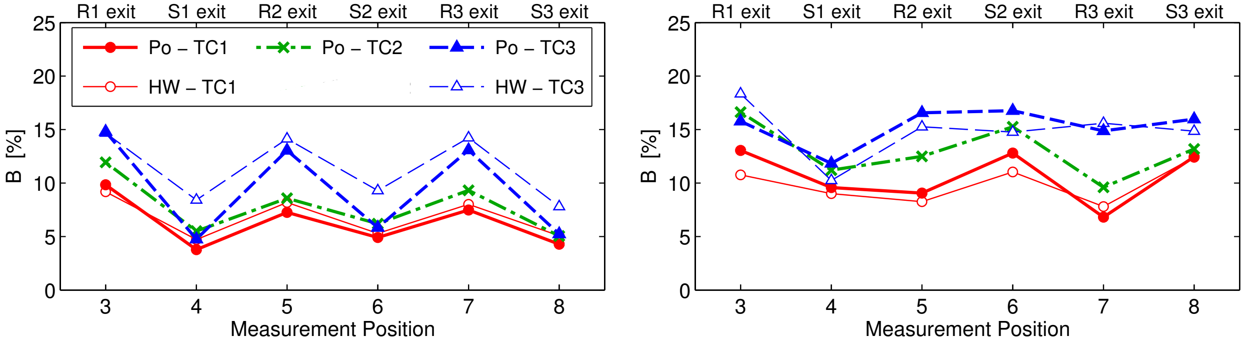

(a) (b)

Figure 3.31: Development of integrated blockage through the compressor combining measurements for all tip clearance configurations: (a) NL, (b) HL.

3.5. Over-Rotor Static Pressures

3.5.1. Influence of Loading Condition on Leakage Flow Trajectory

In previous work, Berdanier and Key (2015b, 2016c) showed the utility of fast-response flush-mounted over-rotor static pressure transducers. Using the definitions for EA and RMS pressures introduced above, an example set of EA and RMS static pressures are shown in Figure 3.32 (a) and (b), respectively.

Yoon et al. (2006) used these RMS pressures to identify the trajectory of the tip leakage flow by tracing the locus of peak unsteadiness positions. A visual comparison of Figure 3.32 (a) and (b) shows that the same leakage flow trajectory is identified by the boundary of the low-pressure trough from the EA static pressures in Figure 3.32(a) and the locus of peak RMS unsteadiness in Figure 3.32(b). Using results similar to Figure 3.32(b) for the other loading conditions, the leakage flow trajectories have been identified for the LL, NL, and HL conditions, as defined by the speedlines in Figure 3.33(a). These trajectories are shown in Figure 3.33(b) (the PE trajectory is not shown due to its relative similarity to NL). For the two high flow rate conditions, NL and LL, Figure 3.33(b) shows that an increase in rotor tip clearance has the effect of moving the leakage flow trajectory closer to the blade suction surface – the same effect as unloading the blade row. The same non-linear leakage flow trajectory noted for Figure 3.32(b) can also be identified at the LL condition.

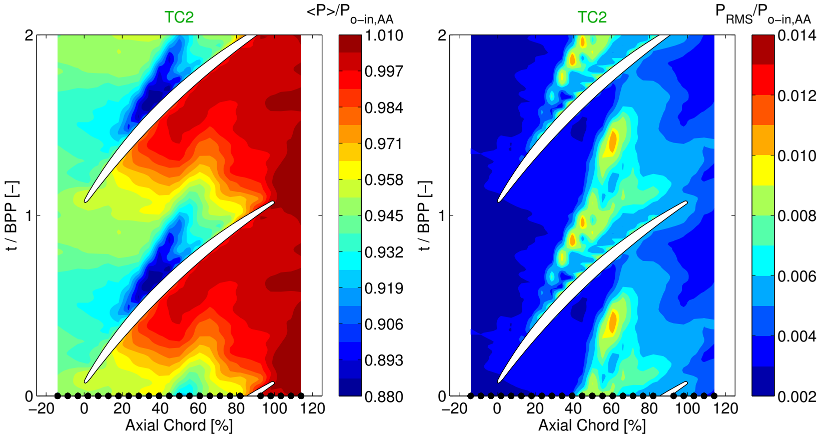

(a) (b)

Figure 3.32: Example over-rotor static pressure results for Rotor 1 with TC2 at NL: (a) EA, (b) RMS.

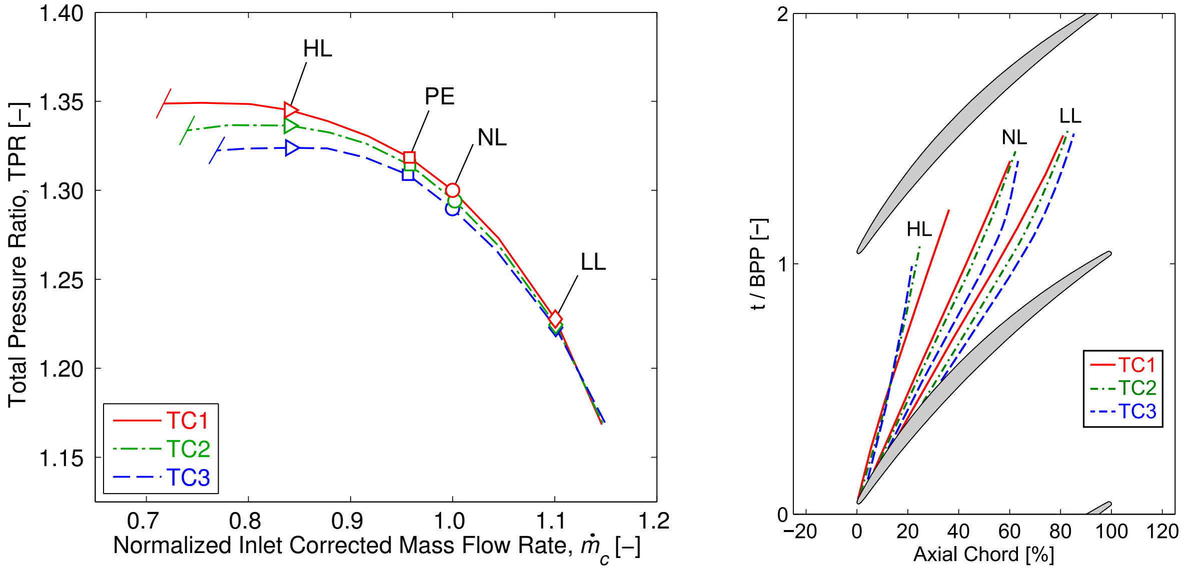

(a) **(b)**

Figure 3.33: Operating condition definition and corresponding leakage flow trajectories for matched corrected mass flow rate (all loading conditions).

As the loading is increased, the position of peak pressure difference across the blade tip moves toward the leading edge, and the location of leakage flow inception moves upstream. Figure 3.33(b) also depicts a noticeable change of the leakage flow trajectory at the high loading condition as the tip clearance increases. Specifically, the two larger clearances, TC2 and TC3, turn more noticeably away from the axial direction and toward the adjacent blade, whereas the TC1 trajectory portrays a more linear path. This observed change in behavior for the HL condition can be attributed to the relative proximity of the HL points to the stall point for each tip clearance, as outlined in Table 3.1 (see also Figure 3.33(a)) recalling the equation for stall margin:

$$\mathrm{SM} = \frac{\left(\frac{\mathrm{TPR}}{\dot{m}_c}\right)_{stall} - \left(\frac{\mathrm{TPR}}{\dot{m}_c}\right)}{\left(\frac{\mathrm{TPR}}{\dot{m}_c}\right)} \times 100\,\% \,. \tag{3.13}$$

Table 3.1: Stall margin calculated for HL condition.

TC Config.	SM [%]
TC1	17.5
TC2	13.3
TC3	9.3

In previous work by Erler et al. (2016), the stall margin is estimated by the position of the interface between the tip leakage flow and the incoming flow. Based on this work, the differences between high loading trajectories shown in Figure 3.33(b) resulting from the difference in stall margin at HL should collapse if the data are instead compared at equivalent stall margin. Thus, data were collected for TC1 and TC2 at an equivalent TC3 stall margin of 9.3%, as shown in Figure 3.34(a), and the corresponding trajectories are compared in Figure 3.34(b). Referring to Figure 3.33(b), however, the PE, NL, and LL operating points identified leakage trajectory angles which decreased with increasing tip clearance. Thus, matching stall margin will not have the desired effect of collapsing the trajectories at these operating conditions.

As an alternative, comparing loading conditions using a ratio of total pressure ratio to corrected mass flow rate, $\mathrm{TPR}/\dot{m}_c$, can be used to approximate equivalent incidence between different configurations. The resulting operating points from this comparison are identified by an asterisk in Figure 3.34(a), PE*, NL*, and LL*. The trajectories resulting from these positions are presented in Figure 3.34(b). These results show that for flow rates greater than or equal to the peak efficiency point, equivalent leakage flow trajectory angles are achieved with different tip clearances when the rotor incidence is matched – e.g., with the ratio $\mathrm{TPR}/\dot{m}_c$. Furthermore, the leakage flow inception position along the blade chord also collapses at these matched conditions, resolving the discrepancies identified in Figure 3.33(b). Although the results presented here for Figure 3.33(b) and Figure 3.34(b) are specific to Rotor 1, the same observations are true for these matched conditions (HL–SM, PE*, NL*, and LL*) with Rotor 2 and Rotor 3, as shown in Figure 3.35.

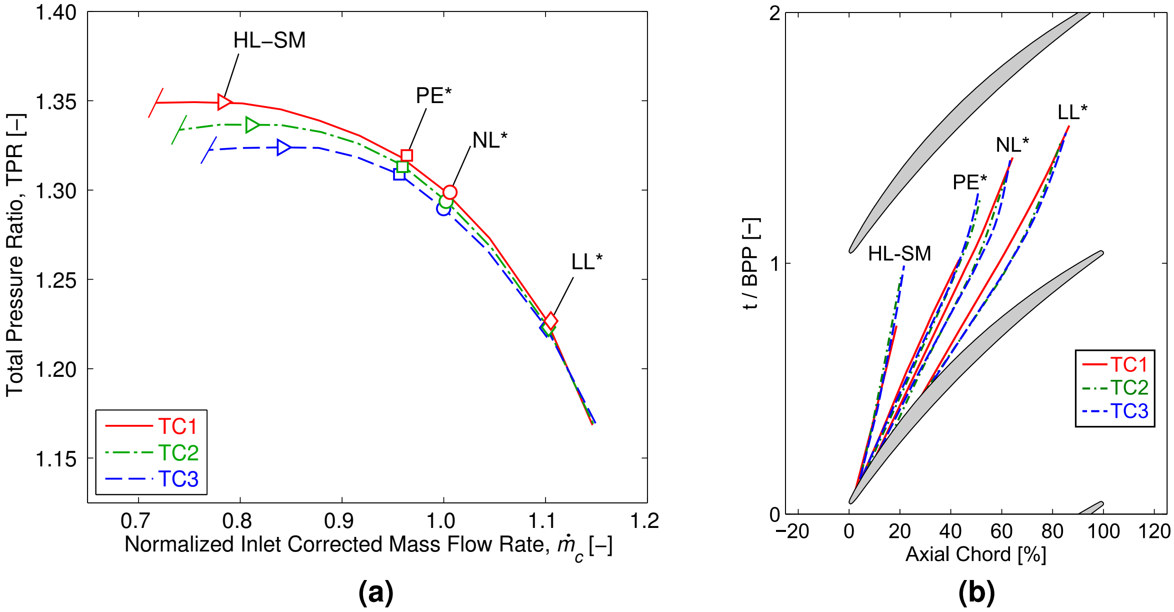

Figure 3.34: Operating condition definition and corresponding leakage flow trajectories for matched stall margin (HL) and matched $\mathrm{TPR}/\dot{m}_c$ (PE, NL, LL).

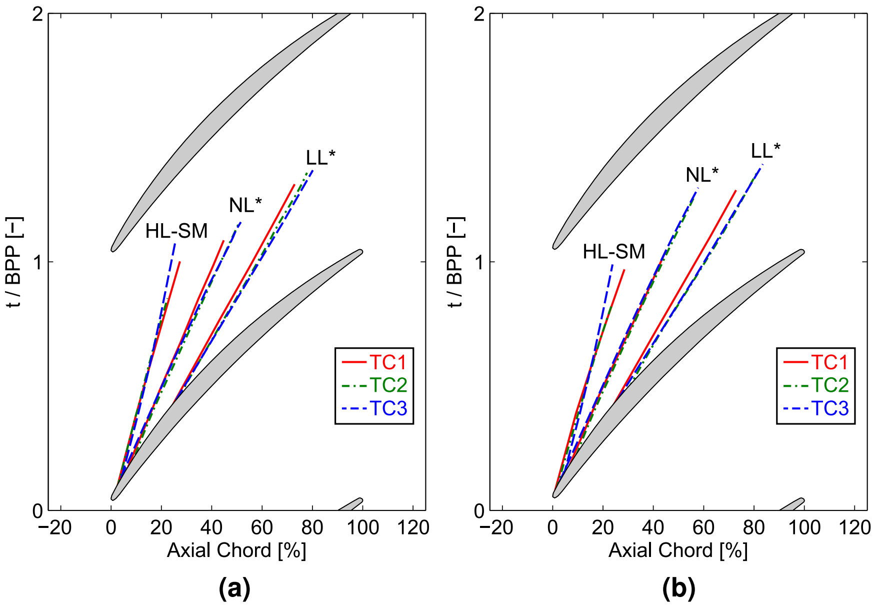

Figure 3.35: Leakage flow trajectories for matched stall margin (HL) and matched TPR/$\dot{m}_c$ (NL, LL): (a) Rotor 2, (b) Rotor 3.

3.5.2. Influence of Stator Wakes on Leakage Flow Trajectory

Berdanier and Key (2015b) previously addressed the observation that adjacent stator vanes may affect the development of the tip leakage flow in the blade passage. Specifically, as the rotor (e.g., Rotor 2) passes through the wake from the upstream stator vane (e.g., Stator 1), a temporary change in loading is sensed as a result of the absolute velocity deficit in the wake, and this change in loading may influence the development of the tip leakage flow. Additionally, the propagation of the low-momentum wake fluid through the rotor passage is likely to continue interacting with the tip leakage flow and affect both its trajectory across the passage and radial movement within the passage.

To better understand this relationship, the same over-rotor static pressure measurements were repeated for several loading conditions with the baseline tip clearance, TC1. A cartoon schematic, Figure 3.36, outlines this measurement process. The sensors are in fixed positions in the compressor casing, but the upstream and downstream stator vanes can be moved (either simultaneously or independently) through the use of a series of linear actuators. Thus, Figure 3.36 shows representative measurements that may be collected at two vane positions with respect to the fixed measurement locations: (a) sensors are circumferentially located at mid-passage with respect to the trailing edge of the upstream stator, or (b) the sensors are circumferentially located in line with the upstream stator trailing edge.

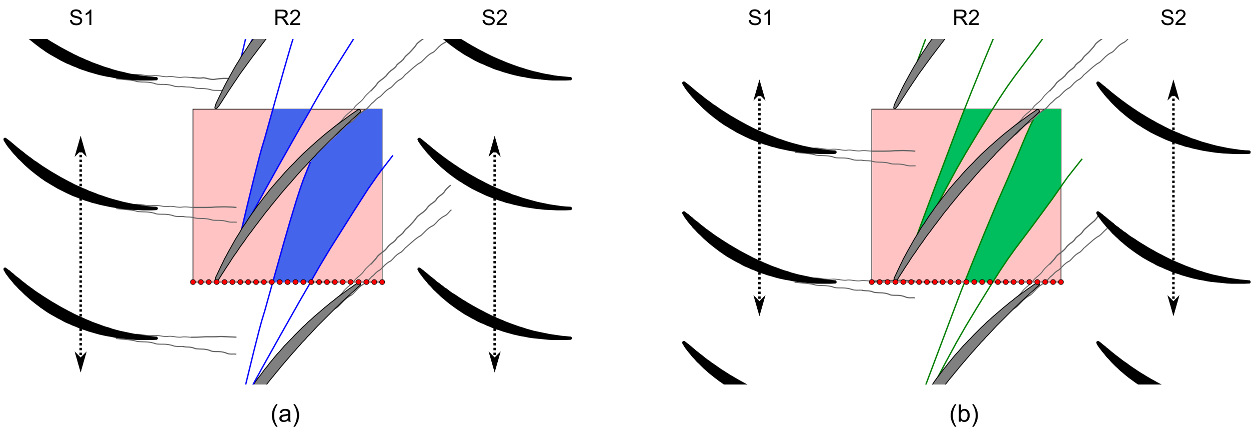

Figure 3.36: Schematic of leakage flow measurements over the rotor for two vane wake-leakage flow interaction positions, (a) and (b).

In each case, the time-resolved measurements are phase-locked with the rotor rotation, so the shaded measurement region identifies one rotor blade pass period of data. The cartoons in Figure 3.36 show measurements over Rotor 2 for which the upstream and downstream stator vanes were moved together, but data were also collected over Rotor 2 when Stator 1 and Stator 2 (the upstream and downstream vane rows) were moved independently from one another.

To assess this effect, the IGV and Stator 1 were moved to 25 unique equally-spaced pitchwise positions with respect to the fixed pressure sensors over Rotor 2. A smooth modulation of static pressures over Rotor 2 can be identified by moving cyclically through the 25 pitchwise positions, but only two out-of-phase positions are shown here for comparison, identified in Figure 3.37 as 0% vp and 52% vp. These measured data represent the sensor positions (a) and (b) identified in Figure 3.36, respectively. For these results in Figure 3.37, the vanes downstream of Rotor 2 (Stator 2 and Stator 3) were maintained in fixed positions to separate effects due to the upstream stator wake from the potential field associated with the downstream vanes.

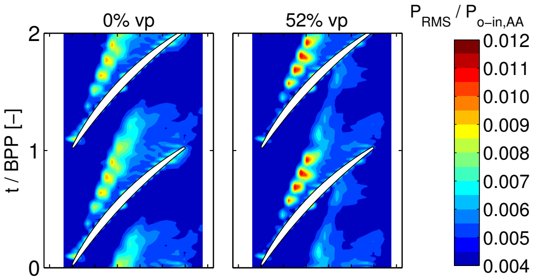

Figure 3.37: Rotor 2 static pressure unsteadiness for two Stator 1 positions half a passage out-of-phase from one another.

The pressure RMS unsteadiness results for these two discrete vane positions shown in Figure 3.37 have been used to determine the leakage flow trajectories, as explained in the discussion accompanying Figure 3.33(b). This comparison of trajectories, Figure 3.38(a), shows an identifiable difference of nearly three degrees between 0% vp and 52% vp. Although this difference may seem small, it is significant compared to the effects associated with changes of tip clearance or loading condition, as will be shown later in this paper.

A procedure similar to the one outlined for Figure 3.37 was followed to identify whether the potential field associated with the downstream vanes may also affect the trajectory of the tip leakage flow. In this case, the IGV and Stator 1 were maintained in fixed positions while Stator 2 and Stator 3 were moved simultaneously to 25 pitchwise positions. The time-averaged static pressure downstream of the Rotor 2 trailing edge was used to identify the vane positions associated with the minimum and maximum static pressure field related to Stator 2. The leakage flow trajectories from these vane positions are presented in Figure 3.38(b). These results confirm that there is no discernable effect on the trajectory of the tip leakage flow associated with the downstream potential field compared to the effect from the upstream vane wakes. The same conclusion can be made regarding the results at the high loading condition, although not shown here. Thus, previous authors have identified a stator-rotor interaction governing the development of the rotor tip leakage flow, but these measurements help to specifically discern between upstream and downstream vane effects.

The interaction between the tip leakage flow and the downstream potential field may depend on the geometry of the compressor. In particular, the axial spacing between the adjacent blade rows will determine the extent to which the potential field interacts with the TLF. The exponential decay of the potential field as it propagates upstream governs that its influence will approach zero at one stator pitch distance upstream of the stator leading edge. For the present compressor, one stator pitch upstream of the vane leading edge corresponds to roughly mid-chord within the rotor passage. For Rotor 1, Rotor 2, and Rotor 3, the exact positions are 48%, 49%, and 61% axial chord, respectively. Based on this, although the tip leakage trajectories are clearly identified beyond 60% axial chord for the NL condition (e.g., Figure 3.37), the trajectories are still unaffected by the decaying potential field.

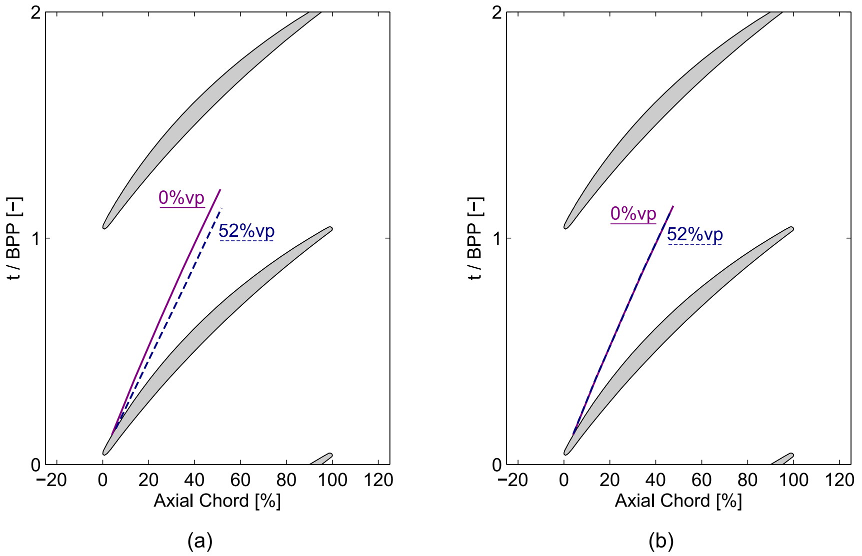

Figure 3.38: Rotor 2 leakage flow trajectories: (a) Stator 1 pitchwise positions 0%vp and 52%vp identified in Figure 3.37; (b) Stator 2 positions for Stator 2 and Stator 3 movement (with IGV and Stator 1 fixed).

3.5.3. Blade-to-Blade Leakage Flow Variability

In general, compressor measurements associated with the rotor are often considered in an average form, neglecting variations which may exist from one blade to the next – similar to the results presented in Figure 3.32. However, small manufacturing defects in the blade hardware and blade row interactions within the machine can create substantial variations which must be considered, as identified in rotor wake variability studies by previous authors (Smith et al., 2016; Sherman et al., 1996; Boyd and Fleeter, 2003; Key et al., 2010) Thus, it is also desirable to assess blade-to-blade variations of the tip leakage flow and a contextual comparison with respect to the influence of upstream stator wakes identified in the previous section.

As explained in Chapter 2, the runout of the rotor blade tips has been evaluated using a dial indicator with a rolling tip. These measurements, recast in Figure 3.39, represent the blade-to-blade variation of static (non-operating) tip clearance height at any fixed location about the circumference of the compressor. The information in Figure 3.39 shows that the blade-to-blade tip clearance varies on the order of 3×10^{-3} to 5×10^{-3} in. (depending on rotor row) around the circumference of the rotor. However, there is also a particularly large discrepancy for Blade 9 of Rotor 3, which shows a significant increase of tip clearance of approximately 1×10^{-3} in. compared to its adjacent blades.

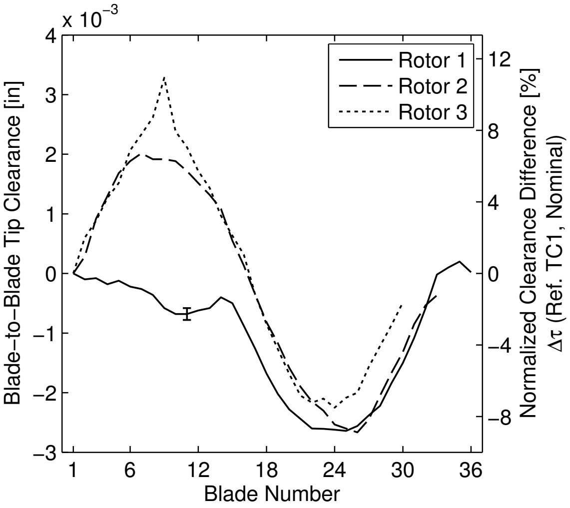

Figure 3.39: Blade-to-blade variation of rotor tip clearance with respect to Blade 1 for each rotor row.

Based on the information in Figure 3.39, it is expected that a discernable change of tip leakage flow pattern may be identified for Blade 9 of Rotor 3. Indeed, if the RMS results for Rotor 3 are maintained as 30 separate data sets (one for each blade) instead of an average blade pass period representing the entire row, Figure 3.40 shows that Blade 9 can be easily identified by its leakage flow pattern which differs noticeably from its adjacent blades. In this case, the local tip clearance increase for Blade 9 creates a larger region of high unsteadiness identified by the RMS which is more dispersed throughout the blade passage, compared with the more localized trajectories crossing the blade passage for the other blades. Moreover, the clearances for Blade 8 and Blade 10 in Fig. 10 are nearly identical. However, the change of the tip leakage flow for the increased clearance of Blade 9 locally affects the loading of the adjacent blade, Blade 10, causing the leakage flow of Blade 10 to behave differently than Blade 8, despite their similar clearance values.

To compare the blade-to-blade variations of tip leakage flow unsteadiness with the vane wake modulation presented above, RMS signatures from the sensor at 50% axial chord are shown in Figure 3.41. Figure 3.41(a) shows the blade-to-blade variability of the RMS unsteadiness for each of the 30 blade pass periods corresponding to the data in Figure 3.40, and a representative average blade pass period is also identified by the arithmetic mean of the signals from the individual blades. Similarly, Figure 3.41(b) shows the modulation effect of the RMS unsteadiness due to the upstream vane wake for the same condition. In Figure 3.41, the peaks centered around $t/\mathrm{BPP} = 0.2$ represent the blade passing event, and the rise of unsteadiness in the range of $t/\mathrm{BPP} = 0.4 - 0.8$ represents the tip leakage flow. Based on the results in Figure 3.41, the minimum-to-maximum blade-to-blade variability of RMS unsteadiness in the tip leakage flow, Figure 3.41(a), is of similar magnitude to the modulation due to vane positions, Figure 3.41(b). However, a majority of the blade-to-blade traces in Figure 3.41(a) align with the average, such that only a few outliers are present. On the other hand, the vane wake modulation in Figure 3.41(b) is more evenly balanced around the average.

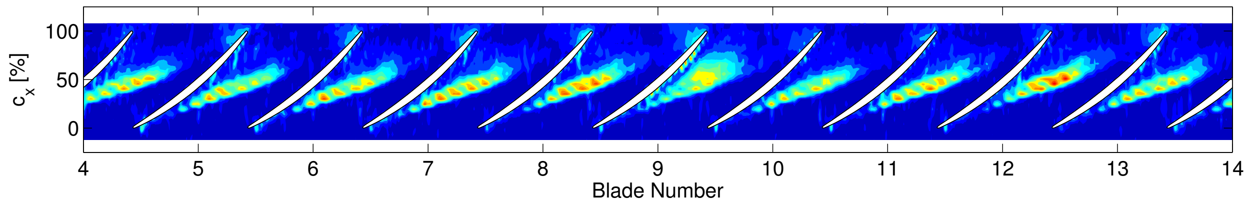

Figure 3.40: Blade-to-blade leakage flow pattern variability for Rotor 3 with TC1 at NL.

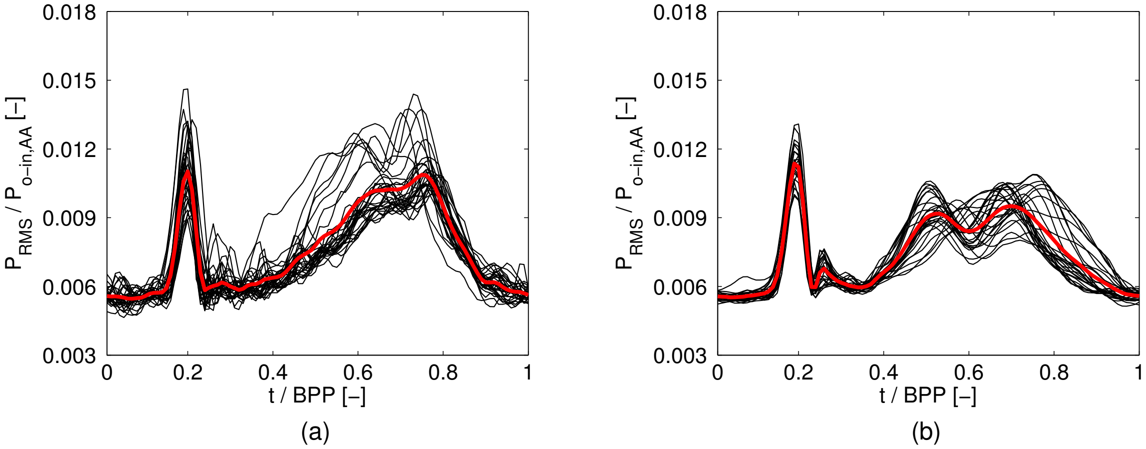

Figure 3.41: Comparison of RMS signatures at 50% axial chord for Rotor 3 with TC1 at NL: (a) 30 individual blade pass periods at one vane position, (b) Average blade pass period for 25 unique vane positions across one stator pitch.

Aside from the differences for Blade 9 identified in Figure 3.40, blade-to-blade variations of the TLF are also visible for other blades which do not necessarily correlate with the clearance variations in Figure 3.39. Figure 3.42 shows a similar comparison of blade-to-blade leakage flow variability, but for all 30 blades from the Rotor 3 row at the larger tip clearance TC3. In Figure 3.42, the 30 blades have been segmented into three 10-blade series.

For this facility, the difference of blade counts between Rotor 1, Rotor 2, and Rotor 3 (36, 33, and 30, respectively) introduces a 3/rev modulation of the flow field for both Rotor 2 and Rotor 3. Figure 3.42 highlights the effect of this 3/rev modulation on the tip leakage flow. An assessment of the EA static pressure signals (not shown) highlights troughs of this 3/rev modulation which exist at blade numbers of approximately 3, 13, and 23, and peaks located at blade numbers of 8, 18, and 28. The data in Figure 3.42 identify these same trends as the 3/rev troughs at Blades 3, 13, and 23 show lower leakage flow intensities than the peaks at Blades 8, 18, and 28.

However, the results in Figure 3.42 tell an additional story as the 3/rev modulation is superimposed with the 1/rev tip clearance variations identified for Rotor 3 in Figure 3.39. A specific comparison of the TLF pattern for Blades 3, 13, and 23 (the troughs of the 3/rev modulation) shows highest intensity in the leakage flow for Blade 23 and lowest intensity (with more dispersed unsteadiness) for Blade 3.

Based on the data shown in Figure 3.40 and Figure 3.42, it is determined that the effect of small blade-to-blade tip clearance variations, such as the one identified for Blade 9 from Rotor 3, are most noticeable in the leakage flow unsteadiness if the tip clearance height is small (i.e., TC1 instead of TC3). This observation could be due to the fact that a 1×10^{-3} in. change represents a larger fraction of the overall clearance height for TC1 (nominally 0.030 in.) than for TC3 (nominally 0.080 in.), but the closer proximity of the sensors to the blade tips for TC1 may also make the sensors more sensitive to these small variations.

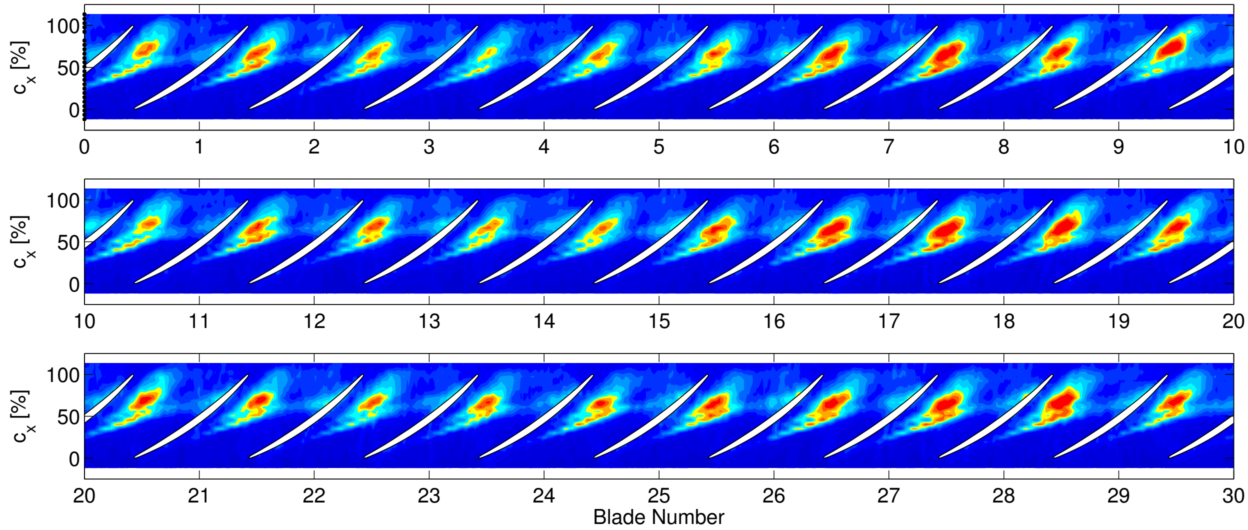

Figure 3.42: Blade-to-blade leakage flow pattern variability for Rotor 3 with TC3 at NL.

Similar to the stator wake interaction highlighted in Figure 3.38, the blade-to-blade variations identified in Figure 3.40 and Figure 3.42 are also important for quantifying changes of the tip leakage flow angle. In this case, the leakage flow angle, ξ, is defined with reference to an axial reference datum, as shown in Figure 3.43. In this figure, two leakage flow trajectories are shown for each rotor at two loading conditions, NL and HL. The minimum and maximum traces define the envelope of trajectory angles representing the blade-to-blade variations. This angular envelope for Rotor 1 is 1.8 degrees for both NL and HL. The blade-to-blade variation of trajectory angle shows no discernible trend with the tip clearance height (e.g., Figure 3.39), and no rotor-rotor interactions are expected for the Rotor 1 results.

However, several differences exist for the Rotor 3 results in Figure 3.43 compared to Rotor 1. In particular, the envelope of blade-to-blade trajectory angle variation for Rotor 3 is 1.5 degrees for NL, but increases to 2.2 degrees for HL. Also, the axial location of leakage flow inception and the leakage flow trajectory angle are more similar between the NL and HL positions for Rotor 2 than for Rotor 1. In this case, although a weak trend of trajectory angle with blade-to-blade tip clearance variation exists, there is no discernible trend associated with the other engine-order frequencies introduced previously. The Rotor 3 envelopes are nearly identical to the Rotor 2 trends (1.5 and 2.2 degrees for NL and HL respectively). For comparison, these blade-to-blade differences of tip leakage trajectory angle with a fixed position of the adjacent stator vanes are consistently on the order of 75% of the average modulation introduced by the upstream stator wakes.

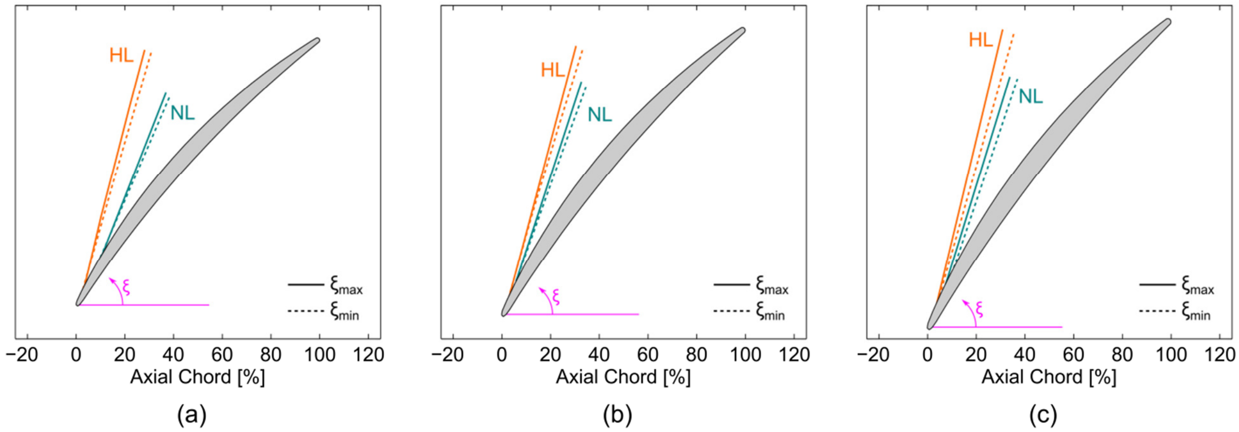

Figure 3.43: Maximum and minimum leakage flow angle variations for TC1:
(a) Rotor 1, (b) Rotor 2, (c) Rotor 3.

3.5.4. Quantifying Tip Leakage Flow Trajectory

Using the leakage flow trajectory identification techniques presented in this paper, the angle of the leakage flow trajectory can be determined. The results from the present study are shown for each of the three rotors at the four loading conditions in Figure 3.44. Several of the NL and HL data points for TC1 in Figure 3.44 also include range bars which identify the variations of tip leakage trajectory angle associated with the modulation of the TLF due to the upstream vane wakes (as calculated using information similar to Figure 3.37). The data in Figure 3.44 are presented as a function of measured tip clearances instead of the "nominal" design values. These operating clearances account for thermal growth differences related to changes in loading and ambient temperature discussed by Berdanier and Key (2015a).

The results in Figure 3.44 highlight several trends. In particular, the leakage flow trajectory angles change differently for Rotor 1 than for Rotor 2 and Rotor 3, both of which show similar trends at all four loading conditions. For all rotors, however, there is a consistent trend of decreasing trajectory angle with increasing tip clearance for LL, NL, and PE, but an increasing trend for the HL condition. At the HL condition, the relative difference of stall margin between the three clearance configurations has a more profound effect on the flow.

The results for Rotor 1 in Figure 3.44 show that the leakage trajectory angles vary almost linearly with increasing rotor tip clearance for the range of clearances investigated in the present study. This result is in alignment with the model introduced by Chen (1991) in comparison with experimental data from single-stage machines and isolated rotor tests. In contrast to these Rotor 1 observations, the data for Rotor 2 and Rotor 3 show insignificant changes of leakage flow trajectory angle for a tip clearance change from TC1 to TC2. This noted difference for Rotor 2 and Rotor 3 is crucial to this study because it shows a trend which would be otherwise overlooked if only two tip clearances were studied (e.g., TC1 and TC3, as was the case for the data presented by Yoon et al. (2006)). Furthermore, this result suggests additional multistage effects on the tip leakage flow trajectory which may be overlooked in the model from Chen. This difference of leakage flow trajectory angles between Rotor 1 and the other two rotor rows agrees with previous observations in this facility suggesting a difference of Rotor 1 performance with increased tip clearance compared to the downstream rotors.

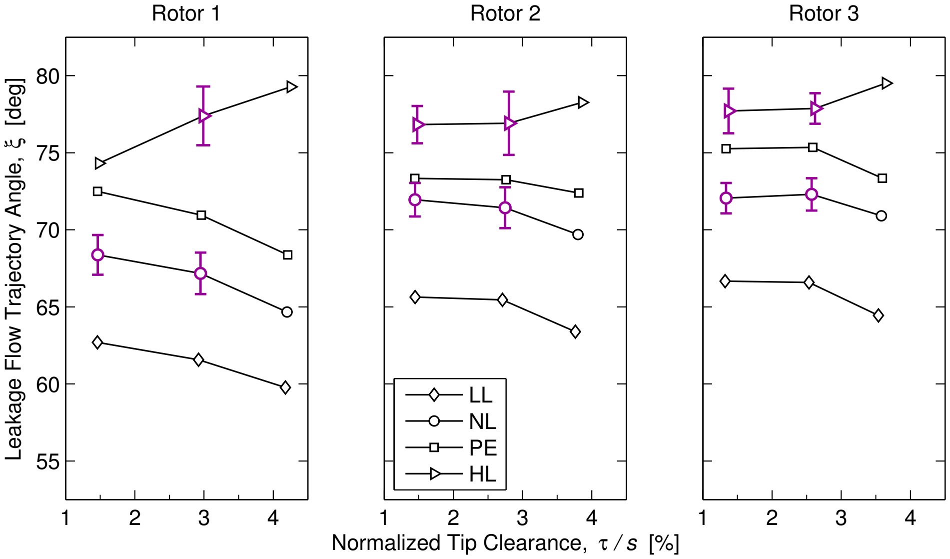

Figure 3.44: Leakage flow trajectory angle versus normalized clearance height. Range bars identify change of trajectory angle due to interaction with the upstream vane wake.

Results similar to the measurements presented in Figure 3.44 have also been collected by Yoon et al. (2006) over Rotor 3 in a four-stage low-speed research compressor with repeating stages. A comparison of the Rotor 3 results from the present study with the measurements collected by Yoon et al. is shown in Figure 3.45.

Previous authors have introduced the clearance derivative as a method for evaluating the change of a particular parameter with changes in tip clearance. In this case, a clearance derivative for leakage flow trajectory angle is defined with respect to the clearance-to-pitch ratio:

$$\delta_\xi = \frac{\Delta\xi}{\Delta(\tau/s)}. \tag{3.14}$$

In Figure 3.44 and Figure 3.45, the clearance-to-pitch ratio was selected instead of the clearance-to-chord ratio used by Yoon et al. (2006) (or clearance-to-span, which is typically used as a metric for efficiency changes) to present trajectory angle changes. The clearance-to-pitch ratio was also chosen to avoid discrepancies of aspect ratio between the two facilities compared in Figure 3.45. A comparison between the four-stage low-speed compressor used by Yoon et al. with the machine used for the present study shows a difference of aspect ratio from approximately 1.2 to approximately 0.7, respectively.

The relationship between pitch and blade loading, as well as the contribution of pitch as a representative length scale in the measurement plane over the rotor, combined to guide the selection of clearance-to-pitch as the representative metric for comparison. However, the relative dissimilarity of blade pitch for Yoon et al. (2006) and the present study creates an opportunity to evaluate the dependence of observed trends to a particular compressor design. Furthermore, the rotor blade sections differ between the current study (DCA) and the Yoon et al. study (GE E^3).

A comparison of the results from the present study in Figure 3.45 with the data presented by Yoon et al. (2006) shows good agreement using the clearance-to-pitch ratio on the abscissa. Especially at the LL and HL conditions, the clearance derivatives are nearly identical when the widest tip clearance range is considered for the present study (TC1 to TC3). However, the absence of a third tip clearance configuration for Yoon et al. makes it difficult to conclude whether the same non-linear trend is expected for all multistage compressors. For reference, if the Rotor 2 results from the present are selected for comparison with Yoon et al. instead of Rotor 3, the results are also similar based on the nearly identical trends between Rotor 2 and Rotor 3 in Figure 3.44.

In general, the position of leakage flow inception may be subject to the loading distribution. For the compressor analyzed in this study, the tip sections of the DCA rotors are loaded such that the maximum pressure difference occurs near 35% c_x for LL, approximately 30% c_x for NL and PE, and 20% c_x for HL. However, Chen (1991) showed that the leakage flow trajectory is governed by the blade parameters, not the loading distribution. Although the different blade profiles for the present study and Yoon et al. (2006) yield leakage trajectory angles which differ in magnitude, the trend of trajectory angle with clearance is the same. As a rule-of-thumb, these data suggest that the leakage flow trajectory angle will decrease approximately one degree for every one percent increase of clearance-to-pitch when rotor incidence angle is large and negative. Similarly, approximately one degree of trajectory angle increase is expected for every one percent of clearance-to-pitch when rotor incidence is large and positive.

Although these data show trends which may apply for large clearance changes, it is important to observe that a critical clearance may exist, leading to significant differences of the clearance derivative for leakage flow angle assessed here. For the present study, the critical clearance represents the TC2 clearance height. By this proposed effect, a change from a "small" to a "moderate" clearance height (i.e., TC1 to TC2) may be met by little or no change of leakage flow angle, whereas a change from a "moderate" to "large" clearance height (i.e., TC2 to TC3) may incur significant changes.

Further comparison of the present study results in Figure 3.45 with the data from Yoon et al. (2006) also shows that the peak efficiency point from the comparison study has a positive clearance derivative which was not observed in the present study. Despite this difference, the observed trends at LL and HL are similar between two machines with different blading parameters – the primary influencing component according to Chen (1991).

The range bars in Figure 3.45 show that the leakage flow modulation associated with the upstream vane wake has a profound influence on the leakage flow. In fact, the change of leakage flow angle due to this stator-rotor interaction is greater than the change due to a doubling of the tip clearance height (TC1 to TC2). At this point, however, there is sufficient information to determine that the stator-rotor interaction plays a significant role in the development of the tip leakage flow, and this relationship must be appropriately considered when comparing experimental data with computational results.

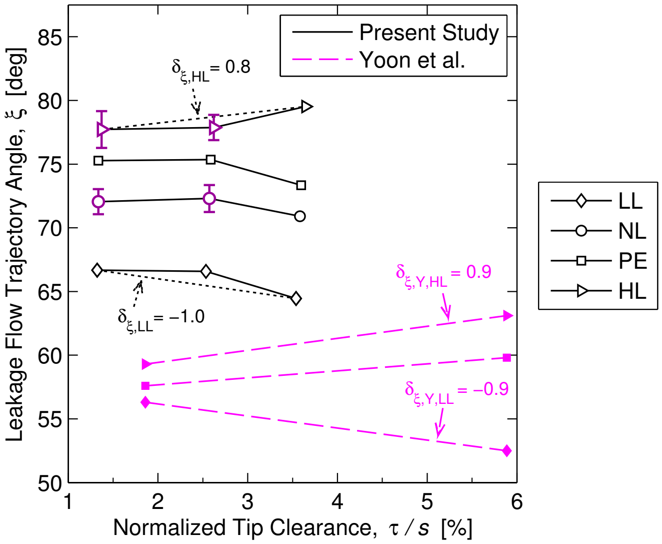

Figure 3.45: Rotor 3 leakage flow trajectory trends compared with results from Yoon et al. (2006).

Further comparison of the present study results in Figure 3.45 with the data from Yoon et al. (2006) also shows that the peak efficiency point from the comparison study has a positive clearance derivative which was not observed in the present study. Despite this difference, the observed trends at LL and HL are similar between two machines with different blading parameters – the primary influencing component according to Chen (1991).

The range bars in Figure 3.45 show that the leakage flow modulation associated with the upstream vane wake has a profound influence on the leakage flow. In fact, the change of leakage flow angle due to this stator-rotor interaction is greater than the change due to a doubling of the tip clearance height (TC1 to TC2). At this point, however, there is sufficient information to determine that the stator-rotor interaction plays a significant role in the development of the tip leakage flow, and this relationship must be appropriately considered when comparing experimental data with computational results.

3.6. Stator Hub Seal Leakage Flow

3.6.1. Time-Averaged Results

Berdanier and Key (2015b) previously presented Stator 3 seal flow rate measurements accompanying a series of detailed compressor map data for this compressor facility. To further develop this data set, stator hub shroud cavity pressure measurements were simultaneously collected for both Stator 1 and Stator 2 for TC1. The compressor map points outlined by Berdanier and Key (see Figure 2.2) were matched to provide additional boundary conditions for those available data sets. However, additional points were also measured in between these pre-defined operating points to yield a high-resolution speedline for each of the four operating speeds. Because the measurements were collected from high-frequency response pressure transducers, time-resolved data are available, but the time-averaged results are considered here first in Figure 3.46.

In Figure 3.46, the differential pressure across the knife seals is shown separately for Stator 1 and Stator 2 at the four identified corrected speeds (100%, 90%, 80%, and 68%). The instrumentation design for these measurements accommodated sensor positions at two discrete locations around the compressor circumference. These measurement locations were located seven degrees from the horizontal center of the compressor, as shown in Figure 3.47. Thus, for each stator and each speed in Figure 3.46, two curves are presented: one for Half (a) and another for Half (b). For each of these curves, markers identify the pre-defined compressor map points discussed above. Furthermore, measurements for each of these curves were repeated on several days, and a representative range bar is shown on the curves denoting test-to-test variability of these results.

From Figure 3.46, it can be seen that the trend of differential pressure, Δp, across the flow range is noticeably different for Stator 1 versus Stator 2. In particular, all four speeds for Stator 1 show a rise of differential pressure as loading increases, followed by a flat portion of the curve, and then a decrease at low flow rates approaching stall. This trend is consistent between Half (a) and Half (b), although the relative magnitude of Δp decreases for Half (b), such that a greater discrepancy between the two halves of the compressor is observed at 100% N_C than for 68% N_c.

On the other hand, the Stator 2 results in Figure 3.46 show a steady rise of Δp as loading increases (flow rate decreases) until a peak Δp is reached near the HL point (specifically for the 100% speedline). As flow rates decrease further, the differential pressure drops slightly, and then begins to rise again prior to stall. In particular for measurements collected in Half (a) of the compressor, a second drop of Δp is observed immediately before stall at 100% and 90% N_c.

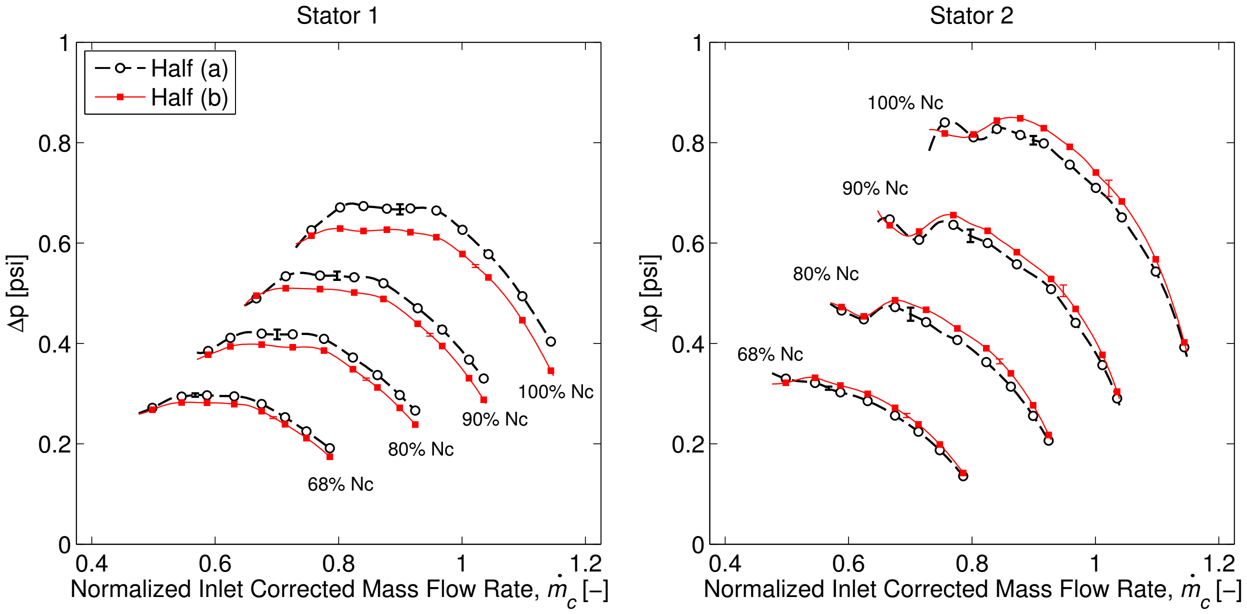

Figure 3.46: Pressure drop across Stator 1 and Stator 2 knife seals at four speeds for TC1. Markers identify map points in Figure 3.1.

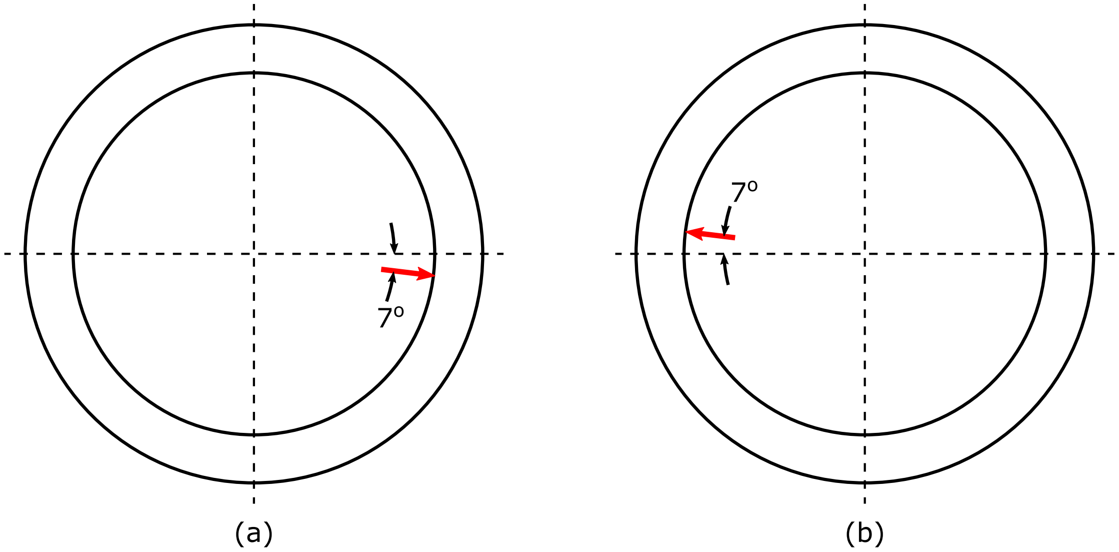

Figure 3.47: Sensor measurement positions for Half (a) and Half (b) noted in Figure 3.46. View is forward looking aft (FLA).

Based on the differential pressure measurements presented in Figure 3.46, a comparison is desired with the static pressure difference across the stator vane. For the compressor map data available from Berdanier and Key (2015b), static pressure in the primary flowpath was measured using static pressure taps located at the outer diameter of the flow annulus. Under a parallel streamline assumption, the static pressure across the span is constant. Thus, the static pressure at the inner diameter of the flowpath (essentially the inlet and exit of the shroud cavity leakage flow) can be defined by these casing-measured static pressures. The differential pressures from these static pressure taps are presented in Figure 3.48. In this figure, Stator 1 and Stator 2 data are shown in parts (a) and (b), respectively, and a schematic of the static pressure measurement locations is shown in part (c).

An initial observation for these comparison Δp data is that the magnitudes are lower than for the knife seal Δp data in Figure 3.46. It is expected that this difference of magnitudes is associated with the decreased flow area and increased flow velocity across the seal teeth. However, the general shape of the curves in Figure 3.48 generally mirrors the shapes identified in Figure 3.46. Specifically, the rise, flat-top, and then drop for Stator 1 moving from high flow rates toward lower flow rates is mirrored in the casing static pressure data. Further, the steady rise of Δp for Stator 2 as loading is increased is also present, and a similar peak is identified near the HL point of 100% N_c. As loading is increased further past HL, the Δp for Stator 2 in Figure 3.48 drops as with the cavity pressures, and the curve appears to begin to level off for the last full traverse point (recalling here that the data point identifying the lowest flow rate in Figure 3.48 does not represent the stall point, but a safe operating point near stall). However, the NS point in Figure 3.46 above showed a distinct increase from the adjacent trough in the curve.

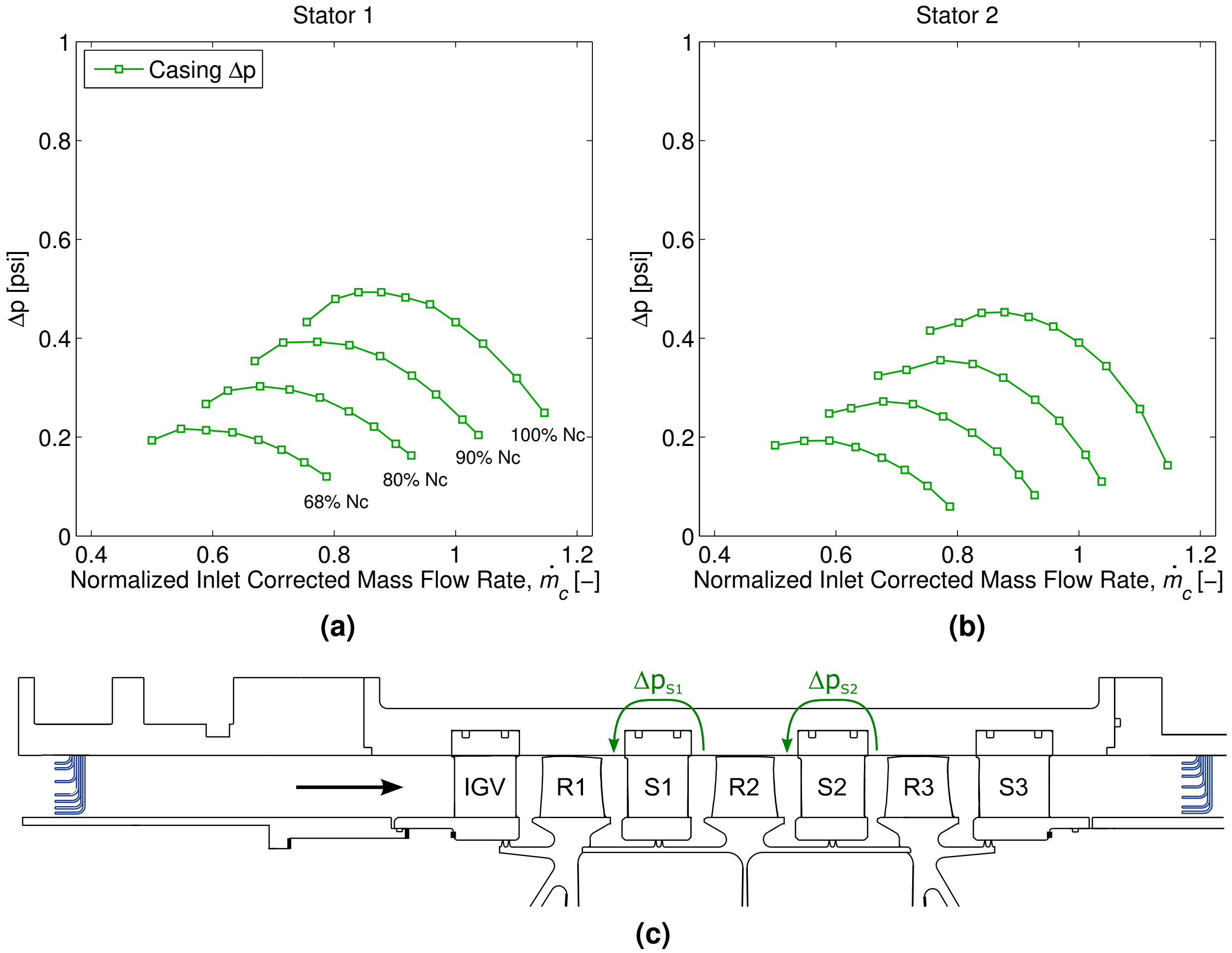

(a)

(b)

(c)

Figure 3.48: Casing pressure drop for map points noted in Figure 3.46: (a) Stator 1, (b) Stator 2, (c) Schematic of measurement positions.

Ultimately, these cavity pressure measurements provide valuable information which can be used for boundary conditions when modeling the shroud cavities in this three-stage compressor. Future analysis of these results, in combination with the three-component velocities and pressure data at the inlet and exit of the shroud cavities may provide additional insight along the same lines as Wellborn (1996). The shape of the Stator 2 curves near stall in Figure 3.46 is of particular interest, and it is possible that these data may be influenced by the large hub corner separation which develops for Stator 2 at high loading conditions. This hypothesis may be tested further by collecting similar Δp measurements with TC2 and TC3 configurations, which alleviate the corner separation at the hub of Stator 2, as shown above in Figure 3.5 and Figure 3.9.

3.6.2. Considerations for Calculating Mass Flow Rate

Wellborn (1996) outlines an equation for calculating mass flow rate through a knife seal using differential pressure measurements across the seal teeth, as derived by a linear momentum balance applied to a control volume surrounding the seal teeth:

$$\frac{\dot{m}_L}{\dot{m}} = C_D\left(\frac{A_\epsilon/A}{\sqrt{1-(A_\epsilon/A_1)^2}}\right)\frac{\sqrt{C_{p1}-C_{p2}}}{\phi}. \tag{3.15}$$

In this equation, the leakage flow rate, $\dot{m}_L$, is a function of the area above the seal tooth, A_ϵ, the area of the flow in the cavity adjacent to the seal tooth (i.e., where the sensors are located), A_1, the throughflow area, A, pressure coefficients defined by the two measured pressures, C_p, and the flow coefficient, ϕ. Because Wellborn developed this equation for application to a series of low-speed compressor tests, it contains several simplifications and assumptions. Of note, this equation contains a constant density assumption which may not be applicable for the present compressor.

Perhaps more important, however, Equation (3.15) relies on a discharge coefficient, C_D, which is crucial for calculating flow rate through an orifice such as the knife seal flow analyzed here. Wellborn (1996) proposes a linearized logarithmic relationship for C_D as a function of the seal tooth width and the seal tooth clearance based on a representative seal tooth geometry from the results of Mahler (1972). In this study, Mahler shows extensively how seal tooth geometry can considerably influence the discharge coefficient (Figure 3.49), and similar results show a significant influence by Reynolds number and other governing parameters.

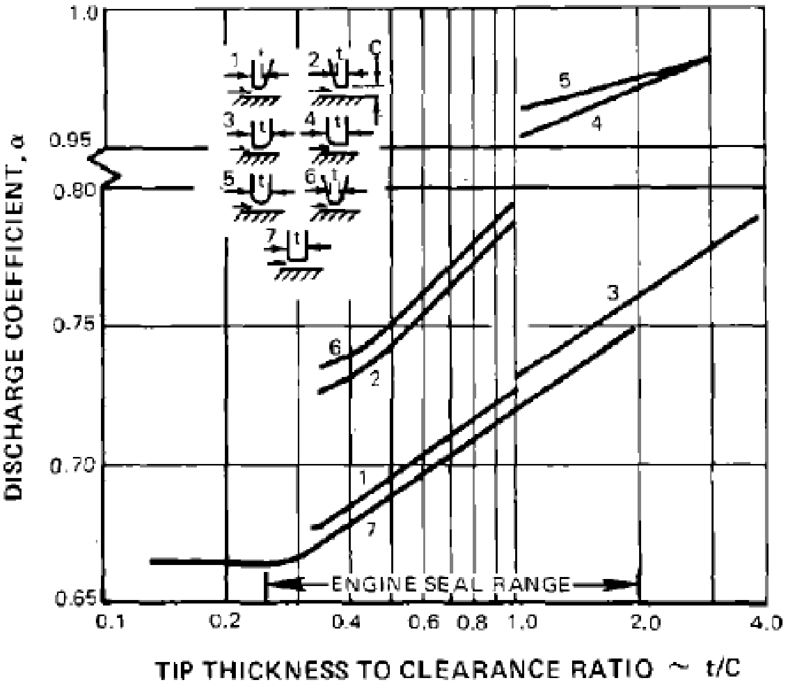

Figure 3.49: Discharge coefficient for different seal tooth geometries (Mahler, 1972).

Based on the relationships outlined by Mahler (1972), and specifically the data shown here in Figure 3.49, the value of C_D may easily range from as low as 0.6 to nearly 1.0, and the geometrical changes required to cause this influence may be small. For instance, unknown seal tooth cross-section profiles (i.e., due to manufacturing errors), a burr or rolled edge left from machining or part mishandling, and even seal tooth geometry changes due to a rub of the teeth with the stator hub shroud (in the event that abradable material is not present), all leave a significant unknown on the C_D necessary to calculate a flow rate from measured differential pressures. Despite this fact, the geometry definition of the seals for this project follows Series 6 in Figure 3.49, and a tooth thickness of 0.020 in. yields a thickness-to-clearance ratio of approximately 0.55 (based on the measured seal clearances outlined in Chapter 2). As a result, a best estimate of C_D for this application is approximately 0.75.

3.6.3. Time-Resolved Results

A considerable added benefit of using high-frequency response pressure transducers to measure the shrouded stator seal cavity pressures is the opportunity to analyze time-resolved data. To begin, pressure data from each of the four sensors were ensemble averaged, and the RMS was also quantified to analyze the unsteadiness with respect to the phase-locked EA. An example of these data is shown in Figure 3.50 for the PE operating point (the corresponding loading point on the 100% speedline for TC1 is also identified in Figure 3.50 for reference). In this figure, the dynamic EA pressure signals from the upstream and downstream sensors for each individual Stator trend together. In other words, the unsteady pressure pattern is the same for the upstream and downstream sensors, with only a DC offset (the Δp) separating the two sensors.

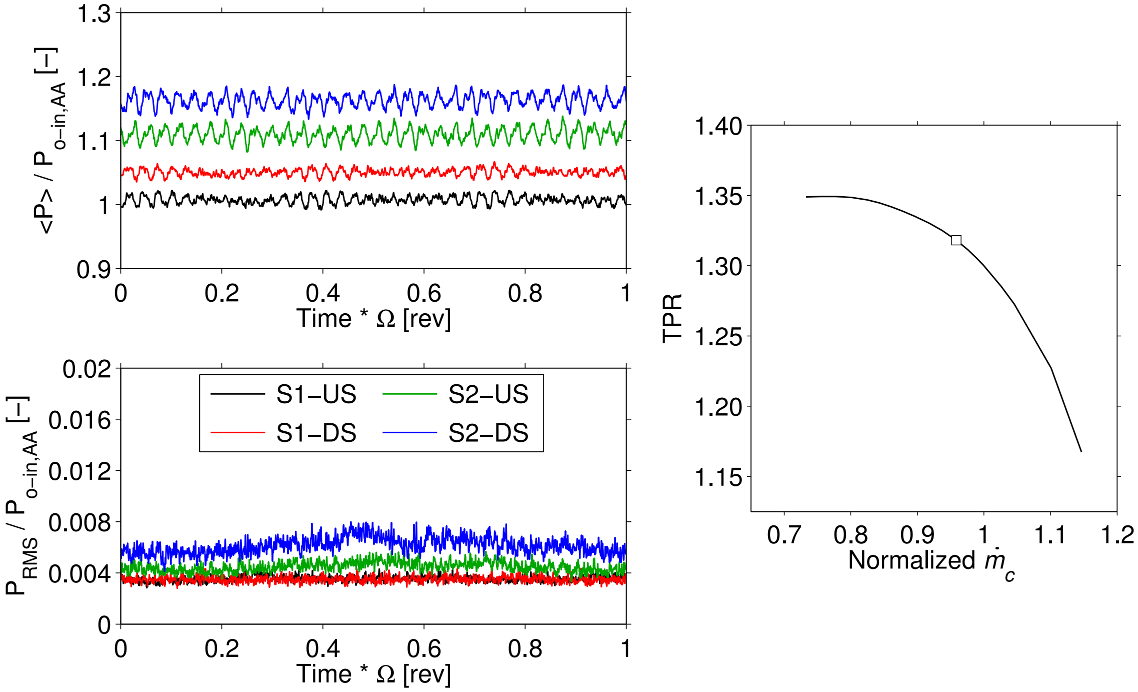

Figure 3.50: Phase-locked results (EA and RMS) for all four sensors at PE.

Figure 3.51 shows similar results at the HL operating condition. At this higher loading condition, the Stator 1 measurements show higher dynamic oscillations than at the PE condition, and the level of dynamic variation about the mean is similar for both Stator 1 and Stator 2 sensors. Considering the RMS unsteadiness in Figure 3.51, the Stator 2 sensors show a slight rise at each end of the revolution, signifying an increase of unsteadiness in a certain portion of the revolution. This same rise exists in the PE results above, Figure 3.50, and analysis of all conditions and speeds shows that it is a trend which occurs in the "central" portion of all speedlines (extending from approximately NL to HL). Analysis of the NS condition, Figure 3.52, confirms that the RMS unsteadiness is nearly constant across the entire revolution for all four sensors, although a higher overall level of unsteadiness is observed.

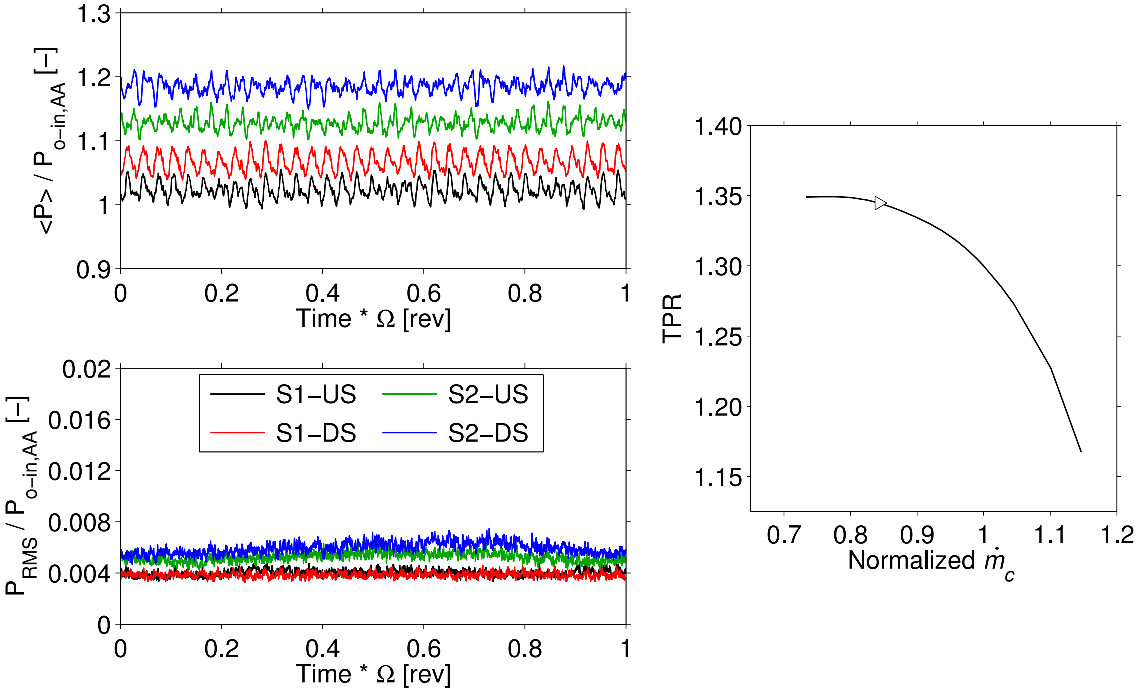

Figure 3.51: Phase-locked results (EA and RMS) for all four sensors at HL.

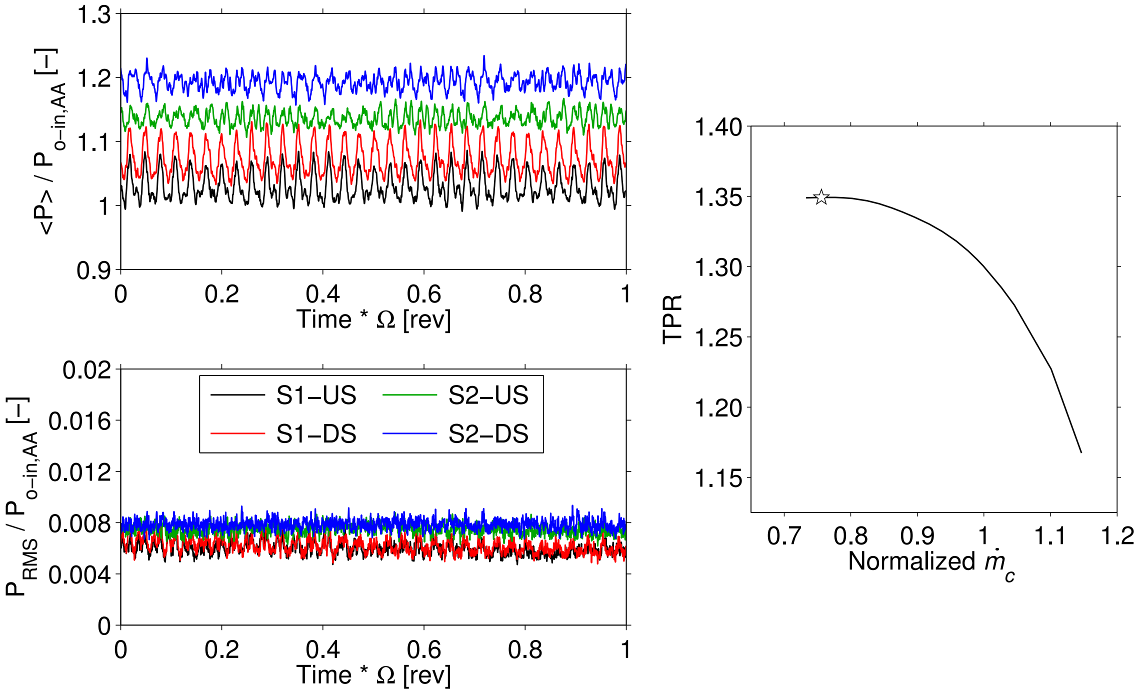

Figure 3.52: Phase-locked results (EA and RMS) for all four sensors at NS.

As discussed in the preceding section analyzing the time-average results, the two halves of the compressor portrayed slightly different levels of differential pressure (e.g., Figure 3.46). For each measurement condition, instantaneous differential pressure was calculated using the raw time series from each sensor pair (S1 and S2), and those data were subsequently analyzed for EA and RMS. Here, the EA and RMS differential pressures are compared from measurements collected on the two halves of the compressor in Figure 3.53 and Figure 3.54 for NL and HL, respectively. In these figures, the EA results are nominally offset on the ordinate due to the fact that the differential pressures are similar in magnitude. For both loading conditions, the EA and RMS data follow similar dynamic patterns, despite the DC offset observed between Half (a) and Half (b) results.

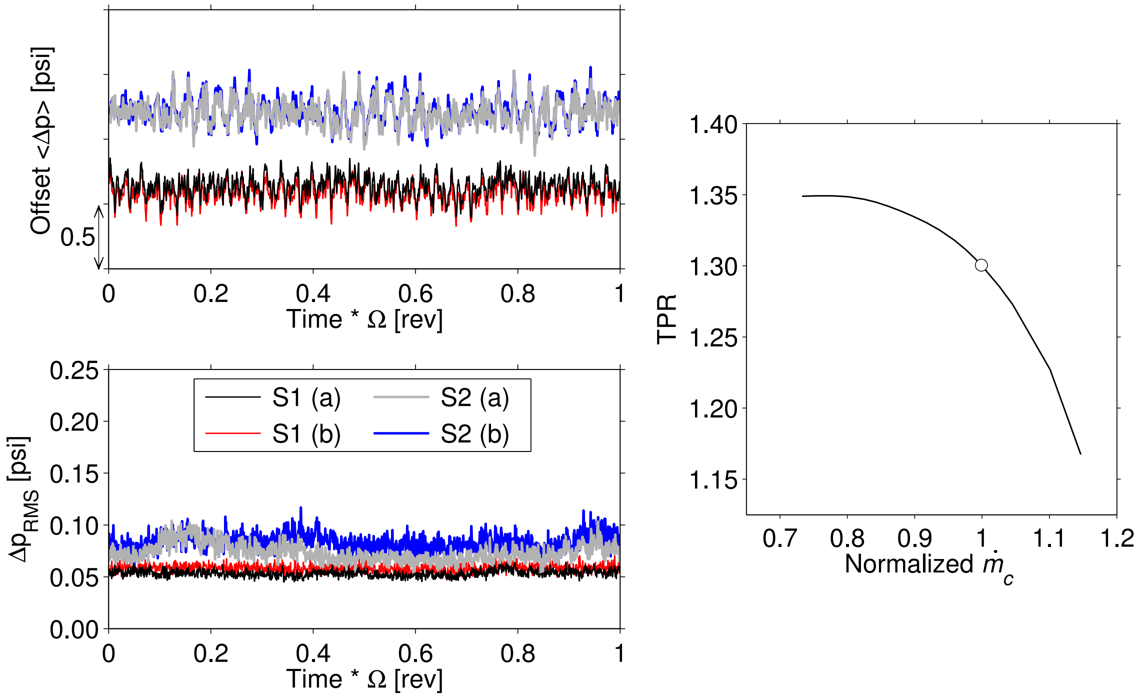

Figure 3.53: Comparison of phase-locked differential pressure measurements from two sides of the compressor at NL.

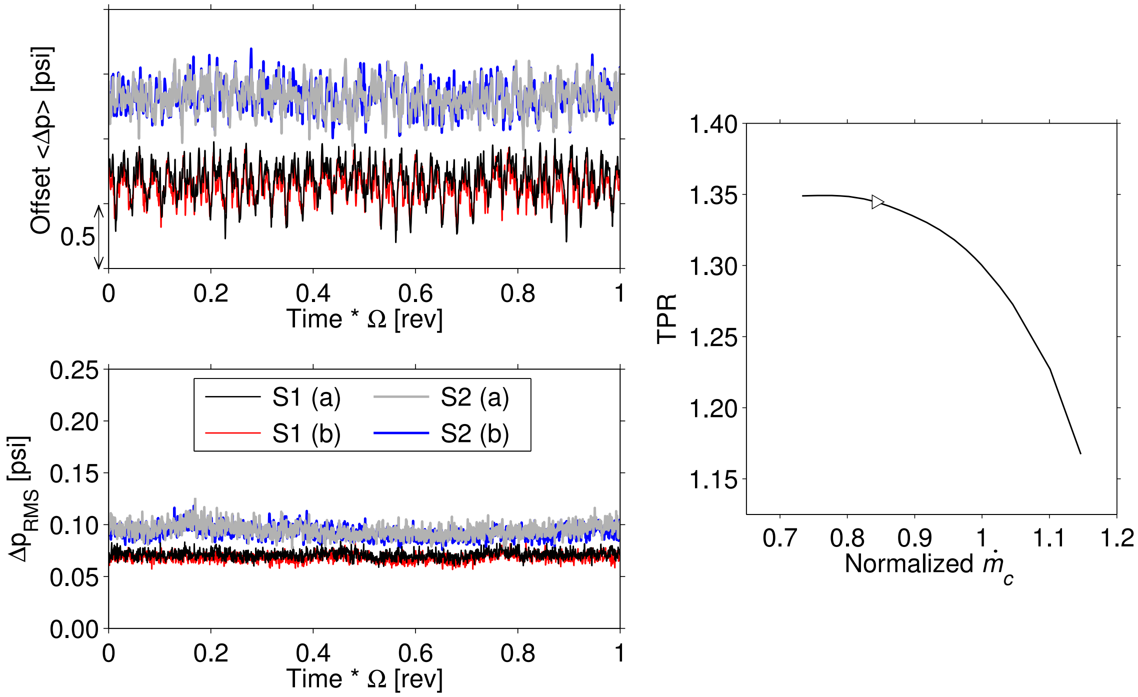

Figure 3.54: Comparison of phase-locked differential pressure measurements from two sides of the compressor at HL.

To this point, the EA pressure signals from the individual sensors and the differential pressures have shown that periodic conditions exist within the data, but the source of this content has yet to be identified. An example set of Fourier transform (FT) results from each of the four sensors, Figure 3.55, analyzes the frequency content of the signals at the HL operating condition.

In Figure 3.55, a 36/rev can be identified in each of the four sensors, and this content can be tracked to the blade count of Rotor 1. This result is somewhat expected due to the fact that all four sensors are downstream of Rotor 1 and will therefore sense its presence. Perhaps somewhat unexpected, however, is that the largest magnitude for all four sensors comes at the 33/rev frequency, which is associated with the blade count for Rotor 2. For Stator 1 sensors, this means that a considerable amount of energy is sensed as upstream-propagating from Rotor 2, but that a similar amount of energy is also felt as downstream-propagating toward Stator 2. These observations were not expected since the large amount of upstream-propagating energy from Rotor 3 is not similarly noted by the Stator 2 sensors, and a large amount of downstream-propagating energy from Rotor 1 is not similarly sensed by Stator 1. In all cases, additional frequency content is found scattered throughout 3/rev sums and differences due to interference patterns from adjacent rotor blade rows due to blade count differences of 3 blades from one row to the next (see Table 2.1).

Following these example FT results for the HL condition, a waterfall plot is shown to identify the frequency content across the entire 100% corrected speedline for these TC1 data. In Figure 3.56, the FT magnitudes for each sensors are shown, and the HL condition shown in Figure 3.55 is noted by a vertical dashed line on each plot.

In Figure 3.56, a few observations are noted. First, the 33/rev component is strongest for all four sensors across the entire range of flow rates on the abscissa. However, the magnitude of this component changes across the speedline, whereby it is strongest for Stator 1 measurements at high and low flow rates, but strongest for Stator 2 measurements in the middle range of flow rates. Second, an increase of broadband content exists for Stator 2 when compared with the Stator 1 sensors, and the greatest amount of broadband content is present at low flow rates approaching stall. Finally, there is an increase of high-frequency content for Stator 2 that is less apparent for Stator 1 sensors. These components, primarily existing above 70/rev, represent the third harmonics of the blade passing frequencies and corresponding combinations of 3/rev sums and differences.

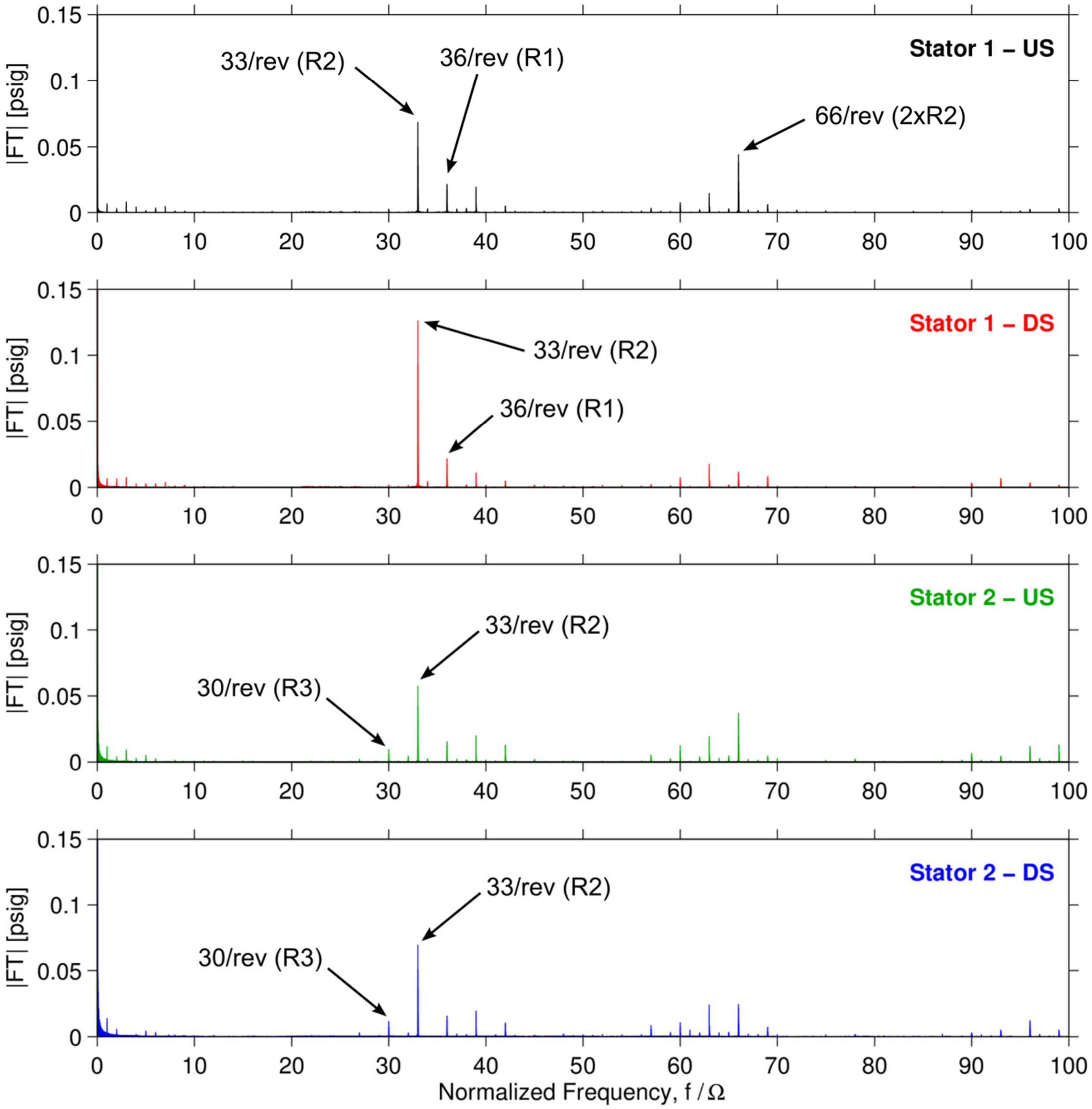

Figure 3.55: Example FT of seal cavity pressures at HL.

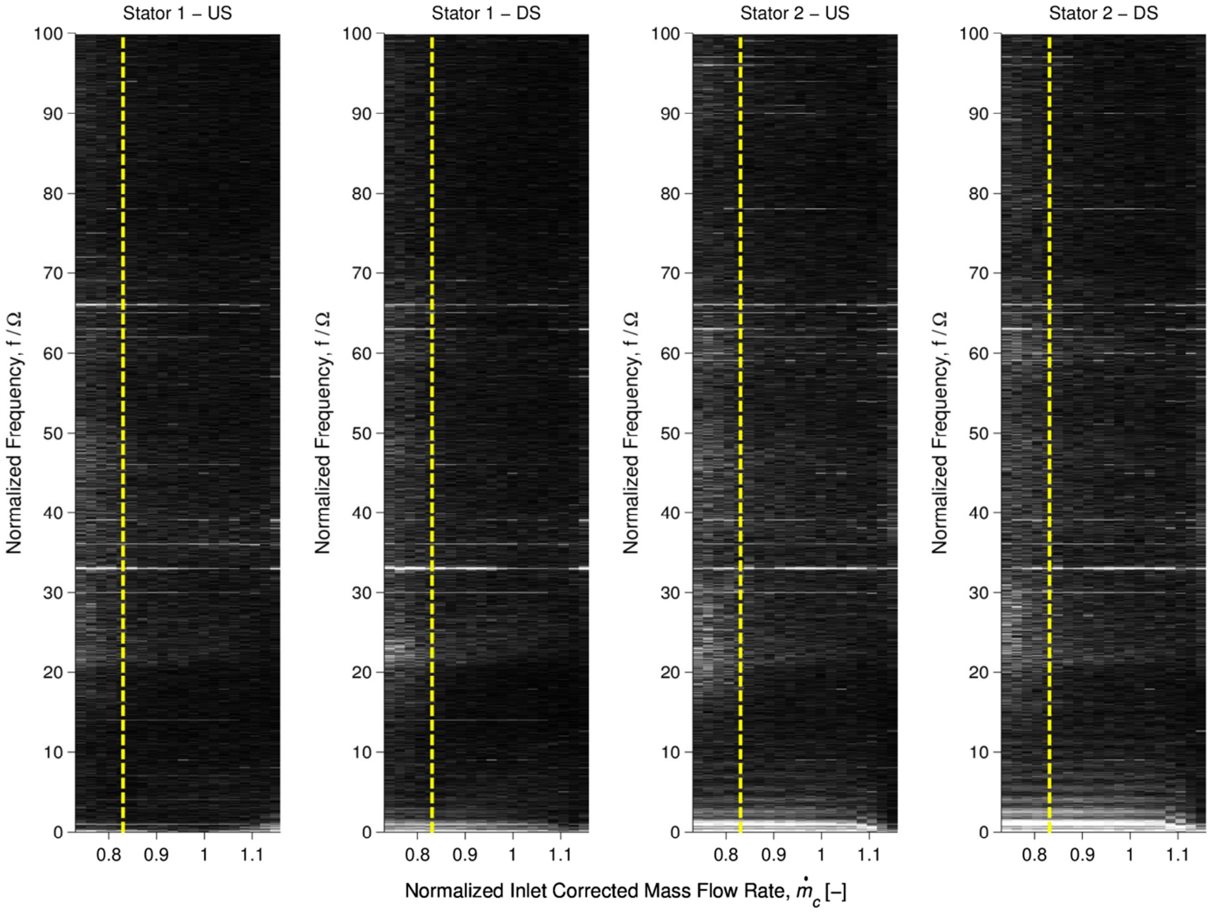

Figure 3.56: Waterfall plot of all four seal cavity pressure sensors as a function of corrected mass flow rate for 100% N_c. Dashed lines identify slices shown for HL in Figure 3.56

In addition to the waterfall plots for individual sensors in Figure 3.56, a similar waterfall plot is constructed for each stator, representing the FT magnitudes of the differential pressures, Figure 3.57. For these differential pressures, the same conclusion is drawn regarding the 33/rev component, for which Stator 1 shows greatest magnitudes at low and very high flow rates with a decrease in the middle region of the flow range, but Stator 2 shows the opposite trend with greatest 33/rev magnitudes in the middle of the flow range. Furthermore, the differential pressures in Figure 3.57 show a wide band of large magnitude components ranging from approximately 10/rev to 30/rev for both Stator 1 and Stator 2 at low flow rates approaching stall. The extent of this range is wider than for the individual sensors in Figure 3.56, which showed a wide band of high-magnitude components from approximately 20/rev to 30/rev.

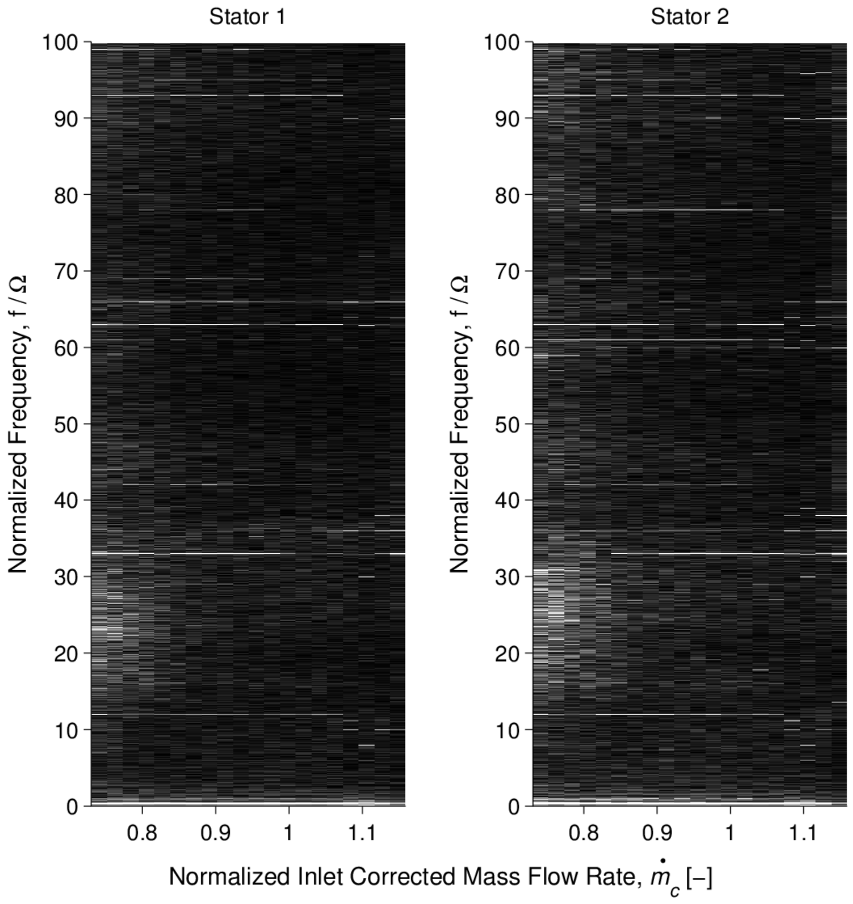

Figure 3.57: Waterfall plot of instantaneous differential pressure for Stator 1 and Stator 2 as a function of corrected mass flow rate for 100% N_c.

CHAPTER 4: SUMMARY AND CONCLUSIONS

The effect of rotor tip clearances on axial compressor performance has been a focus of research for several decades. In general, studies have found that pressure rise capability, efficiency, and operability range all decrease as the rotor tip clearance height is increased. However, the future of gas turbine engine engineering is moving toward designs which will incorporate smaller blade heights in the rear stages of high pressure compressors. As a result, a decrease in blade heights and a corresponding increase in relative rotor tip clearances are expected in the rear stages of these next-generation compressors. Therefore, a better understanding of the fundamental flow physics and multistage performance effects related to large tip clearance heights in axial compressors is a necessity.

4.1. Overview of Methods and Findings

This work has expanded upon previous investigations surrounding the effects of large rotor tip clearances on the performance of a three-stage axial compressor at Purdue University. A series of steady and time-resolved experimental measurement techniques has been implemented to evaluate compressor performance and interrogate the tip leakage flow for three rotor tip clearances: 1.5%, 3.0%, and 4.0% based on annulus height. Beyond this, additional efforts have been geared toward providing data to best define boundary conditions associated with the leakage flow paths in the compressor.

To supplement measurements already collected for the smallest (TC1) and largest (TC3) tip clearances, additional steady and time-resolved measurements of total pressure were collected for an intermediate clearance level (TC2) at two loading conditions on the 100% corrected speedline: a nominal loading point near the peak efficiency point and a low flow rate, high loading point. The steady total pressures provide a detailed look at the stator wake structures and the endwall flows. Furthermore, casting time-resolved rotor exit pressures in terms of an unsteadiness parameter (the RMS with respect to the ensemble average) made it possible to evaluate the radial and circumferential extent of the tip leakage flow structure. These measurements, in combination with existing three-component velocity data from hot-wire campaigns, helped to outline a new method for quantifying blockage in a multistage compressor using strictly pressure measurements (steady for stator exits and time-resolved for rotor exits). Additional evaluation of these results also showed how blockage develops through a multistage compressor at different loading conditions with different tip clearances.

Time resolved over-rotor static pressure measurements provided additional insight to the development and trajectory of the tip leakage flow. From these data, it was shown different conditions must be met for high loading conditions and low loading conditions to equivalent leakage flow trajectories when tip clearance is varied. Also, the impact of upstream and downstream vane rows was quantified in an understanding of multistage influences of tip leakage flow development. In addition to building upon the body of knowledge relating to tip leakage flow propagation, these measurements emphasize the importance of leakage flow trends which are often not accounted for in experimental measurements or computational assessments.

The measurements collected for this project represent a unique data set which contributes to an improved understanding of the tip leakage flow field and its associated loss mechanisms.

These data will serve the community as a method for validating computational design tools, especially at off-design conditions. Through this process, the results presented herein will aid in the development of new blade designs which could be desensitized to rotor tip leakage flows and their associated performance decrements.

4.2. Recommendations for Future Research

The results presented herein provide a wealth of data which will improve the understanding of tip leakage flow effects in axial compressors. However, there is still significant processing that can be performed to glean additional information from the collected data.

The detailed flow field traverses presented here were conducted only at the nominal loading and high loading operating conditions. Thus, there is a multitude of additional data which could be collected at additional loading conditions (i.e., a negative incidence, low loading condition). Also, further information will be gained in the future from conducting similar experiments with comparable instrumentation using more modern blade profiles and next-generation loss-mitigating blade design methodologies.

The understanding of the rotor tip leakage flow field and its impact on the compressor performance developed through this study has created a unique opportunity to investigate leakage flow control techniques (such as casing treatments) and other leakage flow desensitizing design methodologies in this three-stage axial compressor. Ultimately, it is these technologies that will help to drive the future of robust compressor designs.

Finally, the results presented here for shrouded stator cavity pressure measurements open a new opportunity to study seal leakage flows to a level of detail not previously attainable. These leakage flows have a profound effect on multistage compressor performance, and the initial pressure data available through this study provide a solid starting point from which to build models with accurate boundary conditions. However, a lot of interesting questions come to light from the unexpected spectral peak locations, the change of knife seal pressure difference with loading, and the trend of Δp near stall for Stator 2. Ideally, this further investigation would be led by a computational effort, and additional experimental data could be collected to verify CFD outcomes. In particular, the modular design of the instrumentation block facilitates a multitude of instrumentation configurations to meet CFD desires.

LIST OF ASSOCIATED PUBLICATIONS

[1] Berdanier, R.A., Smith, N.R., Fabian, J.C., and Key, N.L., 2015, “Humidity Effects on Experimental Compressor Performance—Corrected Conditions for Real Gases,” *J. Turbomach.*, **137**(3), 031011 (10 pages).
doi: 10.1115/1.4028356

[2] Berdanier, R.A. and Key, N.L., 2015, “Experimental Investigation of Factors Influencing Operating Rotor Tip Clearance in Multistage Compressors,” *Int. J. of Rot. Mach.*, Article ID 146272 (13 pages).
doi: 10.1155/2015/146272

[3] Smith, N.R., Berdanier, R.A., Fabian, J.C., and Key, N.L., 2015, “Reconciling Compressor Performance Differences with Varying Ambient Inlet Conditions,” *J. Eng. Gas Turbines and Power*, **137**(12), 122603 (9 pages).
doi: 10.1115/1.4030518

[4] Smith, N.R. and Key, N.L., 2015, “Flow visualization for investigating stator losses in a multistage axial compressor,” *Exp. in Fluids*, **56**(5), 94 (17 pages).
doi: 10.1007/s00348-015-1964-0

[5] Berdanier, R.A. and Key, N.L., 2015, “An Experimental Investigation of the Flow Physics Associated with End Wall Losses and Large Rotor Tip Clearances as Found in the Rear Stages of a High Pressure Compressor,” NASA/CR–2015-218868.
http://hdl.handle.net/2060/20150021045

[6] Berdanier, R.A. and Key, N.L., 2016, “The Effects of Tip Leakage Flow on the Performance of Multistage Compressors Used in Small Core Engine Applications,” *J. Eng. Gas Turbines and Power*, **138**(5), 052605 (10 pages).
doi: 10.1115/1.4031625

[7] Berdanier, R.A. and Key, N.L., 2016, “A Novel Data Reduction Technique for Single Slanted Hot-Wire Measurements Used to Study Incompressible Compressor Tip Leakage Flows,” *Exp. in Fluids*, **57**(3), 29 (14 pages).
doi: 10.1007/s00348-016-2114-z

[8] Berdanier, R.A. and Key, N.L., 2016, “Experimental Characterization of Tip Leakage Flow Trajectories in a Multistage Compressor,” *J. Propulsion and Power*, **32**(4), pp. 1022-1032.
doi: 10.2514/1.B35929

[9] Bhattacharya, S., Berdanier, R.A., Vlachos, P.P., and Key, N.L., 2016, "A New Particle Image Velocimetry Technique for Turbomachinery Applications," *J. Turbomach.*, **138**(12), 124501 (4 pages).
doi: 10.1115/1.4033672

[10] Berdanier, R.A. and Key, N.L., “Demonstrating Multistage Compressor Blockage Calculations Using Pressure Measurements for Large Tip Clearances,” under review for *J. Propulsion and Power*.

[11] Berdanier, R.A., Smith, N.R., Young, A.M., and Key, N.L., “Effects of Tip Clearance on Stall Inception in a Multistage Compressor,” under review for *J. Propulsion and Power*.

LIST OF REFERENCES

Adkins, Jr., G.G. and Smith, Jr., L.H., 1982, “Spanwise Mixing in Axial-Flow Turbomachines,” *Journal of Engineering for Power*, **104**(1), pp. 97-110.

American Society of Mechanical Engineers, 2004, “Flow Measurement,” ASME PTC 19.5-2004, pp. 19-27.

Ball, P.R., 2013, “An Experimental and Computational Investigation on the Effects of Stator Leakage Flow on Compressor Performance,” Purdue University, West Lafayette, IN, Master Thesis.

Berdanier, R.A. and Key, N.L., 2015a, "Experimental Investigation of Factors Influencing Operating Rotor Tip Clearance in Multistage Compressors," *International Journal of Rotating Machinery*, Article ID 146272 (14 pages).

Berdanier, R.A. and Key, N.L., 2015b, “An Experimental Investigation of the Flow Physics Associated with End Wall Losses and Large Rotor Tip Clearances as Found in the Rear Stages of a High Pressure Compressor,” NASA/CR–2015-218868.

Berdanier, R.A. and Key, N.L., 2016a, “The Effects of Tip Leakage Flow on the Performance of Multistage Compressors Used in Small Core Engine Applications,” *Journal of Engineering for Gas Turbines and Power*, **138**(5), 052605 (10 pages).

Berdanier, R.A. and Key, N.L., 2016b, “A Novel Data Reduction Technique for Single Slanted Hot-Wire Measurements Used to Study Incompressible Compressor Tip Leakage Flows,” *Experiments in Fluids*, **57**(3), 29 (14 pages).

Berdanier, R.A. and Key, N.L., 2016c, “Experimental Characterization of Tip Leakage Flow Trajectories in a Multistage Compressor,” *Journal of Propulsion and Power*, in press.

Berdanier, R.A., Smith, N.L., Fabian, J.C., and Key, N.L., 2015, “Humidity Effects on Experimental Compressor Performance—Corrected Conditions for Real Gases,” *Journal of Turbomachinery*, **137**(3), 031011 (10 pages).

Boyd, D.M., and Fleeter, S., 2003, “Axial Compressor Blade-to-Blade Unsteady Aerodynamic Variability,” *Journal of Propulsion and Power*, **19**(2), pp. 242-249.

Brossman, J.R., 2012, “An Investigation of Rotor Tip Leakage Flows in the Rear-Block of a Multistage Compressor,” Purdue University, West Lafayette, IN, PhD Thesis.

Chen, G.-T., 1991, “Vortical Structures in Turbomachinery Tip Clearance Flows,” Massachusetts Institute of Technology, Cambridge, MA, PhD Thesis.

Courtiade, N. and Ottavy, X., 2012, “Experimental Study of Surge Precursors in a High-Speed Multistage Compressor,” ASME Paper GT2012-68321, pp. 1-10.

Cumpsty, N.A., 1986, “Annulus Wall Boundary-Layer Measurements in a Four-Stage Compressor,” *Journal of Engineering for Gas Turbines and Power*, **108**(1), pp. 2-6.

Cumpsty, N.A., 2004, *Compressor Aerodynamics*, Krieger: Malabar, FL.

Denton, J.D., 2010, “Some Limitations of Turbomachinery CFD,” ASME Paper GT2010-22540, pp. 1-11.

Dickens, T. and Day, I., 2011, “The Design of Highly Loaded Axial Compressors,” Journal of Turbomachinery, **133**(3), pp. 1-10.

Erler, E., Vo, H.D., and Yu, H., 2016 “Desensitization of axial compressor performance and stability to tip clearance size,” *Journal of Turbomachinery*, **138**(3), 031006 (12 pages).

Erwin, J.R., 1964, “Experimental Techniques,” *Aerodynamics of Turbines and Compressors*, W.R. Hawthorne ed., Princeton University Press, Princeton, NJ, pp. 167-269.

Freeman, C., 1985, “Effect of Tip Clearance Flow on Compressor Stability and Engine Performance,” VKI Lecture Series, 1985-05.

Gallimore, S.J. and Cumpsty, N.A., 1986, “Spanwise Mixing in Multistage Axial Flow Compressors: Part I – Experimental Investigation,” *ASME Journal of Turbomachinery*, **108**(1), pp 2-9.

Goto, A., 1992, “Three-Dimensional Flow and Mixing in an Axial Flow Compressor with Different Rotor Tip Clearances,” *Journal of Turbomachinery*, **114**(3), pp. 675-685.

Gupta, A., Khalid, S.A., McNulty, G.S., and Dailey, L., 2003, “Prediction of Low Speed Compressor Rotor Flowfields with Large Tip Clearances,” ASME Paper GT2003-38637.

Heidegger, N.J., Hall, E.J., and Delaney, R.A., “Parameterized study of high-speed compressor seal cavity flow,” AIAA Paper No. 96-2807.

Heidmann, J.D., 2009, “NASA Turbomachinery Technical Working Group Technology Assessment,” *Mechanical Engineering: Global Gas Turbine News*, **49**(4), pp. 5-6.

Hunter, I.H. and Cumpsty, N.A., 1982, “Casing Wall Boundary-Layer Development Through an Isolated Compressor Rotor,” *Journal of Engineering for Power*, **104**(4), pp. 805-817.

Inoue, M., Kuroumaru, M., and Fukuhara, M., 1986, “Behavior of Tip Leakage Flow Behind an Axial Compressor Rotor,” *Journal of Engineering for Gas Turbines and Power*, **108**(1), pp. 7-14.

Key, N.L., Lawless, P.B., and Fleeter, S., 2010, “Rotor Wake Variability in a Multistage Compressor,” *Journal of Propulsion and Power*, **26**(2), pp. 344-352.

Khalid, S.A., Khalsa, A.S., Waitz, I.A., Tan, C.S., Greitzer, E.M., Cumpsty, N.A., Adamczyk, J.J., and Marble, F.E., 1999, “Endwall Blockage in Axial Compressors,” *Journal of Turbomachinery*, **121**(3), pp. 499-509.

Khalsa, A.S., 1996, “Endwall Blockage in Axial Compressors,” Massachusetts Institute of Technology, Cambridge, MA, PhD Thesis.

Krug, A., Busse, P., and Vogeler, K., 2015, “Experimental Investigation Into the Effects of the Steady Wake-Tip Clearance Vortex Interaction in a Compressor Cascade,” *Journal of Turbomachinery*, **137**(6), 061006 (10 pages).

Lakshminarayana, B., Pouagare, M., and Davino, R., 1982a, “Three-Dimensional Flow Field in the Tip Region of a Compressor Rotor Passage—Part 1: Mean Velocity Profiles and Annulus Wall Boundary Layer,” *Journal of Engineering for Power*, **104**(4), pp. 760-771.

Lakshminarayana, B., Davino, R., Pouagare, M., 1982b, “Three-Dimensional Flow Field in the Tip Region of a Compressor Rotor Passage—Part 1: Turbulence Properties,” *Journal of Engineering for Power*, **104**(4), pp. 772-781.

Lemmon, E. W., Huber, M. L., and McLinden, M. O., 2013, NIST Standard Reference Database 23: Reference Fluid Thermodynamic and Transport Properties—REFPROP, Version 9.1, National Institute of Standards and Technology, Standard Reference Data Program, Gaithersburg, MD.

LeJambre, C.R., Zacharias, R.M., Blederman, B.P., Gleixner, A.J., and Yetka, C.J., 1998, “Development and Application of a Multistage Navier-Stokes Flow Solver: Part II — Application to a High-Pressure Compressor Design,” *Journal of Turbomachinery*, **120**(4), pp. 215-223.

Levis, W.R., 2006, “Unsteady Casewall Pressure Measurements in a Transonic Compressor,” Naval Postgraduate School, Monterey, CA, Master Thesis.

Leylek, J.H. and Wisler, D.C., 1991, “Mixing in Axial-Flow Compressors: Conclusions Drawn from Three-Dimensional Navier-Stokes Analyses and Experiments,” *Journal of Turbomachinery*, **113**(2), pp 139-160.

Mahler, F.H., 1972, “Advanced Seal Technology,” Pratt and Whitney Aircraft Division Tech. Rep. PWA-4372, Feb., Also AFAPL-TR-72-8, Also NTIS Rep. AD739922.

Mailach, R., Lehmann, I, and Vogeler, K., 2008, “Periodical Unsteady Flow Within a Rotor Blade Row of an Axial Compressor—Part II: Wake-Tip Clearance Vortex Interaction,” *Journal of Turbomachinery*, **130**(4), 041005 (10 pages).

McDougall, N.M., 1990, “A Comparison Between the Design Point and Near-Stall Performance of an Axial Compressor,” *Journal of Turbomachinery*, **112**(1), pp. 109-115.

NACA Subcommittee on Compressors, 1950, “Standard Procedures for Rating and Testing Multistage Axial-Flow Compressors,” NACA TN-1138.

Peacock, R.E., 1982, “A review of turbomachinery tip gap effects. Part 1: Cascades,” *International Journal of Heat and Fluid Flow*, **3**(4), pp. 185-193.

Peacock, R.E., 1983, “A review of turbomachinery tip gap effects. Part 2: Rotating machinery,” *International Journal of Heat and Fluid Flow*, **4**(1), pp. 3-16.

Reeder, J.A., 1968, “Tip Clearance Problems in Axial Compressors (A Survey of Available Literature),” Atomic Energy Commission R&D Report K-1682.

Sans, J., Dell-Era, G., Desset, J., Brouckaert, J.-F., and Hiernaux, S., “Time-Resolved Measurements of the Unsteady Flow Field in a Single Stage Low Pressure Axial Compressor,” ASME Paper No. GT2013-94264, pp. 1-14.

Sherman, P.J., Dudley, R., and Suarez, M., 1996, “The Stochastic Structure of Downstream Pressure from an Axial Compressor – II. An Investigation of Blade-to-Blade Variability,” *Mechanical Systems and Signal Processing*, **10**(4), pp. 423-437

Shin, H.-W., Solomon, W., and Wadia, A., 2008, “Transonic fan tip-flow features revealed by high frequency response over-tip pressure measurements,” ASME Paper No. GT2008-50279, pp. 1-9.

Sirakov, B.T. and Tan, C.-S., 2003, “Effect of Unsteady Stator Wake—Rotor Double-Leakage Tip Clearance Flow Interaction on Time-Average Compressor Performance,” *Journal of Turbomachinery*, **125**(3), pp. 465-474.

Smith, L.H., 1970, “Casing Boundary Layers in Multistage Axial-Flow Compressors,” in: *Flow Research in Blading*, L.S. Dzung, ed., Elsevier, Amsterdam, p. 275.

Smith, N.R., 2015, “An Experimental Study on the Effects of Blade Row Interactions on Aerodynamic Loss Mechanisms in a Multistage Compressor,” Purdue University, West Lafayette, IN, PhD Thesis.

Smith, N.R. and Key, N.L., 2015, “Flow visualization for investigating stator losses in a multistage axial compressor,” *Experiments in Fluids*, **56**(5), 94 (17 pages).

Smith, N.R., Berdanier, R.A., Fabian, J.C., and Key, N.L., 2015, “Reconciling Compressor Performance Differences with Varying Ambient Inlet Conditions,” *Journal of Engineering for Gas Turbines and Power*, **137**(12), 122603 (9 pages).

Smith, N.R, Murray III, W.L., and Key, N.L., 2016, “Considerations for Measuring Compressor Aerodynamic Excitations Including Rotor Wakes and Tip Leakage Flows,” *Journal of Turbomachinery*, **138**(3), 031008 (9 pages).

Storer, J.A. and Cumpsty, N.A., 1994, “An Approximate Analysis and Prediction Method for Tip Clearance Loss in Axial Compressors,” *Journal of Turbomachinery*, **116**(4), pp. 648-656.

Suder, K.L., 1998, “Blockage Development in a Transonic, Axial Compressor Rotor,” *Journal of Turbomachinery*, **120**(3), pp 465-476.

Suder, K.L. and Celestina, M.L., 1996, “Experimental and Computational Investigation of the Tip Clearance Flow in a Transonic Axial Compressor Rotor,” *Journal of Turbomachinery*, **118**(2), pp 218-229.

Talalayev, A., 2011, “On the Renovation of the Three-Stage Axial Compressor Research Facility for Compressor Performance Research,” Purdue University, West Lafayette, IN, Master Thesis.

Tschirner, T., Johann, E., Müller, R., and Vogeler, K., 2006, “Effects of 3D aerofoil tip clearance variation on a 4-stage low speed compressor,” ASME Paper No. GT2006-90902, pp. 1-10.

Van Zante, D.E., Strazisar, A.J., Wood, J.R., Hathaway, M.D., and Okiishi, T.H., 1999, “Recommendations for Achieving Accurate Numerical Simulation of Tip Clearance Flows in Transonic Compressor Rotors,” *Journal of Turbomachinery*, **122**(4), pp 733-742.

Wagner, J.H., and Okiishi, T.H., “Analysis of Multistage, Axial Flow Turbomachine Wake Production, Transport, and Interaction,” Engineering Research Institute, Iowa State University, ISU-ERI-AMES-78173, TCRL-10 ERI Project 1204, Ames, IA, December 1977.

Wellborn, S.R., 1996, “Effects of shrouded stator cavity flows on multistage axial compressor aerodynamic performance,” Iowa State University, Ames, IA, PhD Thesis.

Wellborn, S.R. and Okiishi, T.H., 1999, “The Influence of Shrouded Stator Cavity Flows on Multistage Compressor Performance,” *Journal of Turbomachinery*, **121**(7), pp. 486-497.

Wellborn, S.R., Tolchinsky, I., and Okiishi, T.H., 2000, “Modeling Shrouded Stator Cavity Flows in Axial-Flow Compressors,” *Journal of Turbomachinery*, **122**(1), pp. 55-61.

Wernet, M.P., Van Zante, D., Strazisar, T.J., John, W.T., and Prahst, P.S., 2005, “Characterization of the tip clearance flow in an axial compressor using 3-D digital PIV,” *Experiments in Fluids*, **39**(4), pp. 743-753.

Williams, R., Gregory-Smith, D., and He, L., 2006, “A Study of Large Tip Clearance Flows in an Axial Compressor Blade Row,” ASME Paper No. GT2006-90463, pp. 1-9.

Wisler, D.C., 1985, “Loss Reduction in Axial-Flow Compressors Through Low-Speed Model Testing,” *Journal of Engineering for Gas Turbines and Power*, **107**(2), pp. 354-363.

Wisler, D.C., Bauer, R.C., and Okiishi, T.H., 1987, “Secondary Flow, Turbulent Diffusion, and Mixing in Axial Flow Compressors,” *Journal of Turbomachinery*, **109**(4), pp 455-482.

Wisler, D.C. and Beacher, B.F., 1989, “Improved Compressor Performance Using Recessed Clearance (Trenches),” *Journal of Propulsion*, **5**(4), pp. 469-475.

Yoon, S.Y., Song, S.J., and Shin, H.-W., 2006, “Influence of Flow Coefficient, Stagger Angle, and Tip Clearance on Tip Vortex in Axial Compressors,” *Journal of Fluids Engineering*, **128**(6), pp. 1274-1280.

Yoon, S., Selmeier, R., Cargill, P., and Wood, P., 2015, “Effect of the Stator Hub Configuration and Stage Design Parameters on Aerodynamic Loss in Axial Compressors,” *Journal of Turbomachinery*, **137**(9), 091001 (10 pages).